ANALYSIS OF SUBSEA BURIED PIPELINES AND PARTIALLY BURIED CABLES

A Dissertation

by

YANBIN BAI

Submitted to the Office of Graduate and Professional Studies of
Texas A&M University
in partial fulfillment of the requirements for the degree of

DOCTOR OF PHILOSOPHY

Chair of Committee,	John M. Niedzwecki
Committee Members,	H. Joseph Newton
	Marcelo Sanchez
	Jun Zhang
Head of Department,	Robin Autenrieth

December 2014

Major Subject: Ocean Engineering

ABSTRACT

This research investigation addresses the analysis and numerical simulation of two very important offshore engineering problems. The first deals with the modeling of the steady state thermal field around buried pipelines conveying high temperature wellhead mixtures of oil and gas, and their associated dissolved impurities. These pipelines may be buried using robotic trenching equipment for physical protection or to provide additional thermal insulation. The solution to this complex multi-layer problem is examined using a boundary element model approach. The second challenging problem is that of modeling a partially buried cable on the seafloor that is ensnared by commercial fishing equipment. There are many cables on the seafloor and several obvious systems are oceanic communication cables and the increasing number of subsea power transmission systems associated with the continuing development of offshore wind farms. In this problem an important numerical modeling challenge is to allow the cable to change its length as a result of the entanglement. A different approach is presented, i.e. a meshfree formulation, is specifically developed for simulating this type of subsea cable problem.

A two-dimensional boundary element model was developed specifically to investigate the local steady-state thermal field in the near field of the pipeline. Subsequently, a parametric study was preformed to evaluate the influence of the thermal power loss, burial depth, pipe diameter and soil thermal conductivity on the thermal field. The numerical examples illustrate the significant influence of the backfill thermal

property on the temperature at the pipe wall, that the pipe diameter controls the required output thermal power needed to maintain the desired pipe wall temperature, and the importance of pipeline burial depth on seabed temperature distribution above the pipeline.

In order to better address the problem of partially buried subsea cables, a three dimensional meshfree method was formulated and implemented to evaluate the structural response of cables in two dimensional space under accidental loads from trawling activities. The methodology specifically was developed to allow the arbitrary layout of a cable on the seafloor, the lengthening of an ensnared cable length at a boundary, and the inclusion of geometrical nonlinearity due to large deflection. This meshfree method is based upon a slender rod formulation, incorporates radial basis functions (RBF) for shape function construction, and utilizes a Galerkin weak formulation for the discretization of governing equations. The methodology was validated against two benchmark examples which have analytical solutions, and shows good convergence rates to the analytical solutions. Finally, a two dimensional gear-cable example illustrating the adaptive nature of this formulation and implementation to address a sliding length boundary condition is presented.

DEDICATION

To all of my families

And in memory of my dear grandfather, Mr. Bai, Jinxiang

ACKNOWLEDGEMENTS

It was a great pleasure to conduct research under the direction of Prof. John M. Niedzwecki in the Aggieland. I would like to express my sincere gratitude to him for his consistent support and insightful guidance. Three years ago, he picked me up when I stepped out of the dark days in my life and was seeking a new life in the Lone Star State. I would also like to thank Prof. Jun Zhang, Prof. H. Joseph Newton, and Prof. Marcelo Sanchez for their comments and suggestions during my research.

I'm grateful to the financial support for my study and research by China Scholarship Council and the Wofford Cain '13 Chair Endowment at Texas A&M University-College Station. I also wish to thank Prof. Charles Aubeny for the technical discussion on the geotechnical aspects of the numerical model inputs and Prof. Marcelo Sanchez for the help on the FEM software Code_Bright.

Dr. Maopeng Fang, Dr. Ziyong Su, Dr. Xiaochuan Yu, Dr. Yucheng Zhao, Mr. Liyun Zhu, MS. Han Huang, and Mr. Hooi Siang Kang are acknowledged for their valuable comments on my study and career development. Gratitude also goes to my colleagues and the department faculty and staff for making my time at Texas A&M University a joyful experience.

I would also like to express my special thanks to Mr. and Mrs. Sudlow for their caring and love when I was experiencing the hardest time in the US. Finally, I gratefully appreciate my parents and all family members for their love, trust, patience, and support.

NOMENCLATURE

BEM	Boundary Element Method
CB	Code_Bright
DEHS	Direct Electrical Heating System
EFG	Element Free Galerkin
HTHP	High Temperature High Pressure
Mfree	Meshfree Method
FDM	Finite Difference Method
FEM	Finite Element Method
FVM	Finite Volume Method
HRPIM	Hermite-type Radial Point Interpolation Method
LPIM	Local Point Interpolation Method
LRPIM	Local Radial Point Interpolation Method
MLPG	Meshless local Petrov-Galerkin
PIM	Point Interpolation Method
PIP	Pipe-in-Pipe
RBF	Radial Basis Function
RPIM	Radial Point Interpolation Method
RKPM	Reproducing Kernel Particle Method
ROV	Remotely Operated Vehicle
U-value	The Overall heat transfer coefficient

q	Heat Flux
κ	Thermal conductivity
T	Temperature
i	Liquid Flux
K	Hydraulic Permeability, *m/s*
k	Intrinsic Permeability, m^2
μ	Dynamic Viscosity of Fluid
ρ	Density
α	Thermal Expansion Coefficient of Fluid
β	Compressibility Coefficient of Fluid
P	Liquid Pressure in Porous Media
t	Time, s
c	Specific Heat
ϕ	Porosity
Subscripts	
sat	Saturated Clay
s	Dry Clay Solid Grain
w	Saline Seawater
0	Reference Value

TABLE OF CONTENTS

Page

LIST OF FIGURES

Page

LIST OF TABLES

Page

1. INTRODUCTION*

The increasing need for hydrocarbons as the primary source of energy is driving the exploration and eventual production of oil and gas discoveries in the Arctic and in worldwide ultra-deep water sites. New engineering challenges have emerged for subsea pipeline systems designed to operate in these areas that include ice interaction with the seabed, freeze-thaw cycles, and high pressures as well as high temperature flows from the well-head. The first arctic production pipeline was installed in the North American Arctic in 2000 and a few flow lines were deployed in 2005-2006 in the Gulf of Mexico in water depths of approximately 2750m. Production safety, environmental risk management, structural integrity and flow assurance are of vital importance for the recovery of hydrocarbons at these often remote sites.

Considering frozen soil at Arctic sites, temperature rise of soil due to buried pipelines may cause significant thaw settlement which may result in structural failure of pipelines (Braden et al., 1998). Regarding structural stability, upheaval thermal buckling is another threat to buried pipelines, which is somehow different from the lateral thermal buckling of bare pipelines. The low ambient temperature observed in very deepwater and at Arctic sites has led to innovative pipeline designs to assure the transport oil produced in these regions. Hydrate formation and wax deposition are two major threats

* Part of the data reported in Section 1.1 of this chapter is reprinted with permission from "Modeling of deepwater seabed steady-state thermal fields around buried pipeline including trenching and backfill effects" by Yanbin Bai and John M. Niedzwecki, 2014. *Computers and Geotechnics*, Volume 61, 221-229, Copyright (2014) by Elsevier B.V.

that may result in blockage or possible plugging of pipelines transporting hot fluids from wellhead to collection points (Lenes et al., 2005). As a consequence of the heat dissipation rates from pipelines transporting very hot multi-phase wellhead fluids to the surrounding environment, thermal insulation may be complimented with integrated heating systems in order to mitigate possible flow assurance issues. Passive thermal insulation, pipe-in-pipe (PIP) heating, direct electrical heating systems (DEHS) or some combinations are designed for hydrate formation prevention. Heggdal et al. (2012) investigated the use of the electrical heating for large diameter subsea pipelines intended for the deepwater application. The major concerns when using the heating technology include the potential of aggravating the thermal buckling issue due to over-heating and the unintended consequences of the heat dissipated from subsea artificial heat source mainly pipelines and power cables that may adversely affect the local marine environment and ecosystem (Kogan et al., 2003). In addition, subsea burial can play an important role in providing physical protection from accidental loads such as iceberg scouring of the seabed in arctic regions (DeGeer and Nessim, 2008), reducing uplift risk due to axial thermal expansion (Gharbawy, 2006), and improving thermal insulation by avoiding strong natural convection effect in seawater (Young et al., 2001). Even though hydrate inhibitors are utilized to reduce hydrate formation, temperature management still plays a dominating role in hydrate formation prevention, wax deposition and plugging. Thus, thermal field investigation about buried subsea pipelines plays a key role in the pipeline system design, and may mitigate the possible thermal impact on the local marine ecosystem.

Besides the thermal problem about subsea pipelines, the interaction between modern bottom-trawling fishing gears as shown in Fig. 1.1 and submarine facilities such as subsea cables as shown in Fig. 1.2 is attracting more and more attention in the past decades, especially in Europe due to the mature development of the extensive subsea pipeline network and the fast growth of subsea power grid for offshore wind farms. Submarine flexible structures such as pipelines, power and telecom cables spanning oceans have been successfully used worldwide in the past a few decades. The study of the interaction between trawl gears and submarine pipelines follows closely the trend of the extensive development of pipeline network, especially in the Gulf of Mexico and in the North Sea.

Fig. 1.1 An example of bottom trawling fishing (Gelach, 2012)

Fig. 1.2 An example of a submarine power cable inspection (Heimbuch, 2010)

The rapid growth of offshore wind energy production in Europe and the resulting and prospective extension of subsea power grid network as illustrated in Fig. 1.3 also presents interesting challenges, especially near shore and in the shallow water where trawl gears increasingly impact pipelines and various cable systems. Drew (2009) reported that annually fishing and anchoring activities result in about 100-150 cable breakages. Considering the increasing investment on offshore wind farms and on-going development of modern fishing gears, the interaction of trawl gears and cables is of interest. This research study will examine the mechanics and behavior of cables under accidental loads, load dependent moving boundary conditions, and structural evaluation under specific scenarios.

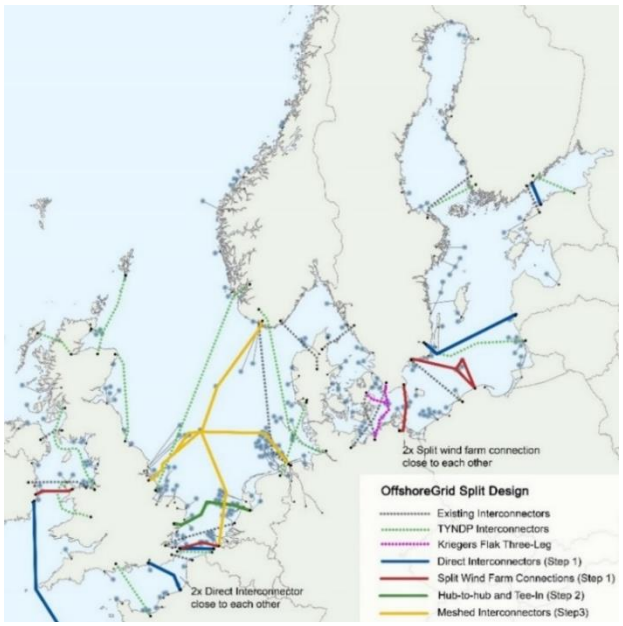

Fig. 1.3 Offshore power grid in Europe (European Wind Energy Association, 2010)

1.1 Heat Transfer of Subsea Buried Pipelines

The two primary offshore classification societies, ABS and DNV, don't provide detailed guidance on the thermal design of fully buried pipelines. As for the preliminary thermal design, Bai et al. (2005) summarized the overall heat transfer coefficient (U-value) method. Burial depth and thermal conductivity of surrounding soil are included in the U-value method assuming the soil as a single homogeneous solid medium. However, the natural convection, trenching and backfill effects, and layered property of marine soils, which may pose significant impacts on the thermal field, are ignored in the U-value method. Earlier research studies by Thiyagarijan et al. (1974), Martin et al. (1978) and Bau (1982) developed an analytical approach to study the thermal behavior of a buried pipe and the surrounding soil. For cases where one wishes to investigate the

spatially dependent thermal properties or piecewise homogeneous domains of problem domain, numerical simulations and/or experimental measurements must be pursued in order to more accurately characterize the resulting thermal distributions. Representative studies investigating buried pipelines and power cables using a variety of numerical methods are summarized in Tab. 1.1. The thermal field in soil near power cables placed in a duct was investigated by Mitchell and Abdel-Hadi (1979), Gela and Dai (1988) and Hanna et al. (1993), and collectively these studies provide a guide for the design of sheathing for power cables. In those studies the soil was modeled as a solid medium, and the critical parameters affecting the heat dissipation in the soil included the thermal property of backfill material, the burial depth, and layout of the cables. Neglecting trenching and backfill aspects, Lu et al. (2008) used their model to investigate the phase change phenomenon of fully saturated soils around a buried pipe in winter conditions. They evaluated the heat conduction effects of crude oil in the pipeline and the natural convection of fluid flow induced in the soil during a shutdown period. Assuming soil to be a homogeneous solid media, Barletta et al. (2008) studied the temperature fluctuation in a subsea pipeline under the start-up and shutdown conditions using a finite element model. Later, Xu et al. (2010) used a finite volume method to investigate the shutdown time neglecting both the natural convection in soil and the backfill conditions. In an experimental study, Newson et al. (2002) investigated the influence of moisture and void ratio changes on the thermal conductivity of marine clay in the North Sea. They found that the moisture content of disturbed clay could be up to 95% and that the corresponding thermal conductivity decreased to 0.8 $W/m\,K$ compared to that of the

undisturbed soil, which approaches that of still seawater 0.65 *W/m K*. In contrast, the thermal conductivity of the undisturbed clay is typically around 1.0 *W/m K*. Based upon numerical simulations using a finite element program Code_Bright (UPC, 2013), it was found for the extremely low hydraulic permeability 10^{-8}~10^{-7} *m/s* associated with deepwater clay that the natural convection resulted from the heat exchange with the pipeline controls the time required to reach the steady state but only slightly impacts the final steady state temperature distribution. Thus, the natural convection effect is not considered in the steady state investigation around a pipeline buried in such clay.

The modeling of subsea pipelines buried in layered soil where the effects of trenching and backfill are included, involves with a problem domain that has complicated interfaces. Though it is true that transient analysis is essential for both start-up and the cooling down of pipeline regarding the detailed thermal design of subsea pipeline, this study is focused on the steady state thermal field, which is sensitive to variations of key parameters associated with trenching and backfill topography in a layered seabed. It is common that the transient start-up and cool-down analyses of a pipeline is used to investigate the time to reach steady state and to understand the natural convection in porous soil using a more simplified FEM model. However, the boundary element method has been shown to be a very efficient approach that model multi-piecewise media and multiple domains to solve two-dimensional steady state heat transfer (Atalay et al., 2004) and three-dimensional static elastic problems (Gao, 2007). Consequently, BEM has been adopted to mathematically model heat transfer of such a pipe-trenching problem.

Table 1.1 Methodologies compassion on selected papers

Year	Author	Time dependence	Numerical scheme	Property of soil	Dim.	Operational mode	Comment
1979	Mitchell	transient and steady	FEM	homogeneous mother soil	2D	Operational mode of power cables	Convection of air was included. Geometry of trench, thermal property of soil, cable size, and solar radiation were included. Geometry of cable was not kept. Natural convection in soil was not considered. Time consuming on modeling and computation.
1988	Gela	steady state	BEM	homogeneous mother soil	2D	Operational mode of power cables	Convection of air was neglected. Trenching and backfill were considered. Natural convection in soil was not included. Both single cable and multi-cable system were studied. It is efficient on modeling and computation.
1993	Hanna	transient	FDM	homogeneous mother soil	2D	Operational mode of power cables	Convection of air was handled. Trenching and backfill effect were included. Geometry of cable was not kept. It didn't include natural convection.
2008	Lu	transient	FDM	homogeneous and porous	2D	Shut down of oil pipelines	Convection of air was included. Natural convection in soil and conduction between cooling oil and pipe wall were treated. Trenching and backfill were not handled.
2008	Barletta	transient	FEM	homogeneous	2D	Start-up of oil pipelines	Natural convection was not considered. Conduction and convection on seabed were not included. Trenching and backfill were not considered.
2010	Xu	transient	FVM	homogeneous	2D	Shut down of oil pipelines	Equivalent conductivity was adopted to simplify convection between oil and pipe wall. Convection of air was handled. Natural convection in soil and trenching effect were not included.

1.2 Interference of Trawling and Subsea Structures

The mechanism of the interaction between subsea cables and trawl gears is similar to that occurring with subsea pipelines located on the seabed that have increased bending stiffness and other design specifications. DNV (2010) provides some design guidance of pipelines in the later instance considering the collision process and analysis procedures of trawl gear engaging a subsea pipeline. The collision can be logically divided into three parts: the initial impact stage, the pull-over phase, and/or a final hooking event. The hooking cases between a pipeline, a power cable, and the trawl board are illustrated in Fig. 1.4 and Fig.1.5.

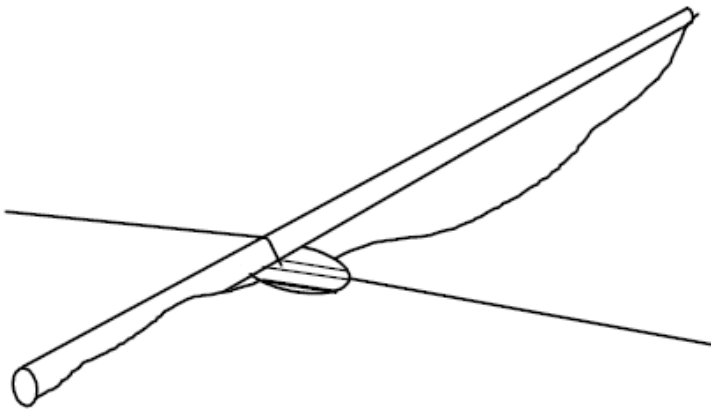

Fig. 1.4 Hooking scenario of a pipeline and trawl board (DNV, 2010)

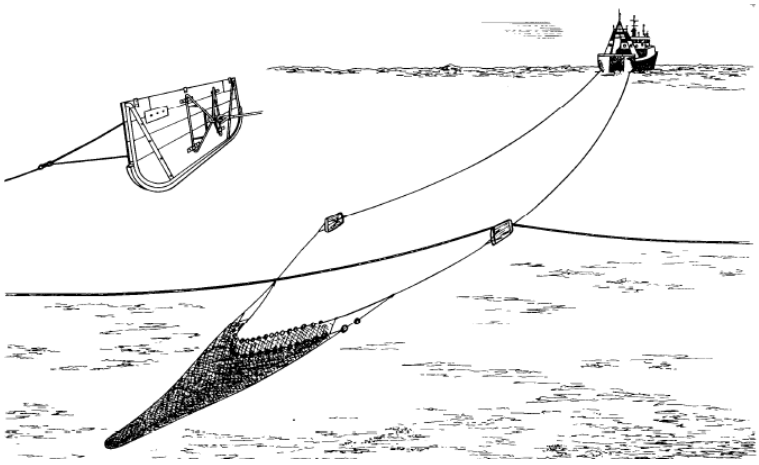

Fig. 1.5 Hooking scenario of a power cable and trawl board (Drew, 2010)

Most of the research studies reported on this topic were conducted in Europe recently, see for example Longva (2011), Vervik (2011), and Johnsen (2012). While in this study, the focus is about the interaction of trawl gears with cables other than with pipelines. Due to the differences of the flexibility and weight per unit length when compared to pipelines, the cable response will be dramatically different. Since a cable is tension dominated and behaves like a flexible beam during the pulling process, assuming the towing speed of the fishing vessel is low, the damage to the subsea cable may not be too significant during the initial impact stage. In the pull-hooking case, due to the massive weight of a typical trawling board up to 9 tonnes with an additional clump weight of 9-10 tonnes, the maximum pulling force may exceed the break load of the submarine cables. Fig. 1.6 shows a model of an industry trawling board for experimental test. If the pulling force reaches the break load of a cable in the pull-hooking case, the pull of a trawl board and a clump weight on the cable is considered as a hooking case. Seizing of cables into the gap between the warp line and trawling board

or clump weight is regarded as a direct hooking scenario. Hooking is a rare situation for a pipeline as shown in Fig. 1.4, but may be a more common scenario for cables considering the relative dimension ratio of a typical cable to that of the trawling gear used in modern industry fishing. Furthermore, the moving of partially buried cables along with gears introduces a drag force due to the friction of seabed soil. Besides, the displacement boundaries also depend on the drag force since the cables move with the towing fishing gear or fishing net. The friction force and moving boundary conditions make the response of cable under the pull of trawling gears more complicated and thus more challenging.

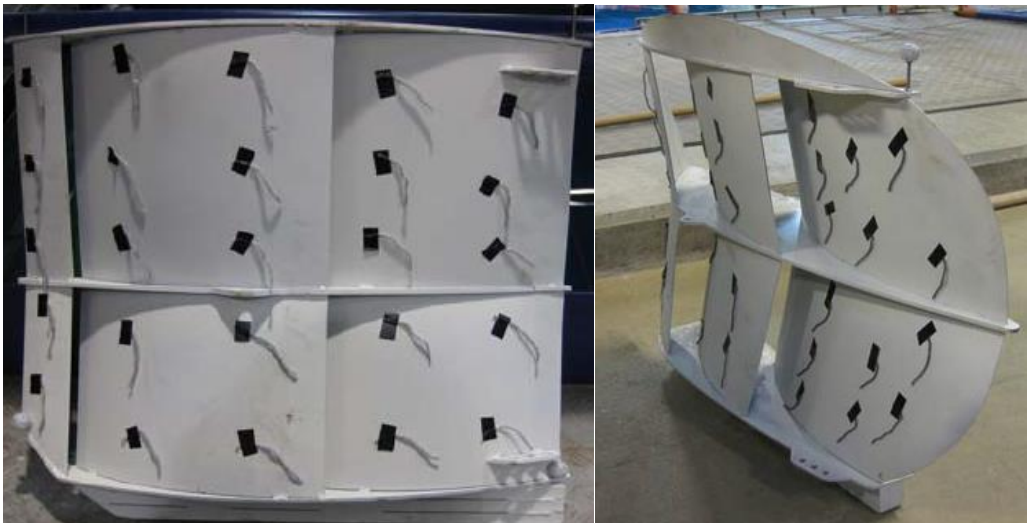

Fig. 1.6 Front and side view of a scaled trawling board model (Teigen et al., 2009)

The interference between trawling gears and submarine slender structures went back to the experimental study of fishing gear impact loads on pipelines in the 1970s.

Hermann et al. (1980) reported the maximum pull-over force around 200 KN and pull-over duration around 1 second, which depends on the shape and weight of trawling gear and the diameter of a pipeline. Attributed to the development of FEM on solving strong nonlinear problems using updated Lagrange approach, Longva et al. (2011) adopted SIMLA developed by MARINTEK and performed the dynamics response of pipeline including the impact and pull-over phase under the drag of trawl boards, which focuses on global response behavior of the pipeline. The added mass and drag coefficient in the simulation are available by the model test conducted by Statoil (Teigen et al., 2009).

Though both the power cable and pipeline are slender structures and subject to the similar accidental impact loads, both the global response behavior and local damage mechanism are somewhat different due to the discrepancy in diameter, structural configuration, and flexural rigidity. Regarding the global displacement response, the power cable may experience large deflection, which is a strong geometrically nonlinear problem. The slender rod model such as Bernoulli-Euler model and Kirchhoff-Love model considering finite-strain is well suited for solving the static and dynamic problem of submarine slender structures. Nordgren (1974) and Garrett (1982) have formulated the equation of motion of slender rods by vector analysis in a curvilinear coordinate and solved this problem by FDM and FEM respectively. Subsequently, Ma and Webster (1994) extended this formulation to risers with internal pressure under complex hydrodynamic loading for offshore applications in 2-D space. Later, Chen and Zhang (2001) introduced a new constraint condition allowing large elongation to tension dominant slender rod and further implemented the 3-D formulation in Cable3D (Chen,

2002).

In recent years, innovative meshfree methods have been proposed to solve 4^{th} order partial differential equations, such as beam and shell bending problems. A meshfree method doesn't need a confined mesh grid over the problem domain and has comparative advantages on domain representation and on strong nonlinearities over FEM. Pioneers including Belytschko et al. (1994), Liu et al. (1993), Atluri and Zhu (1998), Liu and Gu (1999) etc. have paved the road for the meshfree method and have proposed the element free Galerkin (EFG) method, reproducing kernel particle method (RKPM), the meshless local Petrov-Galerkin method (MLPG), the point interpolation method (PIM), and the radial point interpolation method (RPIM), respectively. The differences between these methods include weak formulations and field interpolation techniques. Moreover, the meshfree methods have been applied to both the thin and thick beams by a few scholars. Chen et al. (1996) adopted the RKPM approach for the construction of shape functions for the field interpolation and constitutive law, and then solved the large deformation of a thick beam considering both geometry and material nonlinearities. Donning et al. (1998) applied Galerkin weak formulation and RKPM interpolation scheme to a curved beam and a Mindlin plate. Consequently, the MLPG was validated by a comparison to the analytical solution of Bernoulli-Euler beam theory (Atluri et al., 1999). Using the local weak formulation, the PIM was applied to a straight thin beam by Gu and Liu (2001), which adopts the idea of MLPG for the discretization of strong-form governing equation. Recently, Cui et al. (2008) applied the gradient smoothing technique proposed by Liu (2008) to a thin beam treating the rotation angle

and displacement as independent variables in the field value interpolation, where the weak formulation is developed by one gradient smoothing technique. As a generalized numerical technique, the meshfree method adopts field nodes to represent the problem domain other than mesh grid in FEM. It overcomes the difficulty of instantaneous remeshing of deformed structures experiencing large deflections and avoids the element distortion problem in FEM. Thus, it is suited to solve the large rigid body rotation and deflection of a slender rod, which will be applied to the interference of bottom trawling and cables.

1.3 Research Objectives

A major objective of this research is to further formulate the Boundary Element Method and a Meshfree Method to subsea structures and to develop efficient computer tools for some subsea engineering applications. These techniques will be used to gain a better understanding of assumptions regarding the thermal field around subsea buried pipelines and subsea cable systems often simply placed on the seafloor. In the latter case, the issues investigated will revolve around the interaction of bottom trawl gears with cables and the resulting response leading to possible failure of cables. The research study including two kinds of offshore applications is logically divided into two parts.

The first part of this study focuses on the formulation of Boundary Element Method (BEM) to the steady state heat transfer of a subsea pipeline-multilayer soil system. The thermal field is modeled as a two-dimensional vertical slice along a pipeline. The heat transfer for layered media is first formulated and then implemented in

Matlab. Later, corresponding formulations are accomplished for the modeling of a pipe-trench problem so that key parametric variations and their impacts on the thermal fields can be investigated. The BEM was selected, since remotely operated vehicles (ROVs) especially designed to bury pipelines are widely used and the subsequent installation results in a multiple layered soil domains with complex interfaces. The numerical model addresses trenching and backfill effects, layered property of subsea soils, and the cooling conductive effect of seawater, while neglecting the natural convection effect in the deep-water clay with extremely low hydraulic permeability. This aspect of the proposed research study targets the preliminary thermal design of buried pipelines intended for deepwater and arctic applications and a possible thermal impact on the subsea marine ecology.

In the second part of this research study, a meshfree method will be further formulated to slender cables that is based in part upon the slender rod formulation originally developed by Nordgren (1974) and Garrett (1982). Herein the focus will be on the exploration of the potential of the meshfree method to slender rod structures and the structural response analysis of subsea cables laid on the surface of the seabed or partially buried in the seafloor. Their initial configurations on the seabed need not be a straight path and can be somewhat arbitrary. As the load imposed on a cable by trawl gears can be load-dependent moving boundaries consistent with that of partially buried subsea cables. The meshfree method formulation is to be implemented in Matlab and will be used to investigate the behavior of subsea cables subject to accidental loads from bottom trawling fishing activities.

2. FORMULATION OF HEAT TRANSFER IN LAYERED MEDIA

2.1 Literature Review of BEM on Heat Transfer

Jointing with domain methods such as Finite Difference Method (FDM), Finite Element Method (FEM), Finite Volume Method (FVM), and Meshfree Methods, Boundary Element Method (BEM) has been evolving as an efficient and complementary numerical method for a bunch of partial differential equations. Numerous scientists and researchers have enriched the mathematical foundation of the boundary integral method which was historically depicted by Cheng and Cheng (2005). The term BEM was first adopted by Brebbia and Dominguez (1977) and then widely accepted in the academia. Taking advantage of weighted residual technique and weak formulation, Brebbia and Dominguez (1977) developed a direct formulation of boundary integral equation for potential problem governed by Laplace's equation. Attributed to the enormous efforts exerted on the implementation of BEM, a number of BEM variants has been emerged in the past three decades and successfully applied to a broad topics such as acoustics, solid mechanics, hydrodynamics, structural vibration and heat transfer (Yu et al., 2010). Apart from the extensive applications of these BEM variants, an innovative computational acceleration scheme, Fast Multipole BEM (FMM), has been proposed by Rokhlin and Greengard (1985, 1987). FMM reduces the computation by one order of operation in order to solve large scale problems.

Regarding thermal field problems, BEM is well suited to solve steady and transient heat transfer in solid media as well as in porous media restricted to a steady

state scenario. In an earlier study, Wrobel and Brebbia (1979) applied the direct BEM formulation to heat conduction in homogeneous solid media and incorporated a time-dependent fundamental solution for the linear transient heat conduction problem. Later, the nonlinear heat conduction, resulted from temperature-dependent material has been solved by Kikuta et al. (1987) using a Kirchhoff transformation scheme, and by Wrobel and Brebbia (1988) using dual reciprocity BEM (DRM). Subsequently, multiple reciprocity BEM (MRM) (Nowak and Brebbia, 1989) and triple-reciprocity BEM (Ochiai et al., 2006) have been proposed in order to eliminate the background cell for some field integration terms. All of these studies rely on a time-dependent fundamental solution so as to eliminate some field integrals. Meanwhile, other BEM variants have also been further developed to solve transient problem such as Galerkin BEM (Sutradhar et al., 2002) and Laplace transform DRM (Zhu and Satravaha, 1996).

For cases involved with spatial-dependent material and multiple domains, efforts have also been made in both analytical approaches and numerical schemes. Simões and Tadeu (2005) derived the Green's functions for a multi-layer medium in the frequency domain and retrieved the time domain temperature distribution by the inverse Fourier transformation. Following the procedure of the collocation BEM, Gao (2006) solved the steady state heat conduction in a spatial-dependent material, which adopted a radial integration method (Gao, 2002) so as to convert the existing domain integral into boundary integrals. Additionally, Gao (2006) proposed an interface integral BEM (IIBEM) for multi-domain problems by assuming a thin layer between two adjacent domains. Based upon the direct BEM, the most direct numerical scheme for multiple

domains was named as multiple domain BEM and described by Atalay et al. (2004) and Gao et al. (2007).

BEM facilitates the numerical implementation and the computational modeling from two aspects. On one hand, through transforming the strong-form governing equation to a weak-form boundary integral representation and by approximating boundary value using the boundary element technique, BEM greatly reduced the number of algebraic equations needed to solve unknowns on boundaries. This makes it a computationally efficient numerical method. On the other hand, the reduction in discretization dimension also facilitates the mesh of the problem domain especially for those problems comprising multiple regions and complex geometries.

In this study, boundary element method for homogenous medium has been further developed to solve the steady state heat conduction in layered medium with/without internal heat source. One computer program called Layered Medium Boundary Element Method (LBEM) is constructed based on the proposed methodology and procedure. It is capable of handling heat conduction in layered media with all plausible boundary conditions and applicable to any real cable/pipeline configuration in layered soil. LBEM adopting a quadratic element, which is better at dealing with curved boundaries, was verified by benchmark scenarios compared with IIBEM and FEM. Finally, LBEM was applied to steady state heat conduction in layered soil after the setup of a heat pipeline with the inclusion of trenching and backfill effects in deepwater in Chapter 3.

2.2 BEM Formulation of Heat Transfer in Layered Media

First, a boundary integral equation for a homogeneous isotropic medium is applied to each layer. Then by assuring the continuity of temperature and normal heat flux on the interface of two adjacent layers, global systematic algebraic equations are to be assembled from formulations of all layers. The complete and detailed steps in the formulation are elaborated here for completeness.

The Laplace equation governs the steady-state heat transfer problem in each isotropic homogeneous subdomains depicted in Fig. 2.1. Brebbia et al. (1992) utilized Green's theorem and a weighted residual technique to develop the integral form of this governing equation as

$$c(\boldsymbol{y})T(\boldsymbol{y}) = \int_{\Gamma} T^*(\boldsymbol{x},\boldsymbol{y})q(\boldsymbol{x})d\Gamma - \int_{\Gamma} T(\boldsymbol{x})q^*(\boldsymbol{x},\boldsymbol{y})d\Gamma \tag{2.1}$$

where, $\boldsymbol{y}$ (x_s, y_s) is the source point, $\boldsymbol{x}$ (x_f, y_f) is the field point, $c(\boldsymbol{y})$ takes on a value of 1.0 when the source point is inside the domain and a value of 0.5 for smooth boundaries without sharp corners, and T^* and q^* are the fundamental solutions for temperature and directional derivative respectively.

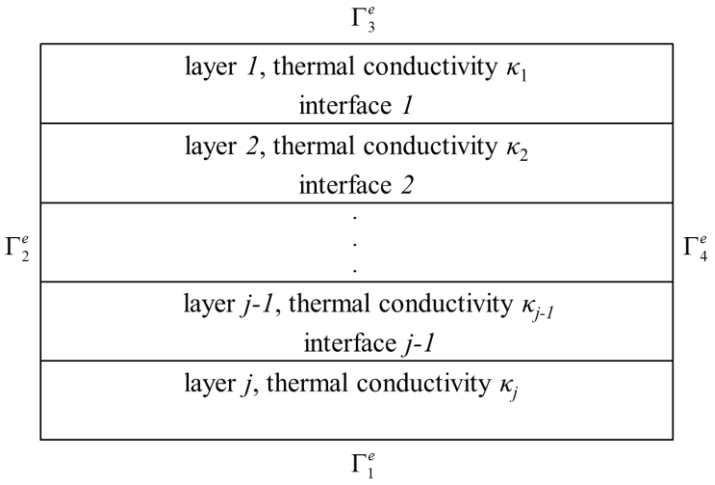

Fig. 2.1 Illustration of multiple layers media model ($j \geq 3$)

Herein, the fundamental solution satisfies the Laplace's equation and denotes the field due to a unit source in an infinite space. As for an isotropic two-dimensional medium, the fundamental solution and its derivative are expressed as (Brebbia and Dominguez, 1992 and Gao, 2006)

$$\begin{cases} T^* = \dfrac{1}{2\pi}\ln\left(\dfrac{1}{r}\right) \\ q^* = \dfrac{\partial T^*}{\partial \vec{n}} = \dfrac{1}{2\pi r^2}\left((x_s - x_f)n_x + (y_s - x_f)n_y\right) \end{cases} \tag{2.2}$$

where, $n = (n_x, n_y)$ is the unit outward normal vector to the boundary Γ in Eq. (2.1), and r is the distance between the source point and the field point in Eq. (2.1).

According to Fourier's law, heat flux on the boundary of each problem domain is the product of the thermal conductivity and the directional derivative. The directional derivative is chosen as the independent variable instead of the heat flux.

Transforming the partial differential equation into a boundary integral equation is

the first critical step of BEM. Besides, discretizing the boundary element is the other crucial technique. In this formulation the quadratic element comprising of three nodes is adopted to discretize domain boundaries. Analogous with an isoparametric element used in FEM, the same concept is utilized for BEM. Quadratic functions are introduced for both the coordinate transformation and interpolations of temperature and derivative in each boundary element. For a 2D problem, the transformation of Cartesian coordinate to natural coordinates is shown in Fig. 2.2. The interpolations are of the form

$$\begin{cases} x = \phi_1 x_1 + \phi_2 x_2 + \phi_3 x_3 \\ y = \phi_1 y_1 + \phi_2 y_2 + \phi_3 y_3 \end{cases} \qquad \begin{cases} T = \phi_1 T_1 + \phi_2 T_2 + \phi_3 T_3 \\ q = \phi_1 q_1 + \phi_2 q_2 + \phi_3 q_3 \end{cases} \tag{2.3}$$

where, $\phi_1 = \xi(\xi - 1)/2$, $\phi_2 = (1-\xi)(1+\xi)$, and $\phi_3 = \xi(\xi + 1)/2$ are the shape functions, (x_1,y_1), (x_2,y_2), and (x_3,y_3) are boundary nodes, T_1, T_2 and T_3 are nodal temperatures, q_1, q_2, and q_3 are nodal directional derivative in the direction of outward normal at nodes of a boundary element.

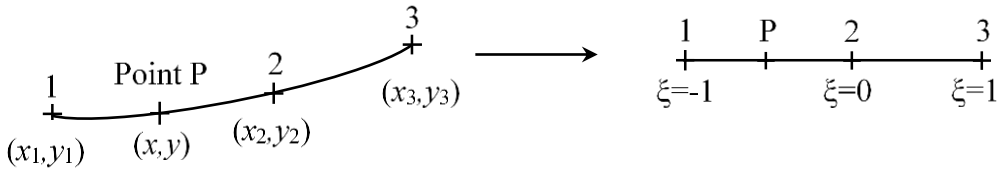

Fig. 2.2 The coordinate transformation of a quadratic element

When the boundary has been discretized into quadratic elements, the boundary integral equation Eq. (2.1) can be rewritten as

$$c(\boldsymbol{y})T(\boldsymbol{y}) + \sum_{n=1}^{NE} \int_{\Gamma_n} Tq^* d\Gamma = \sum_{n=1}^{NE} \int_{\Gamma_n} T^* q d\Gamma \tag{2.4}$$

where, *NE* is the number of boundary elements, and Γ_n is the n^{th} element.

It should be pointed out that both the temperature and heat flux should be continuous inside an element. While the temperature has a single value at the node possessed by two adjacent elements, the heat flux may be different. According to Eq. (2.4) and boundary conditions, one can obtain all the unknown boundary values, and then the temperature and heat flux at any point of interest inside the domain can be evaluated.

By substituting Eq. (2.3) into Eq. (2.4), the line integration can be transformed into a one dimensional integration referring to the ξ-coordinate as follows

$$c^i T^i + \sum_{n=1}^{NE} \int_{\Gamma_n} \begin{bmatrix} \phi_1 & \phi_2 & \phi_3 \end{bmatrix} q^* J d\xi \begin{bmatrix} T_1^n \\ T_2^n \\ T_3^n \end{bmatrix} = \sum_{n=1}^{NE} \int_{\Gamma_n} \begin{bmatrix} \phi_1 & \phi_2 & \phi_3 \end{bmatrix} T^* J d\xi \begin{bmatrix} q_1^n \\ q_2^n \\ q_3^n \end{bmatrix} \tag{2.5}$$

where, "*i*" denotes source point, $J = \sqrt{\left(\frac{dx}{d\xi}\right)^2 + \left(\frac{dy}{d\xi}\right)^2}$ is the Jacobian in the coordinate transformation, and *n* represents the n^{th} boundary element. By introducing the following boundary integral equations, Eq. (2.5) will be further simplified for later formulation

$$\begin{cases} h_m^{in} = \int_{\Gamma_n} \phi_m q^* J d\xi \\ g_m^{in} = \int_{\Gamma_n} \phi_m T^* J d\xi \end{cases} \tag{2.6}$$

where, h_m^{in} and g_m^{in} are the influence coefficients.

Regarding the evaluation of these influence coefficients using the collocation

BEM (Brebbia and Dominguez, 1992), which is adopted in the theoretical formulation, two scenarios must be considered. One scenario is that the collocation point doesn't coincide with any boundary node on one boundary element and the other one is that the collocation point coincides with any one of the three boundary nodes on one quadratic element.

2.2.1 Collocation point is outside the nth element

Consider the first case when the collocation point is not one of the three nodes of the n^{th} boundary element. Suppose that the collocation point "*i*" (source point) is (x_s, y_s) and then the integration point (x_t^n, y_t^n) in the n^{th} element can be interpolated by Eq. (2.3)

$$\begin{cases} x_t^n = \frac{1}{2}\xi^2(x_1^n - x_2^n + x_3^n) + \frac{1}{2}\xi(x_3^n - x_1^n) + x_2^n \\ y_t^n = \frac{1}{2}\xi^2(y_1^n - y_2^n + y_3^n) + \frac{1}{2}\xi(y_3^n - y_1^n) + y_2^n \end{cases} \tag{2.7}$$

Consequently, the first derivative of Eq. (2.7) in respect of ξ are written as

$$\begin{cases} \frac{dx_t^n}{d\xi} = \xi(x_1^n - x_2^n + x_3^n) + \frac{1}{2}(x_3^n - x_1^n) \\ \frac{dy_t^n}{d\xi} = \xi(y_1^n - y_2^n + y_3^n) + \frac{1}{2}(y_3^n - y_1^n) \end{cases} \tag{2.8}$$

Let $\vec{n}^n = (n_x^n, n_y^n)$ denote the unit normal at this integration point on the n^{th} element. The unit normal must be evaluated for each integration point in each element.

$$\begin{cases} n_x^n = \dfrac{1}{J}\dfrac{dy_t^n}{d\xi} \\ n_y^n = -\dfrac{1}{J}\dfrac{dx_t^n}{d\xi} \end{cases} \tag{2.9}$$

where, $J = \sqrt{[\xi(x_1^n - x_2^n + x_3^n) + \frac{1}{2}(x_3^n - x_1^n)]^2 + [\xi(y_1^n - y_2^n + y_3^n) + \frac{1}{2}(y_3^n - y_1^n)]^2}$.

Substitute Eq. (2.2) and Eq. (2.9) into Eq. (2.6) resulting in

$$\begin{aligned} h_m^{in} &= -\frac{1}{2\pi} \cdot \int_{\Gamma_n} \frac{\phi_m}{(x_t^n - x_s)^2 + (y_t^n - y_s)^2} \cdot \left[(x_t^n - x_s)\frac{dy_t^n}{d\xi} - (y_t^n - y_s)\frac{dx_t^n}{d\xi} \right] d\xi \\ g_m^{in} &= -\frac{1}{4\pi} \cdot \int_{\Gamma_n} \phi_m \cdot \ln\left[(x_t^n - x_s)^2 + (y_t^n - y_s)^2 \right] J d\xi \end{aligned} \tag{2.10}$$

2.2.2 Collocation point is one of the three nodes

When the collocation point coincides with any of the three nodes of one quadratic element, a local coordinate system $x_L o y_L$ and a third natural η-coordinate, which is associated with the natural ξ-coordinate are needed in order to treat the singularity in the numerical integration. For the quadratic element, there are three different cases for this local η-coordinate.

When the origin of the local coordinate coincides with the first node of a boundary element, the local coordinate and a third natural coordinate are presented in Fig. 2.3.

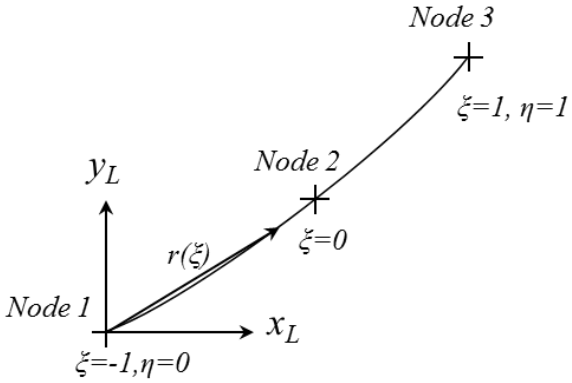

Fig. 2.3 The origin of the local coordinate locates at the first node of n^{th} element

To be consistent, take the n^{th} element for example. The local coordinates of the three nodes on the n^{th} element can be expressed as

$$\begin{cases} x_{L1} = 0 \\ y_{L1} = 0 \end{cases}, \begin{cases} x_{L2} = x_2^n - x_1^n \\ y_{L2} = y_2^n - y_1^n \end{cases}, \begin{cases} x_{L3} = x_3^n - x_1^n \\ y_{L3} = y_3^n - y_1^n \end{cases} \tag{2.11}$$

The interpolation functions under this coordinates using Eq. (2.3) are written as

$$\begin{cases} x_L(\xi) = \phi_2 x_{L2} + \phi_3 x_{L3} = (1+\xi)(A_1\xi + B_1) \\ y_L(\xi) = \phi_2 y_{L2} + \phi_3 y_{L3} = (1+\xi)(A_2\xi + B_2) \end{cases} \tag{2.12}$$

where, $A_1 = (x_{L3} - 2x_{L2})/2$, $B_1 = x_{L2}$, $A_2 = (y_{L3} - 2y_{L2})/2$, and $B_1 = y_{L2}$.

The distance between the collocation point and the integration point $r(\xi)$ is expressed as

$$r(\xi) = (1+\xi)\sqrt{(A_1\xi + B_1)^2 + (A_2\xi + B_2)^2} \tag{2.13}$$

Since a new reference coordinate is introduced, Eq. (2.2) should be derived in the new coordinate system which can be expressed as

$$q^* = \frac{\partial u^*}{\partial n} = \frac{\partial u^*}{\partial r} \cdot \frac{\partial r}{\partial n} = -\frac{1}{2\pi J} \cdot \frac{A_2 B_1 - B_2 A_1}{\left(A_1\xi + B_1\right)^2 + \left(A_2\xi + B_2\right)^2} \tag{2.14}$$

where, $\frac{\partial r}{\partial n} = \frac{1}{J \cdot r}\left(x_L \frac{dy_L}{d\xi} - y_L \frac{dx_L}{d\xi} \right)$ and $J = \sqrt{(2A_1\xi + A_1 + B_1)^2 + (2A_2\xi + A_2 + B_2)}$.

Finally, the influence coefficients h_m^{in} and g_m^{in} for the n^{th} element are as follows

$$\begin{aligned}
h_m^{in} &= -\frac{1}{2\pi}\int_{\Gamma_n} \frac{\phi_m (A_2 B_1 - B_2 A_1)}{(A_1\xi + B_1)^2 + (A_2\xi + B_2)^2} d\xi \\
g_m^{in} &= \frac{1}{2\pi}\lim_{\varepsilon\to 0}\int_{-1+\varepsilon}^{1} \phi_m \cdot J \cdot \ln\left[\frac{1}{(1+\xi)\sqrt{(A_1\xi + B_1)^2 + (A_2\xi + B_2)^2}} \right] d\xi \\
&= \frac{1}{2\pi}\int_{-1}^{1} \phi_m \cdot J \cdot \ln\left[\frac{1}{2\sqrt{(A_1\xi + B_1)^2 + (A_2\xi + B_2)^2}} \right] d\xi \\
&\quad + \frac{1}{\pi}\lim_{\varepsilon\to 0}\int_{\varepsilon}^{1} \phi_m(\eta) \cdot J_1(\eta) \cdot \ln\left(\frac{1}{\eta}\right) d\eta
\end{aligned} \tag{2.15}$$

where, $\eta = (1+\xi)/2$, $\phi_1(\eta) = (\eta - 1)(2\eta - 1)$, $\phi_2 = 4\eta(1-\eta)$, $\phi_3 = \eta(2\eta - 1)$, and $J_1(\eta) = \sqrt{(4A_1\eta - A_1 + B_1)^2 + (4A_2\eta - A_2 + B_2)^2}$ in the last term of g_m^{in}. The last term of g_m^{in} can be numerically computed by the logarithmic Gauss quadrature integration (Brebbia and Dominguez, 1992).

The local coordinate and a third natural coordinate are presented in Fig. 2.4 when the origin of the local coordinate coincides with the middle node of a boundary element.

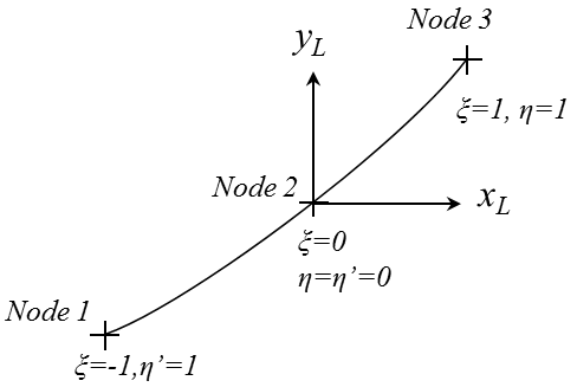

Fig. 2.4 The origin of the local coordinate locates at the middle node of n^{th} element

In order to numerically evaluated h_m^{in} and g_m^{in} in Eq. (2.6), the element is divided into two parts due to the setup of the local coordinate. In the interest of simplicity, these two terms can be written as

$$\begin{cases} h_m^{in} = \int_{Node1}^{Node2} \phi_m q^* J d\xi + \int_{Node2}^{Node3} \phi_m q^* J d\xi \\ g_m^{in} = \int_{Node1}^{Node2} \phi_m T^* J d\xi + \int_{Node2}^{Node3} \phi_m T^* J d\xi \end{cases} \tag{2.16}$$

Investigate the integration between node 2 and node 3 shown in Fig. 2.4 first. Similarly, the local coordinates of the three nodes can be expressed as

$$\begin{cases} x_{L1} = x_1^n - x_2^n \\ y_{L1} = y_1^n - y_2^n \end{cases}, \begin{cases} x_{L2} = 0 \\ y_{L2} = 0 \end{cases}, \begin{cases} x_{L3} = x_3^n - x_2^n \\ y_{L3} = y_3^n - y_2^n \end{cases} \tag{2.17}$$

Then the coordinate transformation functions are as follows

$$\begin{cases} x_L(\xi) = \phi_1 x_{L1} + \phi_3 x_{L3} = \frac{1}{2}\xi(A_1\xi + B_1) \\ y_L(\xi) = \phi_1 y_{L1} + \phi_3 y_{L3} = \frac{1}{2}\xi(A_2\xi + B_2) \end{cases} \tag{2.18}$$

where, $A_1 = x_{L1} + x_{L3}$, $B_1 = x_{L3} - x_{L1}$, $A_2 = y_{L1} + y_{L3}$ and $B_2 = y_{L3} - y_{L1}$.

Subsequently, $r(\xi)$ can be written as

$$r(\xi) = \frac{1}{2}\xi\sqrt{(A_1\xi + B_1)^2 + (A_2\xi + B_2)^2} \tag{2.19}$$

Considering another coordinate transformation between the ξ-coordinate and η-coordinate $\eta = \xi$, the shape function is expressed in the η-coordinate as follows

$$\begin{cases} \phi_1(\eta) = \eta(\eta - 1)/2 \\ \phi_2(\eta) = 1 - \eta^2 \\ \phi_3(\eta) = \eta(\eta + 1)/2 \end{cases} \tag{2.20}$$

Finally, substitute Eq. (2.9), Eq. (2.18), Eq. (2.19) and Eq. (2.20) into Eq. (2.16) resulting in h_m^{in} and g_m^{in} in the section between node 2 and node 3 as shown in Fig. 2.4.

$$\begin{aligned} h_{m|2-3}^{ij} &= \int_{Node2}^{Node3} \phi_m q^* J d\xi = -\frac{1}{2\pi}\int_0^1 \frac{\phi_m(A_2B_1 - B_2A_1)}{(A_1\xi + B_1)^2 + (A_2\xi + B_2)^2} d\xi \\ g_{m|2-3}^{ij} &= \int_{Node2}^{Node3} \phi_m T^* J d\xi = \lim_{\varepsilon\to 0}\int_\varepsilon^1 \phi_m T^* J d\xi \\ &= -\frac{1}{4\pi}\int_0^1 \phi_m(\xi)\cdot J(\xi)\cdot \ln\left[\frac{1}{4}(A_1\xi + B_1)^2 + \frac{1}{4}(A_2\xi + B_2)^2\right] d\xi \\ &\quad + \frac{1}{2\pi}\lim_{\varepsilon\to 0}\int_\varepsilon^1 \phi_m(\eta)\cdot J_2(\eta)\cdot \ln\left(\frac{1}{\eta}\right) d\eta \end{aligned} \tag{2.21}$$

where, $J(\xi) = \sqrt{\left(A_1\xi + \frac{B_1}{2}\right)^2 + \left(A_2\xi + \frac{B_2}{2}\right)^2}$ and $J_2(\eta) = \sqrt{\left(A_1\eta + \frac{B_1}{2}\right)^2 + \left(A_2\eta + \frac{B_2}{2}\right)^2}$.

Note that the last term of g_m^{in} can be evaluated by the logarithmic Gauss quadrature integration. See for examples Brebbia and Dominguez, 1992 and París and Cañas, 1997.

And then by substituting Eq. (2.6) into Eq. (2.5) one can obtains the discrete form of the governing equation

$$c^i T^i + \sum_{n=1}^{NE}\sum_{m=1}^{3} h_m^{in} T_m^n = \sum_{n=1}^{NE}\sum_{m=1}^{3} g_m^{in} q_m^n \tag{2.22}$$

where, *NE* is the number of boundary elements, T_m^n and q_m^n correspond to the nodal temperature and directional derivative at the m^{th} node of the n^{th} element respectively.

When a source point coincides with a node, i.e. h_m^{in} and g_m^{in}, their values are numerically evaluated using the local coordinates, see for example Parés and Cañas (1997). The formulations are also derived in detail here, which are consistent with the notation used in this dissertation. One can rewrite the resulting equations in matrix form and solve for the unknown temperatures and derivatives at boundary nodes.

$$HT = GQ \tag{2.23}$$

where, $T = [t_1, t_2, \cdots, t_{2*NE}]$ is the temperature vector, $Q = [q_1, q_2, \cdots, q_{3*NE}]$ is the derivative vector, and *NE* is the number of boundary elements.

When all the unknown temperature and heat flux are solved, the temperature in a field point can be achieved by Eq. (2.7). Furthermore, the directional derivatives at the internal point "*i*" can be obtained

$$\begin{cases} q_x = \sum_{n=1}^{NE} \int_{\Gamma_n} [\phi_1 \quad \phi_2 \quad \phi_3] \dfrac{\partial T^*}{\partial x} Jd\xi \begin{bmatrix} q_1^n \\ q_2^n \\ q_3^n \end{bmatrix} - \sum_{n=1}^{NE} \int_{\Gamma_n} [\phi_1 \quad \phi_2 \quad \phi_3] \dfrac{\partial q^*}{\partial x} Jd\xi \begin{bmatrix} T_1^n \\ T_2^n \\ T_3^n \end{bmatrix} \\ q_y = \sum_{n=1}^{NE} \int_{\Gamma_n} [\phi_1 \quad \phi_2 \quad \phi_3] \dfrac{\partial T^*}{\partial y} Jd\xi \begin{bmatrix} q_1^n \\ q_2^n \\ q_3^n \end{bmatrix} - \sum_{n=1}^{NE} \int_{\Gamma_n} [\phi_1 \quad \phi_2 \quad \phi_3] \dfrac{\partial q^*}{\partial y} Jd\xi \begin{bmatrix} T_1^n \\ T_2^n \\ T_3^n \end{bmatrix} \end{cases} \tag{2.24}$$

where, $\dfrac{\partial u^*}{\partial x}$, $\dfrac{\partial u^*}{\partial y}$, $\dfrac{\partial q^*}{\partial x}$, and $\dfrac{\partial q^*}{\partial y}$ are function of ξ.

For the piecewise homogeneous medium presented in Fig. 2.1, Eq. (2.8) is applied to each layer and one global matrix can be assembled from all sub-matrices based upon the continuity of temperature and heat flux on the interfaces between two adjacent layers. To accomplish this step, the columns of H and G matrices for each layers are grouped based upon the external boundary nodes and the interface nodes as follows

$$\begin{bmatrix} H_1^e & H_1^{\Gamma_1} \end{bmatrix} \begin{Bmatrix} T_1^e \\ T_1^{\Gamma_1} \end{Bmatrix} = \begin{bmatrix} G_1^e & G_1^{\Gamma_1} \end{bmatrix} \begin{Bmatrix} q_1^e \\ q_1^{\Gamma_1} \end{Bmatrix} \tag{2.25}$$

$$\begin{bmatrix} H_2^e & H_2^{\Gamma_1} & H_2^{\Gamma_2} \end{bmatrix} \begin{Bmatrix} T_2^e \\ T_2^{\Gamma_1} \\ T_2^{\Gamma_2} \end{Bmatrix} = \begin{bmatrix} G_2^e & G_2^{\Gamma_1} & G_2^{\Gamma_2} \end{bmatrix} \begin{Bmatrix} q_2^e \\ q_2^{\Gamma_1} \\ q_2^{\Gamma_2} \end{Bmatrix} \tag{2.26}$$

$$\begin{bmatrix} H_{j-1}^e & H_{j-1}^{\Gamma_{j-2}} & H_{j-1}^{\Gamma_{j-1}} \end{bmatrix} \begin{Bmatrix} T_{j-1}^e \\ T_{j-1}^{\Gamma_{j-2}} \\ T_{j-1}^{\Gamma_{j-1}} \end{Bmatrix} = \begin{bmatrix} G_{j-1}^e & G_{j-1}^{\Gamma_{j-2}} & G_{j-1}^{\Gamma_{j-1}} \end{bmatrix} \begin{Bmatrix} q_{j-1}^e \\ q_{j-1}^{\Gamma_{j-2}} \\ q_{j-1}^{\Gamma_{j-1}} \end{Bmatrix} \tag{2.27}$$

$$\begin{bmatrix} H_j^e & H_j^{\Gamma_{j-1}} \end{bmatrix} \begin{Bmatrix} T_j^e \\ T_j^{\Gamma_{j-1}} \end{Bmatrix} = \begin{bmatrix} G_j^e & G_j^{\Gamma_{j-1}} \end{bmatrix} \begin{Bmatrix} q_j^e \\ q_j^{\Gamma_{j-1}} \end{Bmatrix} \tag{2.28}$$

where, the subscript j means that a node is at the j^{th} layer, the superscript e means that a node is on the external boundary, and the superscript Γ means node is on the j^{th} interface.

Since the direction of the external boundary of each layer is counterclockwise, the direction of the interface and the outward normal direction to the interface of two adjacent layers are opposite to each other. Assuming that (1) these directions of $j\text{-}1^{th}$ layer's $j\text{-}1^{th}$ interface following $j\text{-}1^{th}$ layer, and (2) these direction of j^{th} layer's $j\text{-}1^{th}$ interface refers to that of $j\text{-}1^{th}$ layer, the interface information can be defined once in the

input file. Thus, the issue pointed out by Gao and Wang (2009) that interface information has to be read twice in MDBEM has been resolved in the LBEM, which is read one time and will be elaborated in detail in the following section.

In order to deal with discontinuous prescribed heat fluxes on boundaries, each quadratic element is assigned three derivative terms, which are directly related with heat fluxes in Eq. (2.8). Following the direction of boundary, the heat flux in the upstream direction is called flux before a node and the other in the downstream direction is called flux after a node. However, the heat flux is continuous at the joint node of two neighboring elements for those interfacial nodes. Thus, the columns of G corresponding to interfacial nodes should be collected at the joint nodes in Eq. (2.10) thru. Eq. (2.13), which is termed as CG after the collection operation.

Next, CG and the columns of H associated with interfacial nodes should be reordered according to the order of boundary nodes before assembling into a global matrix. Then, some CG matrices are denoted as IG, where some columns of CG are reordered.

Subsequently, by introducing the continuity conditions of temperature and heat flux on the interfaces of two adjacent layers, the global algebraic system equation for multilayers model can be achieved as follows

$$\begin{bmatrix} H_1^e & & & & H_1^{\Gamma_1} & & & \\ & H_2^e & \ddots & & IH_2^{\Gamma_1} & H_2^{\Gamma_2} & \cdots & \\ & & H_{j-1}^e & & & & IH_{j-1}^{\Gamma_{j-2}} & H_{j-1}^{\Gamma_{j-1}} \\ & & & H_j^e & & & & IH_j^{\Gamma_{j-1}} \end{bmatrix}$$

$$\begin{bmatrix} -CG_1^{\Gamma_1} & & & & \\ \frac{\kappa_1}{\kappa_2} IG_2^{\Gamma_1} & -CG_2^{\Gamma_2} & & & \\ & \cdots & & & \\ & & \frac{\kappa_{j-2}}{\kappa_{j-1}} IG_{j-1}^{\Gamma_{j-2}} & -CG_{j-1}^{\Gamma_{j-1}} & \\ & & & \frac{\kappa_{j-1}}{\kappa_j} IG_j^{\Gamma_{j-1}} & \end{bmatrix} \begin{Bmatrix} T_1^e \\ T_2^e \\ \vdots \\ T_{j-1}^e \\ T_j^e \\ T_1^{\Gamma_1} \\ T_2^{\Gamma_2} \\ \vdots \\ T_{j-2}^{\Gamma_{j-2}} \\ T_{j-1}^{\Gamma_{j-1}} \\ cq_1^{\Gamma_1} \\ cq_2^{\Gamma_2} \\ \vdots \\ cq_{j-2}^{\Gamma_{j-2}} \\ cq_{j-1}^{\Gamma_{j-1}} \end{Bmatrix} = \begin{bmatrix} G_1^e & & & & \\ & G_1^e & \ddots & & \\ & & & G_{j-1}^e & \\ & & & & G_j^e \end{bmatrix} \begin{Bmatrix} q_1^e \\ q_2^e \\ \vdots \\ q_{j-1}^e \\ q_j^e \end{Bmatrix}$$

(2.29)

where, the κ_j is the thermal conductivity of the j^{th} layer, and $cq_{j-1}^{\Gamma_{j-1}}$ is the collected nodal derivative vector of j-1^{th} layer's j-1^{th} interface.

By substituting boundary conditions into Eq. (2.14), all unknowns on the external boundary as well as the temperature and heat flux on interfaces can be obtained. And then Eq. (2.7) is used to compute temperature for each layer. Moreover, the internal heat flux can be reached by Eq. (2.9).

Additionally, an interpolation scheme is utilized to treat the node with flux discontinuity at a corner as depicted in Fig. 2.5. When a corner exists at certain boundary nodes, the normal heat fluxes cannot be obtained by Eq. (2.8) directly because of two unknowns existing at one boundary node. Since heat flux is related with the

gradient of temperature via Fourier's law, temperature in the neighboring domain around the discontinuous node can be interpolated by the three nodal values in the vicinity of this corner as shown in Fig. 2.5.

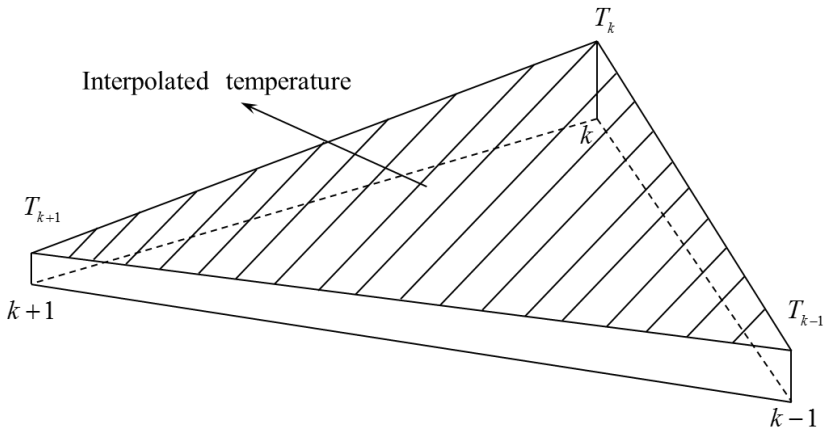

Fig. 2.5 Linear interpolation of temperature at a corner

It is assumed that the node with heat flux discontinuity is node k and two neighboring nodes are termed as node k-1 and node k+1. Since temperatures at the three nodes are independent variables, the temperature distribution can be linearly interpolated at this corner. Then, the normal derivatives before node k and after node k depend on the temperature gradient at this node as illustrated in Fig. 2.6. In the interest of simplicity, letting $x_2 = x_{k-1}$, $y_2 = y_{k-1}$, $x_3 = x_k$, $y_3 = y_k$, $x_4 = x_{k+1}$, $T_2 = T_{k-1}$, $T_3 = T_k$, and $T_4 = T_{k+1}$, the interpolated temperature field can be expressed as

$$\begin{vmatrix} x - x_3 & y - y_3 & T - T_3 \\ x_2 - x_3 & y_2 - y_3 & T_2 - T_3 \\ x_4 - x_3 & y_4 - y_3 & T_4 - T_3 \end{vmatrix} = 0 \tag{2.30}$$

Then the gradient of temperature can be derived from Eq. (2.15) as

$$\begin{cases} \dfrac{\partial T}{\partial x} = \dfrac{1}{D}\left\{(y_2 - y_3)(T_4 - T_3) - (y_4 - y_3)(T_2 - T_3)\right\} \\ \dfrac{\partial T}{\partial y} = \dfrac{1}{D}\left\{(x_4 - x_3)(T_2 - T_3) - (x_2 - y_3)(T_4 - T_3)\right\} \end{cases} \tag{2.31}$$

where, $D = (y_2 - y_3)(x_4 - x_3) - (x_2 - x_3)(y_4 - y_2)$.

Since the quadratic element is used as shown in Eq. (2.3), two boundary elements comprised of five nodes are employed in the interpolation. The directional derivatives with outward normal on each element before and after node k can be expressed by the normal directions on the two elements and the gradient via Eq. (2.16) at this node.

$$\begin{cases} q_{kb} = n_{kb} \cdot \nabla T \\ q_{ka} = n_{ka} \cdot \nabla T \end{cases} \tag{2.32}$$

where, n_{ka} and n_{kb} are the unit outward normal vectors before and after node k.

Since any point on a boundary element can be expressed by a local coordinate ξ, the unit normal before the node can be derived in the natural coordinate shown below

$$n_{kb} = \left(\frac{dy}{d\xi}\frac{1}{J}, -\frac{dx}{d\xi}\frac{1}{J} \right) \tag{2.33}$$

where, $\dfrac{dx}{d\xi} = \dfrac{1}{2}x_1 - 2x_2 + \dfrac{3}{2}x_3$, $\dfrac{dy}{d\xi} = \dfrac{1}{2}y_1 - 2y_2 + \dfrac{3}{2}y_3$, $x_1 = x_{k-2}$, $y_1 = y_{k-2}$ and $J = \sqrt{\left(\dfrac{dx}{d\xi}\right)^2 + \left(\dfrac{dy}{d\xi}\right)^2}$. Similarly, the unit normal after node k can be expressed as

$$n_{ka} = \left(\frac{dy}{d\xi}\frac{1}{J}, -\frac{dx}{d\xi}\frac{1}{J} \right) \tag{2.34}$$

where, $\frac{dx}{d\xi} = 2x_4 - \frac{3}{2}x_3 - \frac{1}{2}x_5$, $\frac{dy}{d\xi} = 2y_4 - \frac{3}{2}y_3 - \frac{1}{2}y_5$, $x_5 = x_{k+2}$, and $y_5 = y_{k+2}$.

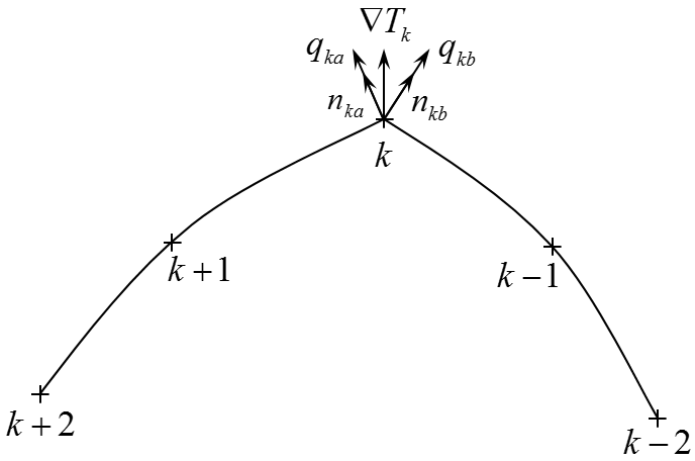

Fig. 2.6 Discontinuity of heat flux at a corner

2.3 Numerical Implementation

Regarding the regular topology of the layered medium model, a generalized numerical procedure, which is capable of solving heat conduction problems in multi-layers medium with all kinds of plausible boundary conditions, is proposed and elaborated here. Following the mathematical formulations shown in Eq. (2.25) thru. Eq. (2.34), one computer program called Layered Medium Boundary Element Method (LBEM) is designed and constructed for the two-dimensional heat transfer problem in Matlab. The program flow chart is now illustrated in Fig. 2.7.

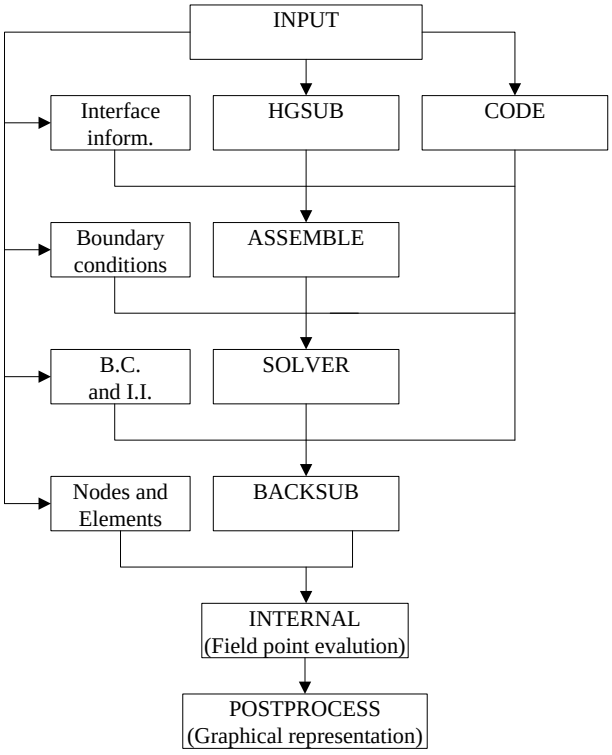

Fig. 2.7 Flow chart and modules of LBEM

LBEM is comprised of eight modules whose functionalities are stated herein. INPUT is designed to read BEM model information from a format *.txt file including the order and coordinates of boundary nodes, boundary elements, interface elements, interface directions, and material properties. In order to handle all kinds of boundary conditions, the type of boundary condition of each node must be identified and stored for three modules: ASSEMBLE, SOLVER and BACKSUB as shown in Fig. 2.7. CODE is utilized to identify and store the type of boundary and interfacial nodes using values listed in Tab. 2.1. HGSUB is used to compute H and G of each layer by Eq. (2.23). ASSEMBLE forms the global matrix which follows Eq. (2.24) thru. Eq. (2.29).

SOLVER solves the algebraic equation by substituting boundary conditions into Eq. (2.29). BACKSUB separates temperatures and derivatives from the solved unknowns and then stores temperatures and derivatives of boundary nodes in order of the sequence nodes for each layer. INTERNAL computes the temperature and heat flux at internal points of interest in each layer using Eq. (2.22) and Eq. (2.24). POSTPROCESS displays the temperature contour of specific BEM model and generates a family of curves for parametric study. Note that case 5 in Tab. 2.1 stands for the discontinuity of heat flux at corners of the BEM model. Linear extrapolation of temperature (París and Cañas, 1997) in the vicinity of this kind of corner is adopted in LBEM using Eq. (2.31).

Table 2.1 Identity of the B.C. type of a boundary node

ID	Temperature	Node before node	Node after node
1	unknown	known	known
2	known	unknown	known
3	known	unknown	known
4	known	unknown	unknown (continuous)
5	known	unknown	unknown (corner)
6	known	unknown	unknown (interface)
7	known	unknown (interface)	unknown
8	unknown	known	unknown (interface)
9	unknown	unknown (interface)	known
10	unknown	unknown (mid. node)	unknown (mid. node)
11	unknown	unknown (end node)	unknown (end node)

2.4 Program Validation

The numerical predictions obtained using the boundary element model were validated by comparing them to the predictions from FEM and IIBEM for the first

example (Gao et al., 2009) and FE program Code_Bright (UPC, 2013) for the second example. The unit of length is meter and the unit of temperature is Kelvin and Celsius for the first and the second problem respectively. Fig. 2.8 shows dimensions, boundary conditions and thermal conductivities of a two layers plate. The corresponding boundary element model is presented in Fig. 2.9 using the same mesh on boundaries and interface adopted in the FE and IIBEM analysis (Gao et al., 2009). The boundary element model consists of 24 quadratic elements for each layer and 38 elements for the whole model.

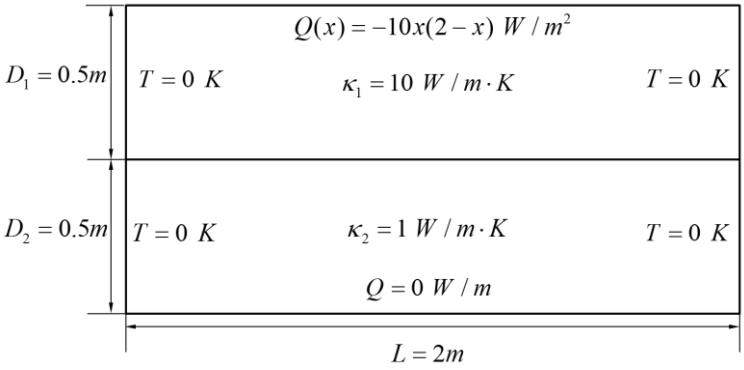

Fig. 2.8 Configuration and boundary conditions of two layers medium plate

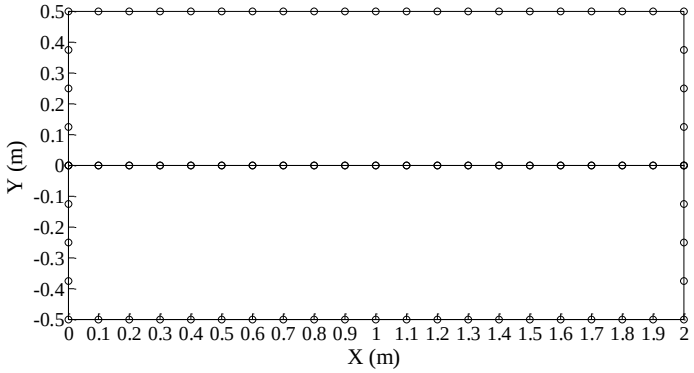

Fig. 2.9 Boundary element model of the two layers medium plate

Fig. 2.10 shows the temperature contour, which has the same pattern of temperature as the results obtained by IIBEM. Due to the fundamental solution, numerical results are not accurate when the distance between the evaluated internal point and boundary element is much less than the length of neighboring boundary elements. However, the temperature and heat flux are accurate and reliable as they are solved directly from the system equation when the mesh of the boundary and interface is fine enough and the aspect ratio issue doesn't arise (Yang et al., 2002).

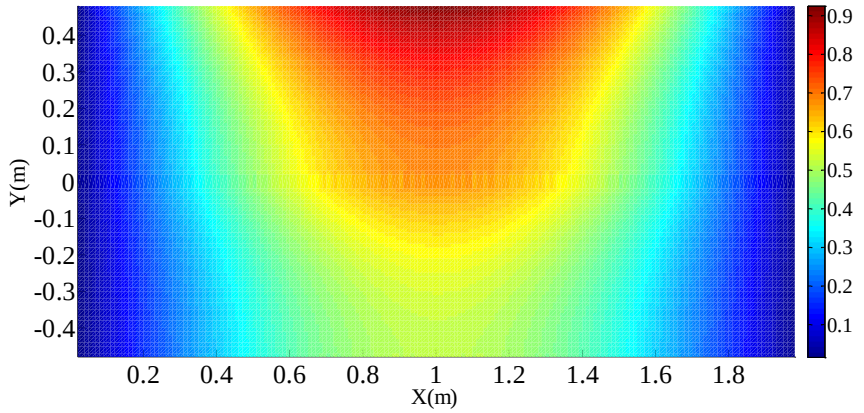

Fig. 2.10 Temperature distribution of two layers medium example (K)

Fig.2.11 and Fig. 2.12 show the temperatures along x=0.5 and x=1 using LBEM are provided in compared to IIBEM and FEM. Temperature distributions along y=0, x=0.5 and x=1.0 by IIBEM, FEM, and BEM are listed in Tab. 2.2 and Tab. 2.3 for comparison. The maximum relative error is 0.57% compared to FEM results. Additionally, interface boundary elements are input only once in LBEM compared to twice in MDBEM as commented by Gao et al. (2009).

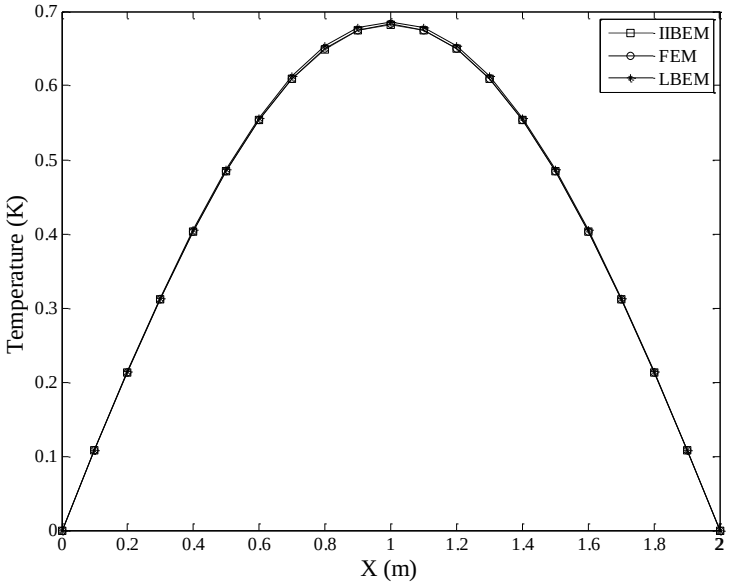

Fig. 2.11 Temperature distribution along y=0 of the two layers case

Table 2.2 Temperature along y=0 of two layers medium case

x	IIBEM	FEM	LBEM
0.0	0.00000	0.00000	0.00000
0.1	0.10761	0.10770	0.10823
0.2	0.21244	0.21262	0.21365
0.3	0.31181	0.31209	0.31358
0.4	0.40324	0.40359	0.40549
0.5	0.48449	0.48492	0.48717
0.6	0.55364	0.55414	0.55667
0.7	0.60910	0.60966	0.61240
0.8	0.64910	0.65021	0.65311
0.9	0.67428	0.67490	0.67789
1.0	0.68256	0.68319	0.68621
1.1	0.67428	0.67490	0.67789
1.2	0.64961	0.65021	0.65311
1.3	0.60910	0.60966	0.61240
1.4	0.55364	0.55414	0.55667
1.6	0.48449	0.48492	0.48717
1.7	0.40324	0.40359	0.40549
1.8	0.31181	0.31208	0.31358
1.9	0.21244	0.21262	0.21365
2.0	0.10761	0.10770	0.10823

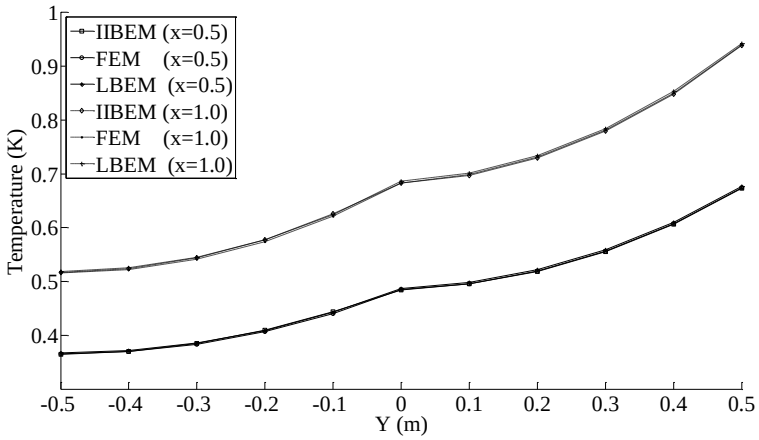

Fig. 2.12 Temperature distribution along x=0.5 and x=1 of the two layers example (K)

Table 2.3 Temperature along x=0.5 and x=1 of two layers medium case

y	x=0.5			x=1.0		
	IIBEM	FEM	LBEM	IIBEM	FEM	LBEM
0.5	0.67368	0.67438	0.67669	0.93861	0.93953	0.94257
0.4	0.60660	0.60773	0.61004	0.84870	0.85024	0.85328
0.3	0.55573	0.55667	0.55896	0.77989	0.78122	0.78425
0.2	0.51896	0.51980	0.52207	0.72981	0.73103	0.73406
0.1	0.49528	0.49610	0.49835	0.69740	0.69859	0.70161
0.0	0.48449	0.48492	0.48717	0.68256	0.68319	0.68621
-0.1	0.44351	0.44035	0.44253	0.62560	0.62112	0.62409
-0.2	0.40908	0.40684	0.40896	0.57775	0.57430	0.57723
-0.3	0.38483	0.38349	0.38558	0.54408	0.54164	0.54452
-0.4	0.37015	0.36973	0.37179	0.52384	0.52234	0.52521
-0.5	0.36504	0.36517	0.36724	0.51709	0.51596	0.51882

The second model shown in Fig. 2.13 is a two layered medium with an internal heat source located at the interface of two layers. Fig. 2.13 includes the dimensions, boundary conditions, and material properties.

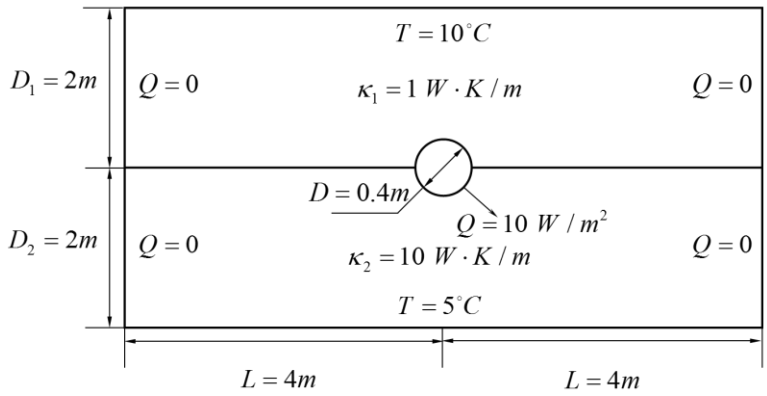

Fig. 2.13 Configuration of the two layers medium model with internal heat source

Fig. 2.14 and Fig. 2.15 illustrate the FEM mesh and BEM mesh details respectively. Note that the origin of coordinates is located at the center of the model, where the x-axis is in the horizontal direction and the y-axis is in the vertical direction. The FEM model had a total of 1580 nodes while the BEM model utilized only 230 nodes to accurately model the same problem. The number of equations to be solved was reduced by a factor on the order of 5~6 for the same mesh size on the model boundary.

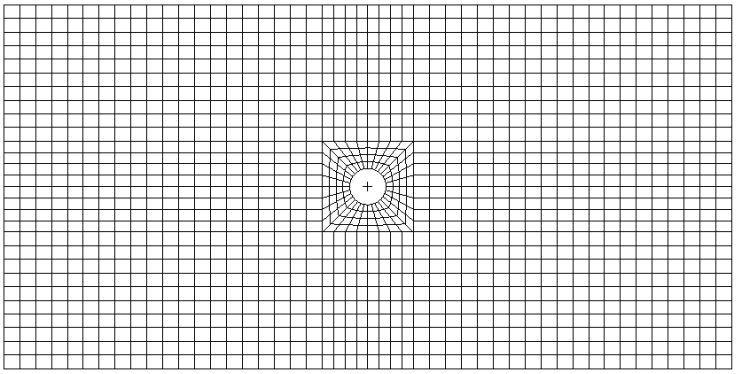

Fig. 2.14 FE model of the two layers medium model with internal heat source

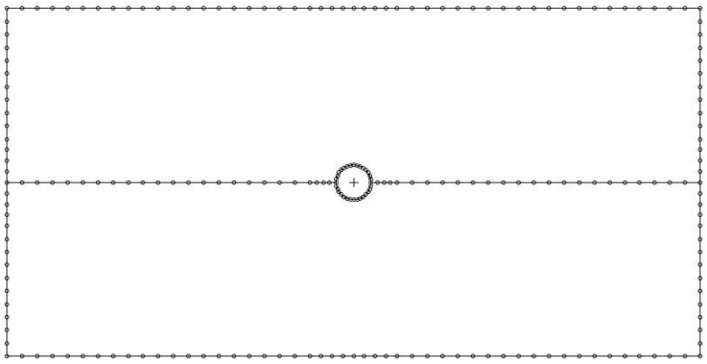

Fig. 2.15 BEM model of the two layers medium model with internal heat source

By matching the mesh on outermost boundaries, the maximum relative error was found to be less than one percent along the vertical axis at x=0 as illustrated in Fig. 2.16. The discontinuity shown in Fig. 2.16 resulted from the cavity at the interface of two layers. Temperature contours are shown in Fig. 2.17 and Fig. 2.18 using symmetric model via FEM and BEM with finer mesh on the boundary so as to obtain accurate results of the internal points close to the interface.

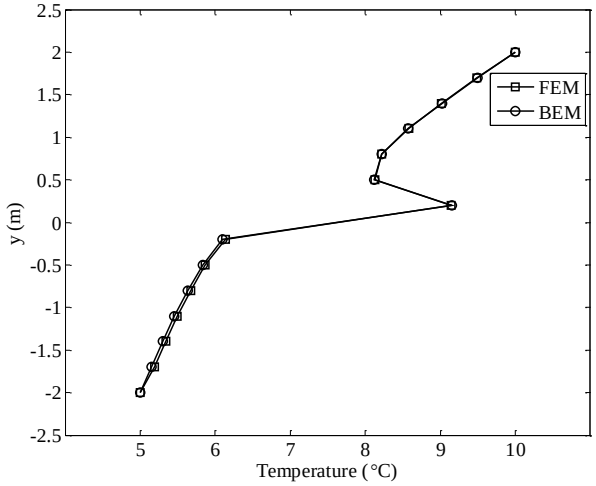

Fig. 2.16 Temperature distribution along x=0 from FEM and BEM results (˚C)

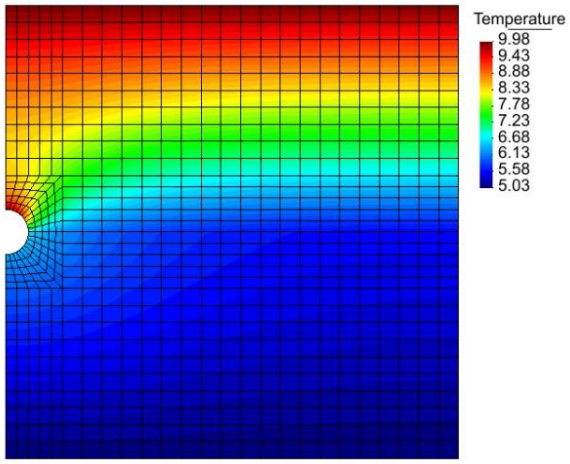

Fig. 2.17 Temperature distributions using symmetric model in Code_Bright

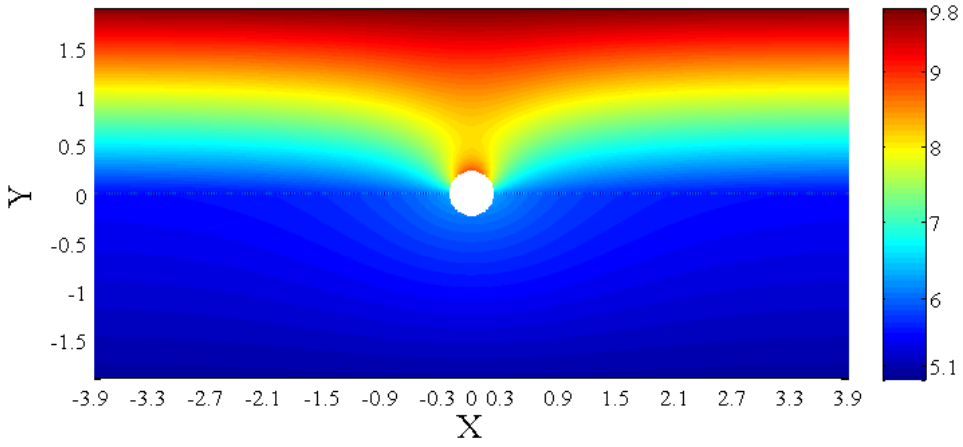

Fig. 2.18 Temperature distribution of the two layers medium model with internal heat source using BEM (˚C)

3. MODELING OF THERMAL FIELDS AROUND SUBSEA BURIED PIPELINES[*]

Heat transfer about buried subsea pipelines is a complex problem, the designers may consider multi-phase flows, coatings, thermal insulation, a necessary active heating plan, trenching and backfill, layered porous soils, routing and sea water depths in the process of design and validation of subsea pipelines especially for deepwater and arctic projects. The thermal field that develops and encompasses the buried pipeline is of critical concern from the point of view of flow assurance and structural safety. This significant temperature difference of mixture of oil and gas inside pipeline and the ambient seawater in deepwater poses some interesting design challenges on pipelines transporting hydrocarbons and associated impurities from reservoirs to collection sites. Depending on the circumstances, these pipelines may be buried for physical protection or for additional thermal insulation using a specially designed ROV. Burial provides an effective way of separating these pipelines from the strong cooling effect of cooler seawater caused by natural convection of seawater near pipelines (Osborne et al., 2001). Fig. 3.1 shows an illustration of deepwater ROV for pipeline burial and a photo of the duct trenched by this ROV is presented in Fig. 3.1 provided by Osborne et al. (2001).

[*] Part of the data reported in Section 3.1 of this chapter is reprinted with permission from "Numerical investigation of thermal fields around subsea buried pipelines" by Yanbin Bai, John M. Niedzwecki, and Marcelo Sanchez, 2014. *Proceedings of the ASME 2014 33rd International Conference on Ocean, Offshore and Arctic Engineering*, OMAE2014-24678, Copyright (2014) by ASME.

[*] Part of the data reported in Section 3.2 and 3.3 of this chapter is reprinted with permission from "Modeling of deepwater seabed steady-state thermal fields around buried pipeline including trenching and backfill effects" by Yanbin Bai and John M. Niedzwecki, 2014. *Computers and Geotechnics*, Volume 61, 221-229, Copyright (2014) by Elsevier B.V.

The process begins with the lay of a pipeline on the seafloor. Then an ROV rides along the pipeline digging a trench beneath it, and lowering it into the trench simultaneously shown in Fig. 3.2(a). To fully bury this pipe, sidewalls are collapsed by the ROV which causes a slump on the seabed illustrated in Fig. 3.2(b). Consequently, installation results in a domain with multiple domains and complex interfaces.

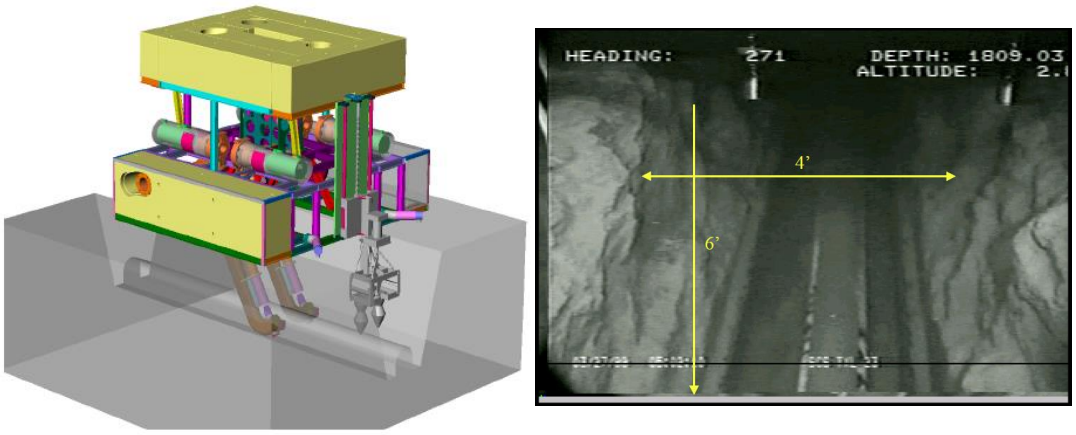

Fig. 3.1 ROV and photo of a deepwater burial project (Osborne et al., 2001)

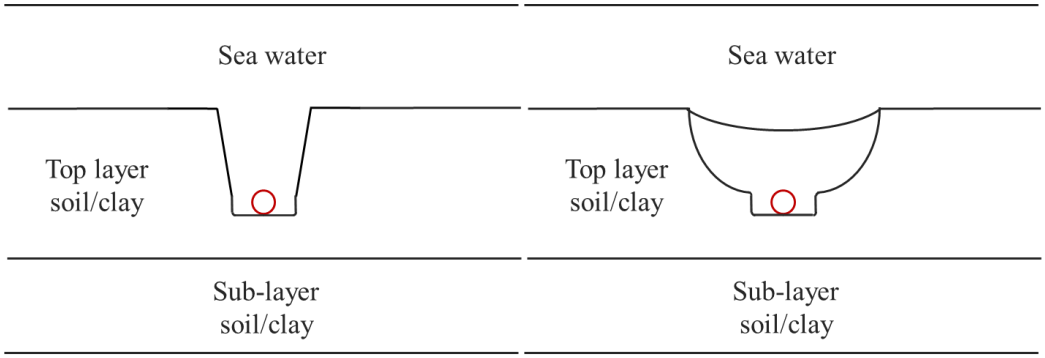

(a) Trenching and place pipe in duct (b) Simplified trench after backfilling

Fig. 3.2 Illustration of installation of a pipeline by an ROV

In the present study, a recently developed steady state two-dimensional boundary element model was used to investigate the thermal field surrounding buried pipelines. The domain of interest includes multiple domains and complex interfaces typically encountered in the actual installation such as trenching and backfill. As the submarine soil is partially or fully saturated porous media, the influence of natural convection even in marine clay with extreme low hydraulic permeability (10^{-8}~10^{-7} *m/s*) should be examined first. In order to establish the timeframe to achieve steady state conditions in the thermal field, a finite element code developed at the Technical University of Catalonia (2013) was used to conduct the natural convection simulation in a typical deepwater marine clay. The purpose of this FEM simulation is to scrutinize later assumption of the BEM formulation on the steady state heat transfer of buried pipelines.

The FEM results demonstrate that the fluid convection cell induced by temperature gradients in this marine clay affects the time required to reach the steady state but only slightly impacts the steady state temperature distributions in clay surrounding the buried pipeline. Subsequently, a boundary element model, incorporating layered seabed soils and conductive cooling effect of seawater near the seabed, was established. The BEM formulation further developed in Chapter 2 is updated according to the topology of multiple domains, which accounts for the installation issues. In terms of numerical investigation, the procedure proposed and elaborated in Chapter 2 is well suited to conduct a parametric study about the impacts of burial depth, backfilling and thermal power loss from the pipeline on the thermal fields.

3.1 FEM Investigation of Natural Convection in a Marine Clay

Regarding heat transfer in saturated porous media, Olivella et al. (1994) derived a set of mathematical formulas for the thermal-hydraulic-mechanical (THM) problem, which established the framework of Code_Bright (CB) (UPC, 2013) utilized in the current numerical study. CB adopts these assumptions: 1) thermal conductivity is independent of temperature; 2) the marine clay is a homogeneous isotropic porous media; 3) the marine clay is fully saturated; 4) the induced flow in clay is two dimensional and laminar; 5) the solid skeleton remains at rest; and 6) water contained in clay is not allowed to evaporate.

Along with the thermal conductive law (Fourier's law), the hydraulic conductive law (Darcy's law), initial conditions, and boundary conditions, the governing equations can be formulated and solved by FEM iteratively. In this thermal-hydraulic coupled problem, temperature and the liquid pressure are the two primary variables, which are formulated by the conservation of mass and energy. The coupling mechanism between the temperature and liquid flow is captured by an iterative scheme between the temperature and pressure at each time step in CB. The thermal constitutive law relates the conductive heat flux with the temperature gradient.

$$\boldsymbol{q} = -\kappa \nabla T \tag{3.1}$$

With the inclusion of compressibility of water, the hydraulic conductive law using the generalized Darcy's law, which correlates the liquid flow with the liquid pressure, is expressed in Eq. (3.2). The natural convection effect is driven by the buoyancy force resulted from the change of the density of seawater (Gebhart et al.,

1978) in marine clays as given in Eq. (3.2)

$$i_w|_z = -\frac{k_z}{\mu_w}\rho_{w0}g\left(-\alpha\left(T-T_0\right)+\beta\left(P_w-P_{w0}\right)\right) \tag{3.2}$$

where, k_z is the intrinsic permeability in z-direction.

In contrast, the conventional heat transfer equation describes the heat transfer problem in a solid medium. Governing equation for the heat transfer in a non-deformable homogeneous isotropic solid medium is given in Eq. (3.3).

$$\kappa\nabla^2 T + q_c = \rho c\frac{\partial T}{\partial t} \tag{3.3}$$

where, κ is the thermal conductivity, q_c is the internal heat source/sink term, ρ is mass density, c is the specific thermal capacity, T is temperature and t is time.

The thermal conductivity in fully saturated clay is defined as

$$\kappa_{sat} = \kappa_s^{1-\phi}\kappa_w^{\phi} \tag{3.4}$$

where, ϕ is the porosity of the marine clay.

By considering Fourier's law, temperature and conductive heat flux evolution can be obtained iteratively according to convergence of some nodal values in CB. To investigate the natural convection effect on the thermal field around buried pipelines, solid medium and porous medium case studies were performed and compared. Solid case simulation uses the thermal properties of fully saturated clay derived from the properties of solid and liquid phases of a marine clay as listed in Tab. 3.1. In addition, Tab. 3.1 summarizes some ambient parameters essential for these two FEM studies.

Table 3.1 Problem data: marine clay properties and ambient parameters

	Name	Symbol	Value	Unit
Solid media case	Thermal conductivity of saturated clay	κ_{sat}	0.92	*W/m K*
	Specific heat of saturated clay	c_{sat}	2237	*J/kg K*
	Density of saturated clay	ρ_{sat}	1327	*kg/m3*
Porous media case	Thermal conductivity of solid clay grain	κ_s	1.6	*W/m K*
	Specific heat of solid clay grain	c_s	800	*J/kg K*
	Density of solid clay grain	ρ_s	1800	*kg/m3*
	Reference density of seawater	ρ_{w0}	1025	*kg/m3*
	Thermal conductivity of seawater	κ_w	0.65	*W/m K*
	Specific heat of seawater	c_w	3850	*J/kg K*
	Thermal expansion coefficient of seawater	α	0.00034	$^{\circ}C^{-1}$
	Compressibility of seawater	β	0.00045	*MPa*
	Viscosity of seawater	μ_w	0.0018	*kg/m s*
	Porosity	ϕ	0.61	/
	Hydraulic permeability	K	1.0E-7	*m/s*
	Gravity	g	9.81	m/s^2
	Water depth	H	2750	*m*
	Ambient temperature	T_a	5	$^{\circ}C$

In the interest of simplicity, a simplified but representative 2-D pipe-soil model is adopted to study the natural convection effect on thermal field around a pipeline buried in marine clay as depicted in Fig. 3.3. The soil around buried pipe is assumed as a single homogeneous medium. Constant temperature on the seabed and lower bound of the truncated model are prescribed initially and the lateral heat flux conditions were the approximation of zero temperature gradient in the horizontal direction in the far field. Initial condition is selected as the ambient temperature as listed in Tab. 3.1. The heat flux dissipated from the heat pipeline is selected to be 20 W/m^2, which can be estimated from the thermal loss of the pipeline.

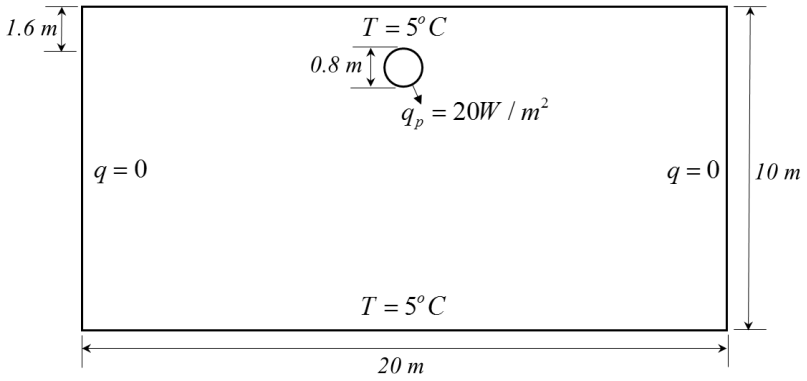

Fig. 3.3 2-D pipe-soil model for FE investigation

The FEM mesh of this model is illustrated in Fig. 3.4 with finer mesh in the vicinity of the pipe in order to guarantee numerical convergence and accuracy. This model has a total of 986 nodes and 920 quadrilateral elements.

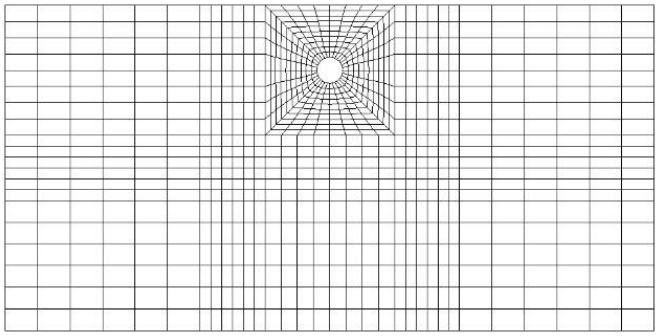

Fig. 3.4 FEM mesh of the pipe-soil model

According to the time evolution of temperature distribution in the problem domain, it is revealed that the time required for the porous case to reach the same temperature distribution is slightly longer than that of the solid media case as

demonstrated in Fig. 3.5. The natural convection cells developed around the pipeline contribute to this time lag.

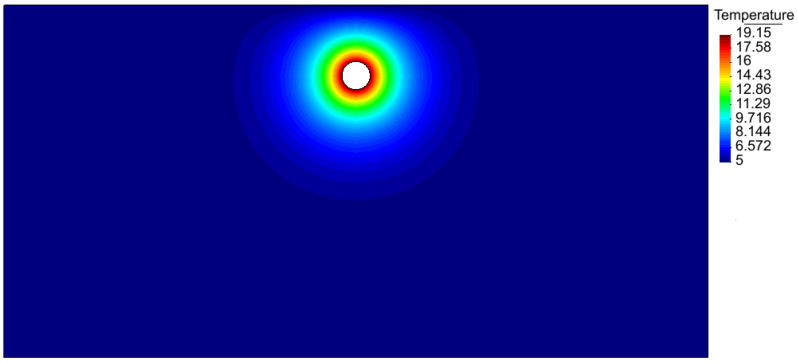

Fig. 3.5 Temperature distribution (˚C) for solid media case at 60 days and for porous media case at 63days

The nonlinear temperature rise in both the solid and porous case was observed from these simulations. It must be addressed that the burial depth has a critical influence on the time evolution history. The deeper the burial, the larger the time difference between these two cases. Regarding the convective liquid flow inside the clay in the problem domain, four convection cells were developed when the thermal field reached steady state. In this transient analysis, the thermal field in the porous media case is cooled down by the fluid flow driven by temperature gradients as shown in Fig. 3.6.

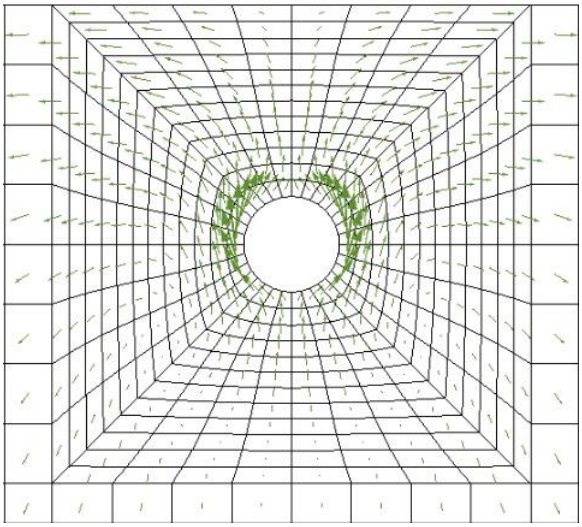

Fig. 3.6 Liquid flux around a buried pipe at 63 days for the porous media simulation

According to this comparative numerical study, it is recommended to include the natural convection in the transient analysis, including the start-up and cooling down operational modes, especially for soils with much larger hydraulic permeability such as silt and sand. While in the steady state evaluation, the cooling down effect of natural convection is not significant on the thermal field for this marine clay. Thus, it is reasonable to neglect this phenomenon in this marine clay used in the BEM investigation of the steady state thermal field.

3.2 BEM Formulation of Thermal Field about a Buried Pipeline

A 2-D vertical slice of the irregular sub-seafloor geometry that results from the trenching and backfilling processes is depicted in Fig. 3.7. The 2-D model includes consideration of both layered and disturbed marine soil conditions where the buried

pipeline is subject to high internal temperatures. This model encompasses four domains: two layers of undisturbed soils, a third coming from the backfilling, and the fourth containing seawater. In the model of the domain containing seawater adjacent to the seafloor, the fluid is assumed to be a hydraulically quiescent layer where the inclusion of seawater convection initiated in the seabed is neglected. The problem variables used in the formulation of the boundary element model are presented in Fig. 3.7. The variables Ω_1, Ω_2, Ω_3 and Ω_4 denote the sub-layer soil, the top layer soil, the backfill region, and the seawater domains respectively. The variables Γ_1, Γ_2, Γ_3 and Γ_4 are used to represent the domain boundaries for their respective domains. The geometric parameters defining vertical dimensions of the problem domain are D_1, D_2 and D_4. The horizontal width of the model is denoted as L. The cover depth of pipeline is D_b; the dimension at the lower section of the trench is D_t; the collapsed gap due to backfilling is D_c; the width of the trench at the top is L_{tt}; and the width of the trench on which the pipeline rests is L_{tb}. As for the boundary conditions, T_w is the initial temperature of the seawater domain; T_b is the temperature at the bottom of the sub-layer soil layer; and Q_1, Q_2 and Q_4 are the heat flux specified at the lateral boundaries of the subdomains. The variable d_0 is the outer diameter of the pipeline where either an essential condition (temperature, T_p) or a natural condition (heat flux, Q_p) is specified. The natural convection of seawater was found to be negligible for steady-state heat transfer in deepwater clay when the soil permeability is in the range of 10^{-8}~10^{-7} *m/s*. Additionally,

natural convection effect is also negligible compared to the heat conduction. Consequently, this provides the basis to further assume that the soil can be modeled as a homogeneous isotropic media for each domain using the equivalent thermal conductivity of a saturated soil.

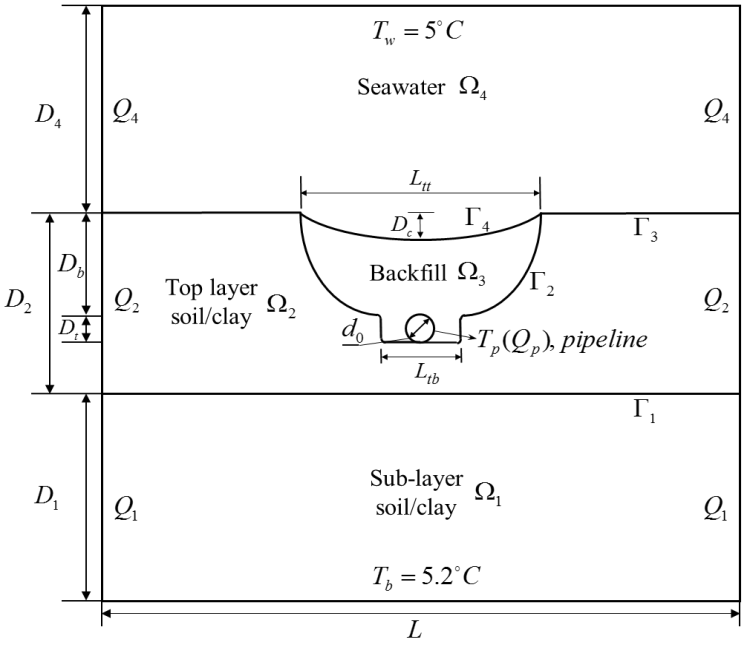

Fig. 3.7 Sketch of 2D pipe-trench model for BEM numerical investigation

The mathematical formulation using BEM follows the numerical procedure elaborated in Chapter 2. However, due to an additional domain resulted from trenching and backfill, the global matrix presented by Eq. (2.29) cannot be directly applied to this specific problem. As a consequence of having multiple domains, i.e. soil and seawater, the formulation must be assembled in a way so that the assembled system of equations are ordered in a manner assuring the continuity of temperatures and heat fluxes on the

interfaces between adjacent domains. To accomplish this, the columns of *H* and *G* matrices for each layer were grouped based upon the external boundary nodes and the interface nodes as follows

$$\begin{bmatrix} H_1^e & H_1^{\Gamma_1} \end{bmatrix} \begin{Bmatrix} T_1^e \\ T_1^{\Gamma_1} \end{Bmatrix} = \begin{bmatrix} G_1^e & G_1^{\Gamma_1} \end{bmatrix} \begin{Bmatrix} q_1^e \\ q_1^{\Gamma_1} \end{Bmatrix} \tag{3.5}$$

$$\begin{bmatrix} H_2^e & H_2^{\Gamma_3} & H_2^{\Gamma_2} & H_2^{\Gamma_1} \end{bmatrix} \begin{Bmatrix} T_2^e \\ T_2^{\Gamma_3} \\ T_2^{\Gamma_2} \\ T_2^{\Gamma_1} \end{Bmatrix} = \begin{bmatrix} G_2^e & G_2^{\Gamma_3} & G_2^{\Gamma_2} & G_2^{\Gamma_1} \end{bmatrix} \begin{Bmatrix} q_2^e \\ q_2^{\Gamma_3} \\ q_2^{\Gamma_2} \\ q_2^{\Gamma_1} \end{Bmatrix} \tag{3.6}$$

$$\begin{bmatrix} H_3^e & H_3^{\Gamma_4} & H_3^{\Gamma_2} \end{bmatrix} \begin{Bmatrix} T_3^e \\ T_3^{\Gamma_4} \\ T_3^{\Gamma_2} \end{Bmatrix} = \begin{bmatrix} G_3^e & G_3^{\Gamma_4} & G_3^{\Gamma_2} \end{bmatrix} \begin{Bmatrix} q_3^e \\ q_3^{\Gamma_4} \\ q_3^{\Gamma_2} \end{Bmatrix} \tag{3.7}$$

$$\begin{bmatrix} H_4^e & H_4^{\Gamma_4} & H_4^{\Gamma_3} \end{bmatrix} \begin{Bmatrix} T_4^e \\ T_4^{\Gamma_4} \\ T_4^{\Gamma_3} \end{Bmatrix} = \begin{bmatrix} G_4^e & G_4^{\Gamma_4} & G_4^{\Gamma_3} \end{bmatrix} \begin{Bmatrix} q_4^e \\ q_4^{\Gamma_4} \\ q_4^{\Gamma_3} \end{Bmatrix} \tag{3.8}$$

where, the subscript *j* means the j^{th} domain, the superscript *e* denotes the external boundary, and the superscript Γ_j represents the node on the j^{th} interface.

The assembly of the global matrix used the same procedure demonstrated in Chapter 2. The steps leading to the final form are fairly straightforward and are summarized here for completeness. The compression, inversion, and reordering of columns of the subdomain matrices are performed according to the order of boundary nodes. The heat flux is continuous at two adjacent elements and is discontinuous at the corners of interfaces and external boundaries. In the process, an extra unknown that exists at the joint node of the interfaces Γ_2, Γ_3 and Γ_4 was addressed in order to obtain a solvable system of linear equations. There are four unknowns at this joint node

including three nodal heat fluxes associated with three boundary elements on the three interfaces and one nodal temperature. The interpolation scheme proposed in Chapter 2 via Eq. (2.30) thru. Eq. (2.34) is adopted to introduce one more relation about the nodal heat fluxes at this joint node.

Then utilizing Eq. (3.5) thru. Eq. (3.8) and performing a series of matrix manipulations lead to the final from of the assembled global matrix equations in the form

$$\begin{bmatrix} H_1^e & & & H_1^{\Gamma_1} & & & \\ & H_2^e & & IH_2^{\Gamma_1} & H_2^{\Gamma_2} & H_2^{\Gamma_3} & \\ & & H_3^e & & IH_3^{\Gamma_2} & & H_3^{\Gamma_4} \\ & & & H_4^e & h_4^{\Gamma_3}\cdots & IH_4^{\Gamma_3} & IH_4^{\Gamma_4} \end{bmatrix}$$

$$\begin{bmatrix} -CG_1^{\Gamma_1} & & & \\ \frac{\kappa_1}{\kappa_2} IG_2^{\Gamma_1} & -CG_2^{\Gamma_2} & -CG_2^{\Gamma_3} & \\ & \frac{\kappa_2}{\kappa_3} IG_3^{\Gamma_2} & & -CG_3^{\Gamma_4} \\ & & \frac{\kappa_2}{\kappa_4} IG_4^{\Gamma_3} & \frac{\kappa_3}{\kappa_4} IG_4^{\Gamma_4} \end{bmatrix} \begin{Bmatrix} T_1^e \\ T_2^e \\ T_3^e \\ T_4^e \\ T_1^{\Gamma_1} \\ T_2^{\Gamma_2} \\ T_2^{\Gamma_3} \\ T_3^{\Gamma_4} \\ cq_1^{\Gamma_1} \\ cq_2^{\Gamma_2} \\ cq_2^{\Gamma_3} \\ cq_3^{\Gamma_4} \end{Bmatrix} = \begin{bmatrix} G_1^e & & & \\ & G_2^e & & \\ & & G_3^e & \\ & & & G_4^e \end{bmatrix} \begin{Bmatrix} q_1^e \\ q_2^e \\ q_3^e \\ q_4^e \end{Bmatrix} \tag{3.9}$$

where, the prefix term '*C*' and '*c*' represent compression of original columns respectively, and '*I*' denotes reordering the columns according to numbering of nodes.

By substituting Eq. (2.32) and boundary conditions into Eq. (3.9), the solution for the thermal field at the boundaries can be achieved. Then the temperatures at internal

points of interest can be evaluated using Eq. (2.5). Note that singularities can cause some numerical issues when evaluating internal points that are close to the nearest boundary element (Yang et al., 2002). It is suggested that in the discretization step, one should be careful to avoid internal points that fall within a half-length radius of the nearest boundary element. This issue can be ameliorated by increasing the mesh density.

The two-dimensional boundary element model was initially depicted in general terms in Fig. 3.7. The model provides for a change of thermal properties in each domain. The specific dimensions and material properties used in this model are presented in Tab. 3.2. The outside diameter of the heat pipeline is also a parameter that will be part of the parametric study. The thermal conductivity ratio for the backfill is estimated with reference to the thermal conductivity of the topsoil layer. Since the thermal conductivity varies with the consolidating process of the backfill soil, this ratio will also be discussed in the parametric study.

Table 3.2 Primary dimensions and thermal properties of the BEM model

	Name	Symbol	Value	Unit
Dimension	Thickness of the sub-layer soil	D_1	8.0	*m*
	Thickness of the top-layer clay	D_2	2.8	*m*
	Thickness of the seawater	D_4	8.0	*m*
	Bottom depth of trench	D_t	0.4	*m*
	Width of the truncated model	L	20	*m*
	Top width of the backfill region	L_{tt}	3.6	*m*
	Bottom width of the backfill region	L_{tb}	1.2	*m*
	Outside diameter of pipeline	d	0.4	*m*
Thermal conductivity	Sub-layer thermal conductivity	κ_1	1.2	*W/m K*
	Top-layer thermal conductivity	κ_2	1.0	*W/m K*
	Thermal conductivity of seawater	κ_4	0.65	*W/m K*

A sense of the problem symmetry and the boundary element discretization for the illustrative example is shown in Fig. 3.8, and some of the realistic problem values are noted. The lateral temperature gradients of the two soil layers and the seawater layer are specified as being zero, and this approximates the boundary conditions in the far field in the horizontal direction. A constant temperature of 5.2℃ accounting for geothermal gradient is adopted at the lower bound of the sub-layer soil. Due to the forced convection of bottom currents near the seabed, the temperature of the seabed is assumed to be constant by some researchers (Lu et al. 2008, Xu et al. 2010, and Barletta et al. 2008). However, it has been reported that in the North Sea in shallow water where seafloor current is present, heat dissipated from buried cables still imposes a significant impact on the local submarine ecology system (Kogan, 2003). If the constant temperature on the seabed were used, it is prescribed by assuming that there is not any thermal impact from the buried cable or pipeline, which is not true in reality. Even when seafloor current is present, the local thermal impact still exists.

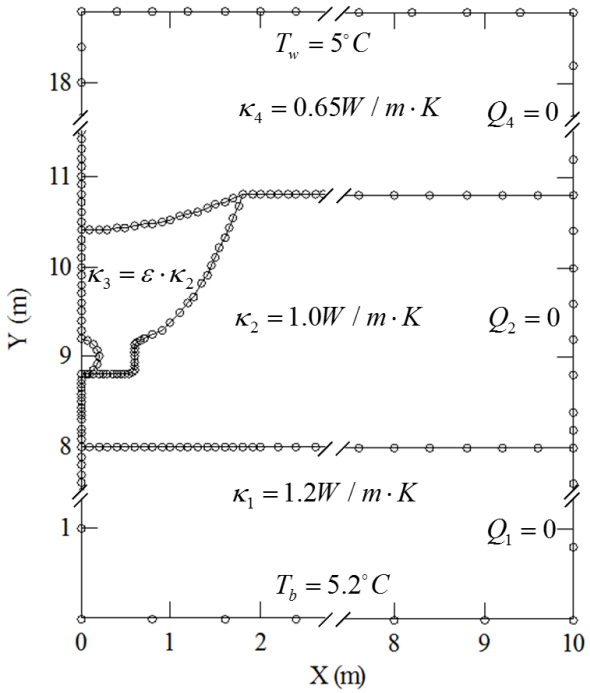

Fig. 3.8 BEM mesh of the pipe-trench model

In this numerical investigation, a visual view of the thermal field on the seafloor and the local thermal impact can be evaluated using the BEM model developed in this study. Considering the low seawater temperature in deep water, a constant seawater temperature of 5℃ is assumed at the upper bound of the seawater far away from the seabed. This approach is conservative since the temperature gradient on the seafloor induces the natural convection of seawater near the seabed. Finally, regarding the complexity of the multi-phase flow inside transporting pipes, a uniform heat flux dissipated from the pipe is used for the parametric study.

3.3 Parametric Study of Thermal Field around a Buried Pipeline

The model allows for one to account for the complex geometries in the near field associated with site-specific multi-layered soil conditions, the seawater adjacent to the seafloor, and the burial technique demonstrated previously. The numerical examples illustrate 1) the influence of the backfill thermal property on the temperature at the pipe wall, 2) the correlation of the pipe diameter and the required output thermal power needed to maintain the desired pipe wall temperature, and 3) the burial depth's influence on the seabed temperature distribution above the pipeline.

3.3.1 The thermal insulation efficiency of different materials

The deepwater buried pipelines transport mixtures of oil and gas, and their associated impurities. These impurities are sensitive to temperature and pressure, and are consequently deposited and accumulate under different conditions. For example wax typically becomes an issue at around 30~50℃, and hydrates form around 20℃ at 10 *MPa* (Su, et al., 2003). Under the normal operational conditions the temperature of hydrocarbons being transported has to stay above 55℃ (Osborne et al., 2001). To examine the thermal power required to maintain this wall temperature, the following parameters were selected: outer pipe diameter of 0.4 m, the initial cover depth of 1.6 m, and a conductivity ratio of 0.9. The minimum required heat flux, 55 W/m^2, was screened out for the pipes without insulation treatment. Fig. 3.9 shows the temperature distribution in the surrounding soil. The white space seen in Fig. 3.9 illustrates null value regions where temperature is not evaluated in order to avoid numerical singularity

issues. Refining the boundary mesh can minimize this numerical issue.

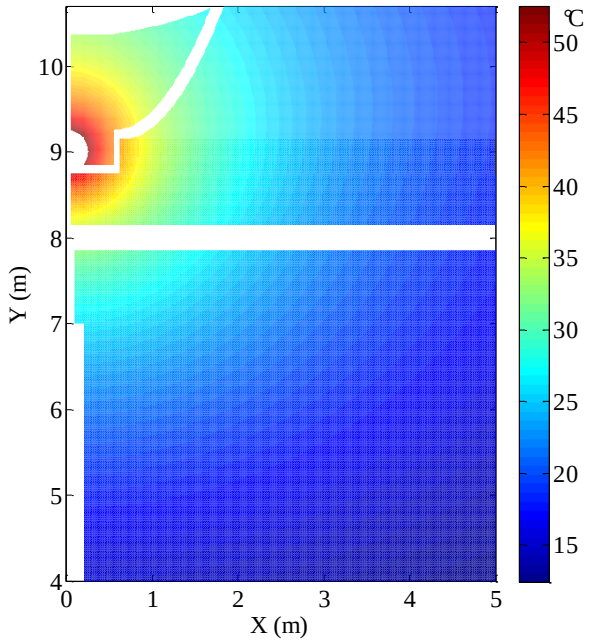

Fig. 3.9 Temperature in clay around the pipeline with heat flux of 55 W/m^2

Fig. 3.10 shows the temperature distribution along the external surface of pipeline in terms of uniform heat flux. Since the fluctuation of temperature at the external side of the pipe is relatively small, the uniform heat flux is approximately equivalent to the uniform temperature at the external boundary of the pipe. However, variance of the temperature distribution slightly increases with the output heat flux. A linear fit between the mean temperature and heat flux for this specific example is obtained and plotted in Fig. 3.11 with the inclusion of temperature variance

$$\overline{T}_{ext} = 0.894Q + 5.13 \tag{3.10}$$

where, $\overline{T}_{ext}$ is the average temperature (℃) and Q (W/m^2) is the output heat flux.

Neglecting the thermal resistance of the steel pipe wall, the approximate inner wall temperature can be obtained by the following expression

$$T_{wall} = \overline{T}_{ext} + Q \cdot t / \kappa_{in} \tag{3.11}$$

where, t is the thickness and κ_{in} is the thermal conductivity of thermal insulation layer.

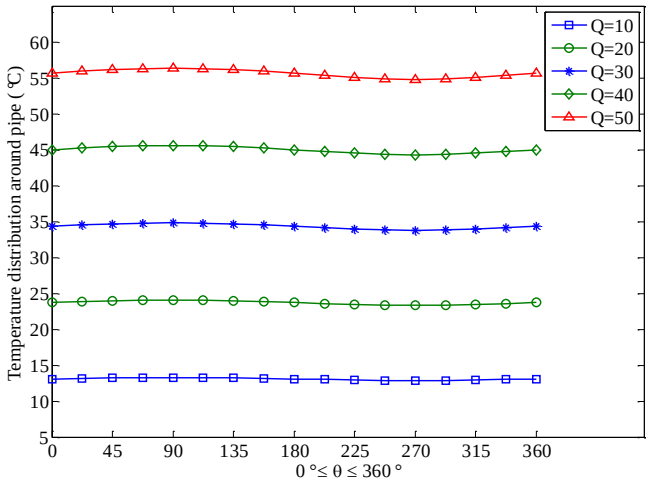

Fig. 3.10 Temperature along the circumferential surface of external pipe wall

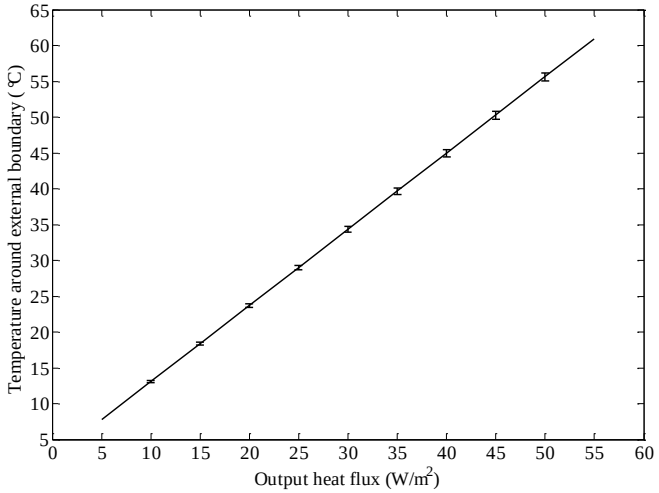

Fig. 3.11 Linear fit of external mean temperature and heat flux

The thermal power loss is the product of the output heat flux and the circumference of pipes using the outer diameter. Assuming the insulation layer thickness of 30 *mm*, the thermal power loss needed to maintain different inner wall temperatures is listed in Tab. 3.3 for three typical insulation materials. These results reveal that the pipe-in-pipe (PIP) is much more effective than the integrated external insulation technique in terms of maintaining temperature. However, the PIP is less cost-effective than the integrated coating (Grealish, et al., 2002).

Table 3.3 Insulation efficiency of pipe operated at different temperature

Inner pipe wall temperature (℃)		55	60	65	70	75	80
Thermal power loss (*W/m*)	Without insulation	70.10	77.13	84.16	91.18	98.21	105.24
	Soild polypropylene ($0.22 W/m \cdot K$)	60.82	66.92	73.02	79.12	85.21	91.31
	polypropylene foam ($0.15 W/m \cdot K$)	57.28	63.03	68.77	74.51	80.26	86.00
	PIP polyurethane ($0.025 W/m \cdot K$)	29.93	32.93	35.93	38.93	41.93	44.93
Insulation efficiency (%)	Soild polypropylene			13.23%			
	polypropylene foam			18.28%			
	PIP polyurethane			57.31%			

Note: thermal conductivity of insulation material refers to Grealish et al. (2002).

3.3.2 Influences of thermal conductivity of backfill soil

Since moisture and void ratio can change the thermal conductivity of soil and the thermal conductivity of backfill changes during the consolidation process (Newson, et al., 2002), the influence of the conductivity ratio between the backfill soil and the undisturbed top layer is studied next. Consider the pipe-trench model with the outer pipe

diameter of 0.4 *m* without thermal insulation and the initial cover depth of 1.6 *m*. Under the thermal power loss of 80 *W/m*, the temperature along the circumferential outer surface of the pipeline is presented in Fig. 3.12. The right horizontal point and the upper top point of the pipeline correspond to 0 ° and 90 ° respectively. Fig. 3.12 includes two extreme cases of the thermal conductivity of backfill soil. The ratio of 0.65 indicates that the trench is filled with seawater. The ratio of 1.0 denotes the situation where the thermal conductivity difference between backfill and the undisturbed soil is neglected. It can be seen that the maximum temperature difference occurs when the pipe is placed in the trench without coverage. However, the natural convection of seawater driven by buoyancy force due to temperature gradients may reduce the temperature difference. But, it is observed that backfill reduces temperature difference between the upper surface and the lower surface of a pipeline, which can reduce the upheaval risk due to thermal expansion.

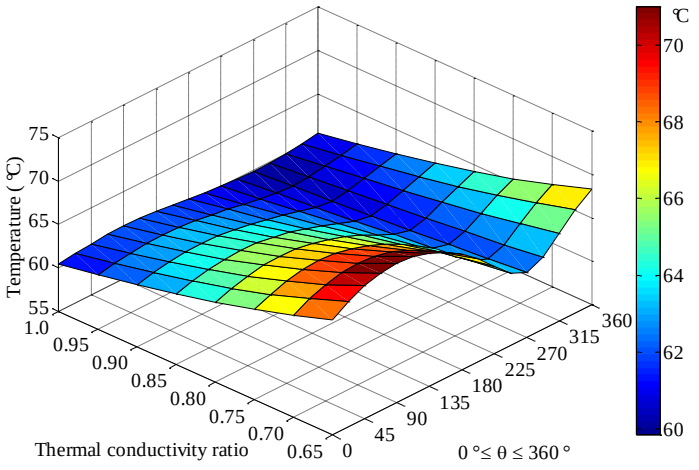

Fig. 3.12 Temperature along the circumferential external surface of the pipeline

Fig. 3.13 and Fig. 3.14 show temperature distributions on the seabed and under the pipeline in the vertical direction. The horizontal distance away from the centerline of the pipeline is normalized by the pipeline's outer diameter. A seabed temperature slightly higher than 30 ℃ is observed on the seabed directly above the pipeline, and this may be reduced if the seawater convection effect is included.

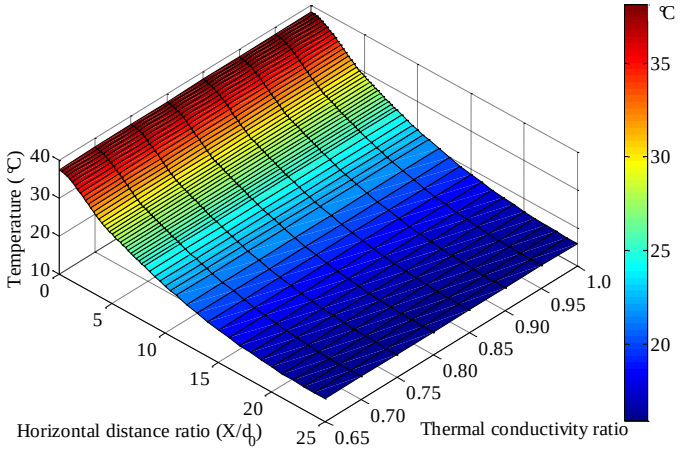

Fig. 3.13 Temperature distributions on the seabed vs. thermal conductivity ratio

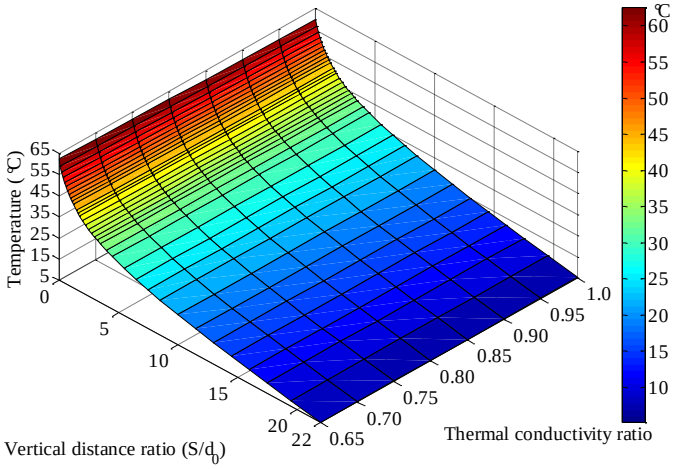

Fig. 3.14 Temperature distribution under the pipe

To evaluate the influence of the conductivity variation on the external pipe wall and on the seabed temperature, Fig. 3.15 is presented with a temperature ratio normalized by the corresponding temperature for a conductivity ratio of 1. It can be noted that neglecting trenching and backfill effects may underestimate the temperature difference between the upper and the lower part of the pipeline. Backfill can reduce this temperature difference. The temperature difference is small when the pipeline exterior is maintained at an average of 55 $^{\circ}C$. However, this difference grows when the average temperature increases and may aggravate the thermal buckling issue due to thermal expansion. Even though the significance of the temperature gradient is small compared to the imperfection of welded joint along pipelines and unevenness of the seafloor or burial trench for thermal buckling. The significance should be quantitatively investigated by either model test or numerical simulation. The average temperature may control the upheaval buckling. However, the small bending initiated by the small temperature difference between the upper surface and the lower surface of the pipeline is important. It is worth considering this effect in the thermal buckling analysis when checking the structural stability of subsea pipeline, where failure may result in catastrophic impact to the ocean environment. Thus, it is worth considering the installation effect in the thermal buckling analysis when checking the structural stability of a subsea heat pipeline.

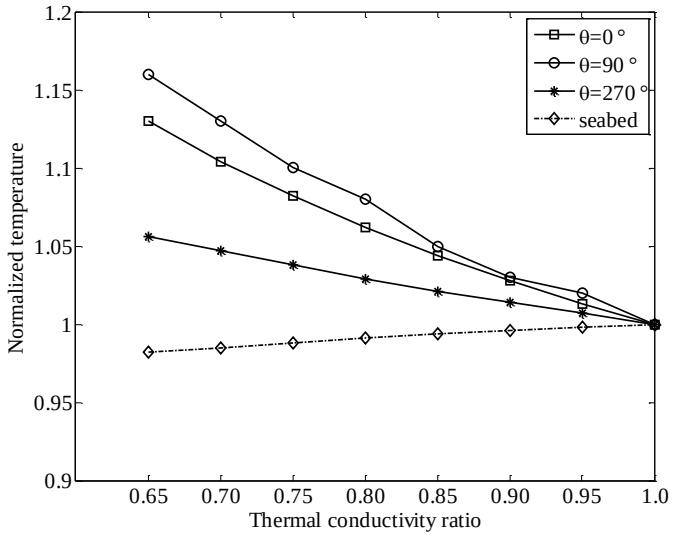

Fig. 3.15 Normalized temperature versus the thermal conductivity ratio

From Fig. 3.13 thru. Fig. 3.15, it can be also concluded that the thermal conductivity variation of backfilling has only a local impact and a limited influence on the temperature distributions on the seabed. At the seabed directly above the pipe, the variation is less than 3%.

3.3.3 Influences of the cover depth

Since thermal properties of backfilling impact the fluctuation of temperatures on the external surface as discussed above, the effect of backfilling on temperature distributions is further investigated with respect to the cover depth. Fig. 3.16 shows the local pipe-trench model with different cover depths. The cover ratio is defined as D_b / d_0. The following parameters were employed in this numerical investigation: the pipeline's outer diameter was of 0.4 *m*, the output thermal power was 80 *W/m*, and the

ratio of 0.9 was selected reflecting the consolidation process of the backfill clay.

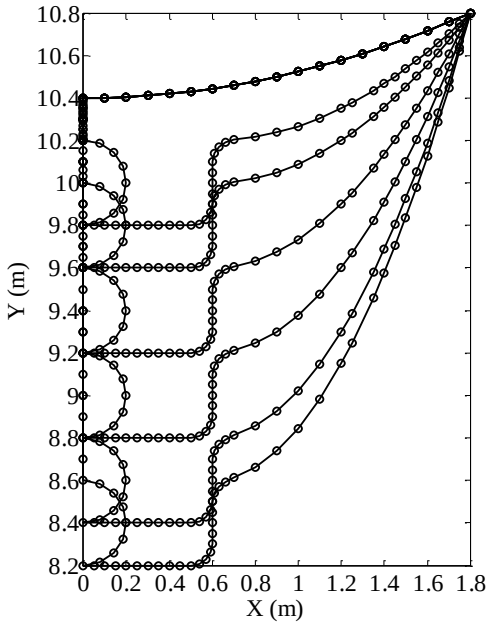

Fig. 3.16 BEM mesh of the trench and pipe showing different actual burial depth

Under various cover depth conditions, the temperature distribution along the circumferential surface of the pipeline is shown in Fig. 3.17. It demonstrates that deeper cover depth does not significantly reduce the temperature difference on the external surface of the pipeline. The minimum temperature difference case corresponding to a cover depth ratio of 4 was determined for this model. However, in the range of 5 pipeline diameters, temperatures on the seabed decreased dramatically with the increase of the cover depth as shown in Fig. 3.18. To examine the influence of cover depth on temperature of seabed and along the external surface of the pipeline, the temperatures in the 1.5 diameter cover depth case are normalized temperatures at specific points. Fig.

3.19 shows that the cover depth has a greater impact on the seabed than the external surface of the pipeline. The three points along the circumferential surface of the pipeline are defined in a polar coordinate where 0˚ starts from the horizontal plane. Thus, 0˚, 90˚ and 270˚ denotes the middle point, the top point, and the bottom point respectively.

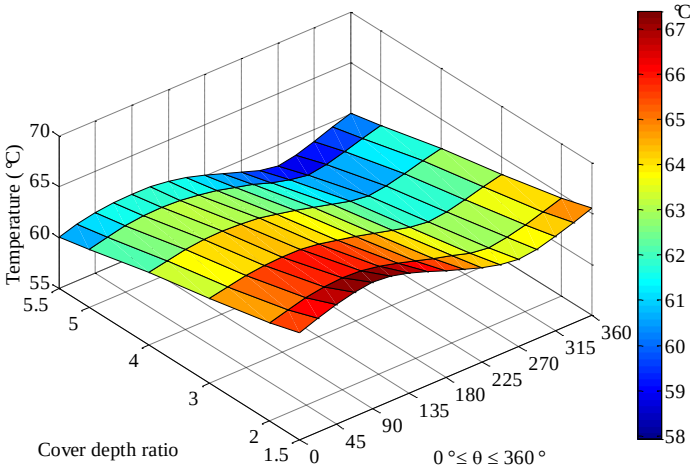

Fig. 3.17 Temperature on the external pipeline surface versus initial cover depth ratios

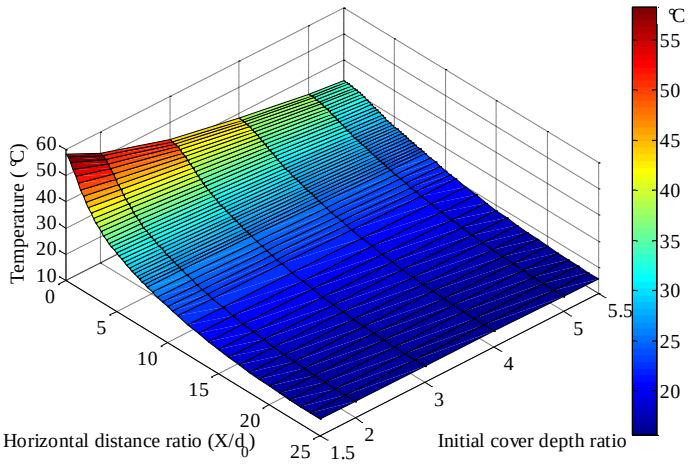

Fig. 3.18 Temperature distribution on the seabed with cover depth variation

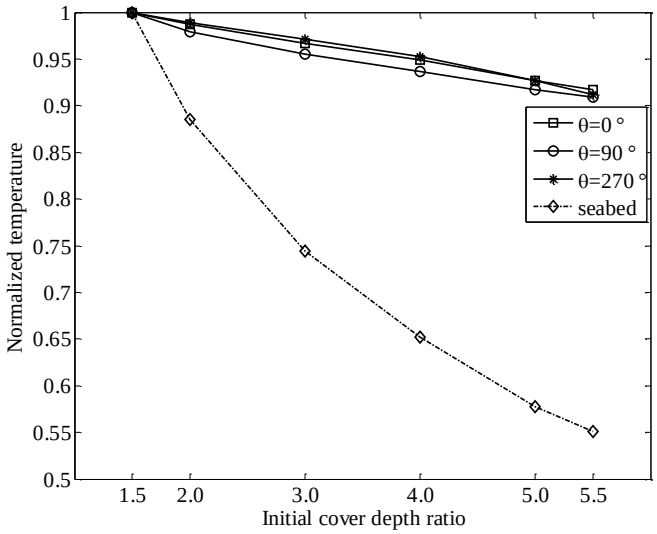

Fig. 3.19 Normalized temperature versus the initial cover depth

For the cover depth ratio of 4, the temperature on the seabed directly above the pipeline dropped by 35% compared to that of the cover depth ratio of 1.5. While the temperature-drop along the external surface of the pipeline at the three typical points is less than 10%. However, convection effect in the seawater may reduce the temperature directly above the pipeline. In fact, the maximum temperature along the surface of the pipeline depends on the thermal conductivity ratio and the relative relation between the thermal conductivity of the top layer and the mother soil, which determines the quick heat dissipation path. It was found that deeper coverage does not significantly reduce the temperature difference of the external boundary of the pipeline. However, deeper coverage can greatly reduce the thermal impact on the seabed above the buried pipeline.

3.3.4 Effect of pipe diameter

Depending on the capability of the trenching equipment, the depth of the trench

may vary. For this study it was assumed to be 2 *m*. The thermal conductivity ratio was selected as 0.9. Fig. 3.20 shows the BEM mesh on the local pipe-trench model with various diameters.

Under the same thermal power loss of 80 *W/m*, temperature distributions along the external circumferential surface for a number of pipelines with different outer diameters are shown in Fig. 3.21. The numerical simulation reveals two important results. First, the temperature fluctuation on the pipe wall is small. Second, if the same wall temperature is to be maintained for different pipes, the required output thermal power increases with the pipe diameter.

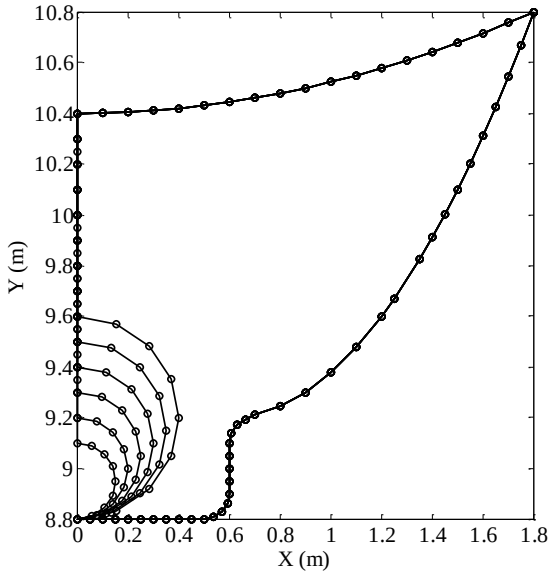

Fig. 3.20 Detail of pipe-trench with different size of pipes

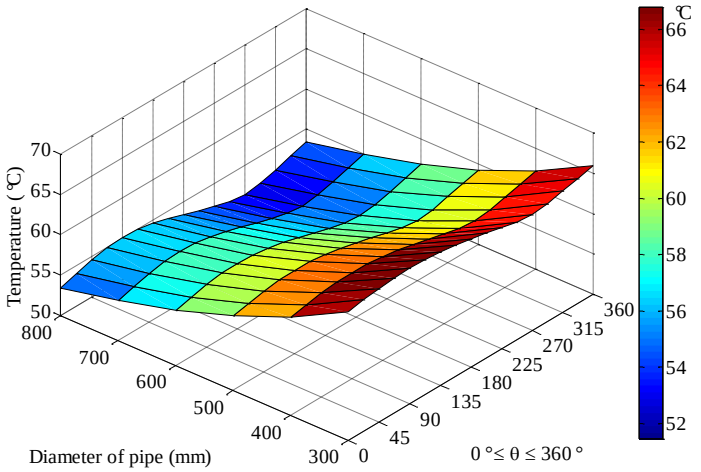

Fig. 3.21 Temperature along the external pipeline surface versus outside diameter

To examine how deep the heat can penetrate into the soil, Fig. 3.22 shows temperature distributions directly beneath the pipe. These results demonstrate that the size of pipes only significantly impacts the local temperature field within the range of only a few pipeline diameters. Further, it only slightly influences the far field, seven meters below the pipelines, where the temperature increased less than 5 ℃. This local impact comes from the distance to the center of heat source and geometry configuration of the pipe-trench system due to the variation of pipe diameters.

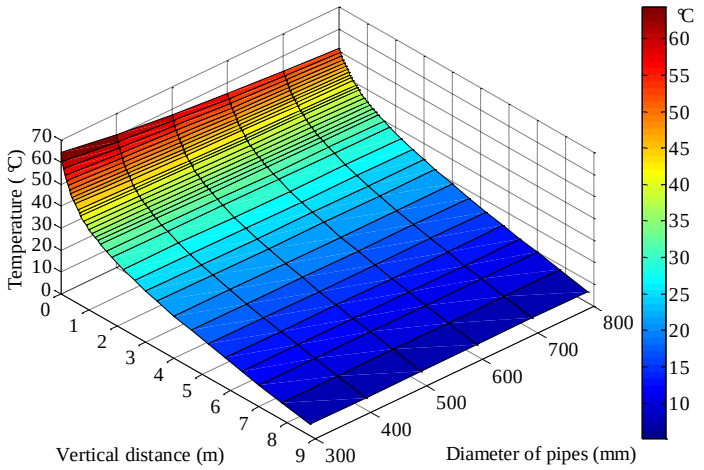

Fig. 3.22 Temperature distribution in soil beneath the pipe versus pipeline diameter

A numerical simulation was performed using CB to investigate the transit heat transfer of a pipeline in both a solid and porous medium. The objective is to determine the conditions one could pursue the analysis of this complex system assuming steady-state heat transfer within the thermal field of interest. Heating or cooling down of the exterior pipeline wall temperature was observed to drive the natural convection process in the soil for both the solid and porous medium cases. For these two cases, the time required to reach essentially identical steady-state conditions differed by days. Based upon these numerical simulations the effects of the natural convection cannot be neglected for soils having much larger hydraulic permeability than the deep sea marine clay examined in this study. Furthermore, even though the induced liquid flow in clay presents a significant impact on the transient heat transfer analysis, it doesn't significantly affect the steady-state thermal distribution in the domain of interest since it is assumed that a steady-flow through the pipeline has been established longer than the

observed two-month period.

The thermal field encompassing the deep sea buried pipeline was efficiently modeled using the boundary element method. The proposed multi-layer model addressed the complex geometries of trenching and backfill effects, as well as, taking advantage of the problem symmetry. A comparison of FEM and BEM values at nodal points showed a difference much less than one-half a percent for solid media case. Linear correlation between the uniform heat flux and the mean internal pipe wall temperature can be obtained using this pipe-trench model and BEM based approach. Burial depth poses a significant impact on thermal field on the seabed but a limited influence on the temperature variation along the circumferential pipe wall. Both trenching and backfill effects should not be neglected, since the thermal conductivity of backfill clay can significantly impact the thermal field along the external pipe wall. Finally, the BEM model as discussed can be extended to address the preliminary thermal insulation design of heated pipeline.

4. MESHFREE FORMULATION OF SUBSEA CABLES

Fishing and anchoring activities impose potential hazards to the submarine cables and these two causes contribute to around 70% of telecom cable damage in the Atlantic (Worzyk, 2009). Though enlightenment about the interference between fishing gears and cables can be gained from experience of the interaction between gears and pipelines, the response behavior of cables is somewhat different because of both structural specifications and boundary conditions including displacement and force boundary conditions. Regarding the bending stiffness, a cable is much more flexible than a pipeline. Subsequently it results in different seabed layout configurations for the exposed pipelines and cables. Even though a cable route is planned to avoid exposure in places where fishing activity is massive, free spanning is inevitable in rocky areas and in the places where a bottom current induces aggressive sediment transport on the seabed and creates sand waves as illustrated in Fig. 4.1. The interaction process between gears and cables is elaborated first and subsequently a mathematical description of slender rod is selected for physical investigation.

From the point of view of structural integrity, DNV (2010) released the recommended practice guidance on the interference of trawl gears and pipelines, which provides insight on the structural evaluation of pipelines in case of accidental loads from trawl gears such as clump weights, trawl boards and beams.

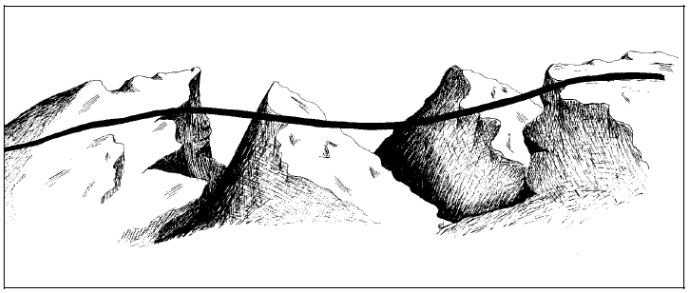

(a) A free cable span between rocks

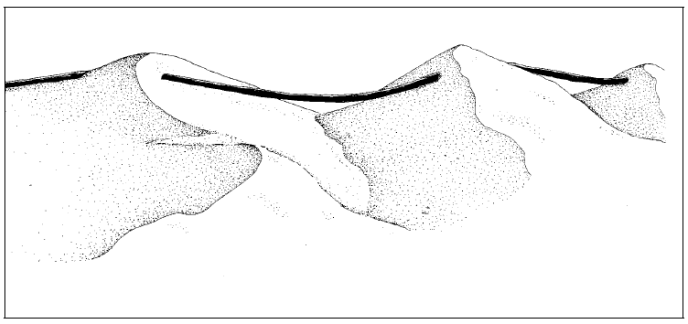

(b) A free cable span between sand waves

Fig. 4.1 Two scenarios of free spans of subsea cables (Drew, 2010)

The interference mechanism between a cable and a trawl gear resembles somewhat that of a pipeline and a gear: (1) The initial collision is the instantaneous impact when a trawl gear hits the cable. Fig. 4.2(a) shows the initial impact case. Since the cable behaves like a slender rod during this interaction and the towing speed of the gear is slow, the damage to the cable may not be significant in this scenario and is not of interest in this study; (2) The pull-hooking phase is the stage following the short impact under which the trawl equipment is dragged over the cable. Fig. 4.2(b) demonstrates a trawl board pulls a cable stuck between rocks or sand waves. Due to the massive weight of a typical industry trawl board (2-9 tons) and clump weight (9-10 tons), the maximum pulling force (200 kN) may exceed the break load or cause evident damage to the

submarine cables. Hooking may happen during the pulling phase and is termed as pull-hooking for clarity and should be investigated considering structural integrity of cables; and (3) Direct hooking describes the case where the cable is entangled with gears. Fig. 4.2(c) shows a cable is being towed by a board and is hooked by rocks or sand waves as shown in Fig. 4.2(d). It is a rare situation for pipelines but may be a common situation for cables as the much smaller relative dimension of a cable to a gear than that of a pipe to a gear. This case involving movable boundary conditions and displacement-dependent loading is the other interest of this study.

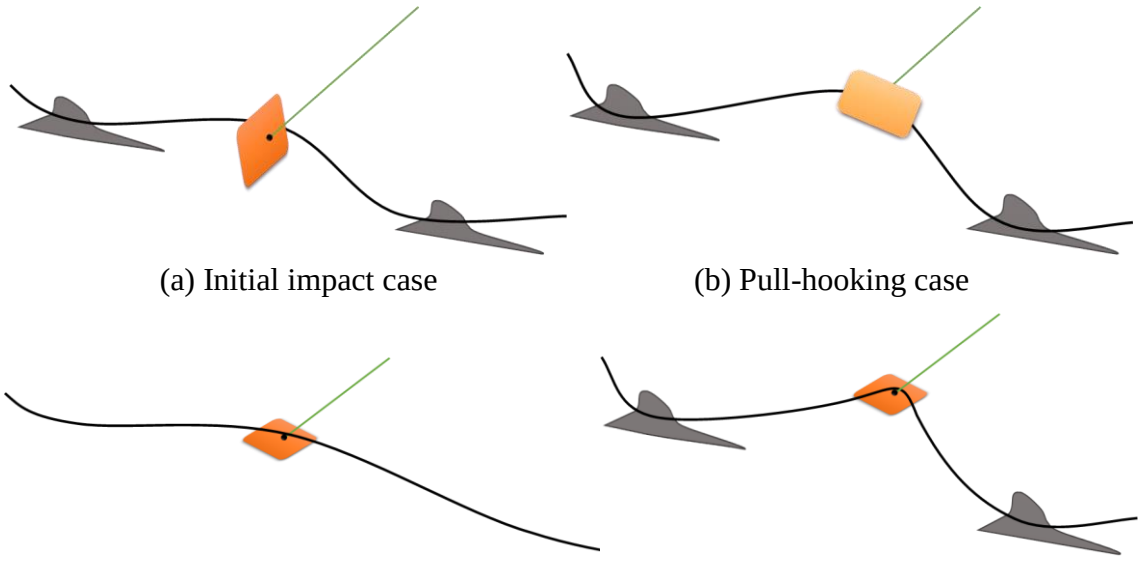

(a) Initial impact case (b) Pull-hooking case

(c) Direct hooking case (d) Cable hooked in direct hooking case

Fig. 4.2 Sketch of the interaction phases between trawl board and cable

Since the interaction scenarios are stated, arbitrary layout configuration, moving boundaries, drag force due to partial burial on the seafloor, and strong nonlinearity due

to large deflection of cables are the challenging issues that need to be handled properly. Assumptions are made so as to propose a reasonable model which can handle these aforementioned issues. According to the layout of cables on the seabed (Drew, 2009) and exposed spans illustrated in Fig. 4.1, the curvilinear coordinate shown in Fig. 4.3 is well suited to represent the center line of a deformable cable in 3-D space and to benefit the derivation of governing equations. The position vector $\vec{r}$ is a function of the arc-length s. Since the cable is extensible, elongation due to axial tension will be included. This mathematical description was adopted by earlier studies, see for example Nordgren (1974), Garrett (1982), Ma and Webster (1994) and Chen and Zhang (2001).

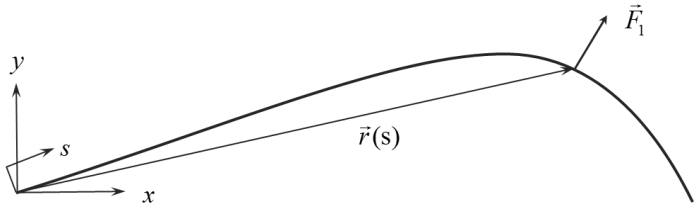

Fig. 4.3 Illustration of curve coordinate for the interaction model

The slender rod theory is to be reviewed to establish the governing equations for the cable problem. The state art of meshfree methods on solid mechanics applications is to be critically reviewed intended to filter out a candidate meshfree method considering all numerical implementation facets such as field value approximation, weak formulation, discretization, and numerical integration of point stiffness. Local radial point interpolation method (LRPIM) is further formulated to apply to the cable problem and associated numerical issues will be investigated subsequently such as node

distribution, shape parameters, and numerical convergence by two benchmark examples.

4.1 Review of Slender Rod Theory and Meshfree Method

The study assumes uniform bending stiffness, no shear deformation and no rotational inertia. In order to derive the equation of motion of a slender cable, the cable is assumed inextensible first and thus the deformed and undeformed states coincide. The instantaneous configuration of a cable is described by $\vec{r}(s,t)$ as shown in Fig. 4.4.

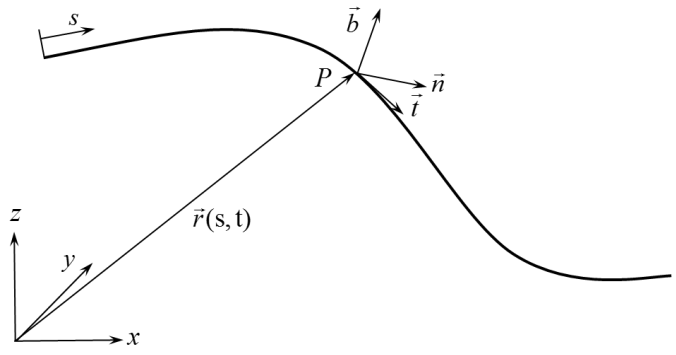

Fig. 4.4 Coordinates for mathematical formulation

In Fig. 4.4, the unit tangent vector, the unit normal vector, and the unit binormal vector are denoted as $\vec{t}$, $\vec{n}$ and $\vec{b}$. Some basis in the differential geometry of curves including the Serret Frenet formulae are utilized and then the unit normals are defined as

$$\vec{t} = \vec{r}', \ \vec{n} = \vec{r}'' / \kappa, \ \vec{b} = \vec{t} \times \vec{n} \tag{3.12}$$

where, prime denotes the derivative with respect to s and κ is the curvature defined by

an identity $\kappa^2 = \vec{r}'' \cdot \vec{r}'' = -\vec{r}' \cdot \vec{r}'''$.

Fig. 4.5 illustrates a differential element on the cable. According to the conservation of linear and angular momentum, the equations of motion are expressed as

$$\vec{F} + \vec{q} = \rho \ddot{\vec{r}} \tag{3.13}$$

$$\vec{M}' + \vec{t} \times \vec{F} + \vec{m} = 0 \tag{3.14}$$

where, ρ is the mass per unit length, $\vec{q}$ and $\vec{m}$ are the distributed force and moment along the cable per unit length respectively, and $\vec{F}$ and $\vec{M}$ are internal force and moment of the cross section. Double dot means the second derivative with respect to time.

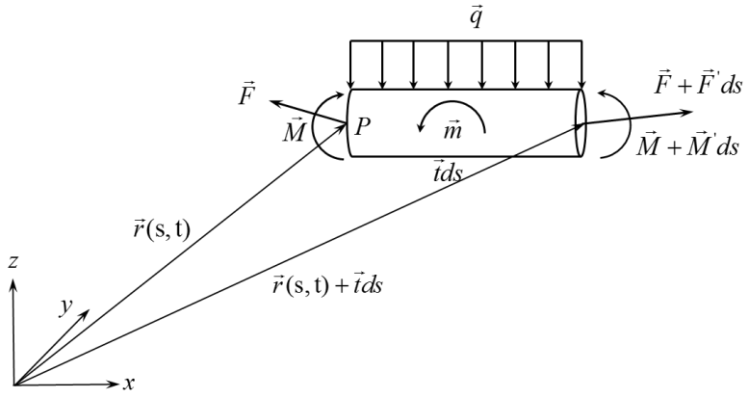

Fig. 4.5 A differential element on a cable

Though a small deformation is presumed, it still allows large deflection of the cable due to small rotational angle caused by bending and rigid body motion. Therefore, Bernoulli-Euler beam theory is still applicable for the constitutive law adopted here,

where the bending moment and torque are proportional to curvature and twisting angle per unit length, respectively.

$$\vec{M} = EI\kappa\vec{b} + H\vec{t} = \vec{r}' \times \left(EI\vec{r}''\right) + H\vec{r}' \tag{3.15}$$

$$\vec{M}' = \vec{r}' \times \left(EI\vec{r}''\right)' + H'\vec{r}' + H\vec{r}'' \tag{3.16}$$

where, EI is the bending stiffness, $H = C\alpha$ is torque, C is the torsional rigidity, and α is the angle of twist per unit length. By substituting Eq. (4.5) into Eq. (4.2), one obtains

$$\vec{r}' \times (EI\vec{r}'')' + H'\vec{r}' + H\vec{r}'' + \vec{r}' \times \vec{F} + \vec{m} = 0 \tag{3.17}$$

Cross product of both sides of Eq. (4.6) by $\vec{r}'$ yields the expression of $\vec{F}$

$$\vec{F} = \lambda\vec{r}' - \left(EI\vec{r}''\right)' \tag{3.18}$$

Substituting Eq. (4.7) into Eq. (4.1) leads to the equilibrium equation

$$-EI\vec{r}'''' + (\lambda\vec{r}')' + q(\mathrm{s}) = \rho\ddot{\vec{r}} \tag{3.19}$$

where, $\lambda = T - EI\kappa^2$ is the Lagrange multiplier.

Then, a small elongation is introduced to the constraint condition

$$\vec{r}' \cdot \vec{r}' = (1+\varepsilon)^2 = \left(1 + \frac{\lambda + EI\kappa^2}{EA}\right)^2 \tag{3.20}$$

where, $\varepsilon = T / EA$ is the normal strain, $T = \lambda + EI\kappa^2$ is the local tension, and A is the equivalent section area of cable.

After the two primary parameters $\vec{r}$ and λ are determined by Eq. (4.8) and Eq. (4.9) together with proper initial conditions and boundary conditions, the internal resultant force and moment can be achieved as follows

$$\vec{F} = \lambda \vec{r}' - (EI\vec{r}'')' \tag{3.21}$$

$$\vec{M} = \vec{r}' \times (EI\vec{r}'') \tag{3.22}$$

The governing equations are well established and to be numerically solved by a meshfree method. Meshfree methods, which don't rely on mesh grid, are successfully applied to elasticity problems with arbitrary geometry of plates, moving boundary conditions, and strong nonlinearity due to large deflection (Atluri, 2004, Chen et al., 1996, Chen et al., 1997, Liew et al., 2002, Han et al., 2005). Pertinent literatures on meshfree methods of structural mechanics, especially about specific approaches applicable to beam-like structures, are critically reviewed so as to screen out the most feasible shape function construction schemes and weak formulation approaches for the subsequent formulation of the interaction between trawl gears and partially buried cables. Various meshfree methods have been developed and successfully demonstrated their capabilities on structural analysis of conventional structures in the past decade, e.g. beam, plate, and shell. Categorization of these studies on solid mechanics helps one figure out feasible technical route of the cable problem. Basically, there are two ways to classify meshfree methods: discretization of governing equations and field value approximation. Strong and weak formulation are the two major ways to transforming a PDE in to a series of linear algebraic equations. Furthermore, weak formulation comprises of the global and local weak formulations. More variants of shape function construction schemes are summarized, which are practical to structural analyses such as static, vibration, and buckling.

Based upon the strong-form, meshfree collocation methods combining moving

least square (MLS) and radial base functions (RBF) were employed by Zhang et al. (2000) and Zhang et al. (2001) respectively and were validated against a cantilever beam. MLS and RBF are adopted to construct the shape functions for the field value approximation. Besides the series representation, smooth particle hydrodynamics (SPH) (Chen et al., 1999), hp-clouds method (Duarte and Oden, 1996), and the reproducing kernel particle method (RKPM) (Chen et al., 1996) use integral form of kernel interpolation schemes for field value approximations, which are also strong-form based methods. However, SPH and hp-cloud are less employed for structural analysis. Mendonca et al. (2000) studies the sensitivities of weight functions, enrichment function and cloud overlapping via a shear deformation beam. Li et al. (2004) developed a Hermite-type cloud method to fluid-structure interaction between sea bottom current and a pipeline, where the pipe was simplified into a two-dimensional plate and the problem was simplified into a plane stress problem. In contrast, RKPM is widely utilized for beam, plate and shell structures, especially for nonlinear problem due to large deformation (Chen et al, 1996, Chen, et al., 1997, Donning and Liu, 1998, Liew et al., 2002).

The other group of meshfree methods is based on weak formulation, either the global weak-form or the local Petrov-Galerkin weak-form. The basis functions used for weight function and the weighted domain differentiate the global and the local form. Joint with Galerkin global weak-form, element-free Galerkin (EFG) method (Belytschko et al., 1994), point interpolation method (PIM) (Liu and Gu, 1999), and radial point interpolation method (RPIM) (Wang and Liu, 2002) have been proposed and applied to

the computational solid mechanics. As for the meshfree methods adopting global weak-form, background cell is essential for numerical integrations of the point stiffness matrix. While the methods based on the local weak-form introduce a local integration domain associated with nodes, these methods that avoid the use of background cells are true mesh free methods. Using the local weak-form, Atluri et al. (1999) proposed the meshless local Petrov-Galerkin (MLPG) method and applied to an Euler-Bernoulli beam, which adopted the MLS scheme for deflection approximation. Later, Cho and Atluri (2001) applied this new meshless method to investigate the possibility of this approach on a shear deformable beam, which demonstrated the potential of MLPG on large deflection problems. Gu and Liu (2001) combined PIM and the idea of MLPG and then proposed a local point interpolation method (LPIM) to study the response of a thin beam under static and dynamic load. Subsequently, Liu and Gu (2001) collaborated the RPIM interpolation scheme and a local weak formulation to the dynamics of a cantilever beam simplified as a 2-D plate. Additionally, Liu and Gu (2005) and Liu (2010), studied the effects of shape parameters of RPIM and recommended the optimal parameters based on their comparative numerical studies of the most four common radial basis function families.

The meshfree method has its own advantage and disadvantage based on either the global or local weak formulation. According to two research groups' work (Atluri 2004 and Liu and Gu, 2005), numerical performances of RPIM, LRPIM and MLPG using weighted least squares are briefly summarized here. The convergent rate and efficiency of RPIM and MLPG is better than LRPIM. However, RPIM based on the

global weak form requires background cell and compatibility of shape functions for point stiffness in the whole domain. In contrast, LRPIM and MLPG are true meshfree methods and don't require compatible shape functions over the whole domain.

Four most often used RBFs are listed in Tab. 4.1 see for reference (Liu, 2002). Franke (1982) numerically compared 29 data interpolation algorithms with respect to parameter sensitivity, complexity of implementation, accuracy and visual quality of fitted surface. This comparative study rated Hardy's multi-quadric (MQ) (Hardy, 1971) approach as one scheme of best performance. Later, Schaback (1995) found the trade-off of error and condition numbers for radial basis function interpolation. Wang and Liu (2002) preliminarily studied the optimal selection of shape parameters of modified MQ-RBF and EXP-RBF and provided reasonable range of these parameters for in the implementation of the RPIM to two-dimensional plane stress problems.

Table 4.1 Four typical RBFs

No.	Name	Expression	Shape parameters
1	MQ	$R_j(\vec{x}) = (d_j^2 + C^2)^q$	C, q
2	Gaussian (EXP)	$R_j(\vec{x}) = \exp(-cd_j^2)$	c
3	TPS	$R_j(\vec{x}) = d_j^\eta$	η
4	Logarithmic RBF	$R_j(\vec{x}) = d_j^\eta \log d_j$	η

With the intent to reduce the requirement on the order of continuity of field interpolation function, the weighted residual statement is often combined with integration by part technique. In respect of weak formulation applied to the cable

problem, the global Galerkin weak form is not applicable when integration by part is used because of the shape function is locally supported. Considering the trade-off of numerical implementation, convergence, symmetry of global matrix, and accuracy, LRPIM is screened out as one qualified candidate meshfree method to further formulate to solve the 4^{th} order differential equations presented in Eq. (4.8) and (4.9). Three variables position vector, tangent vector, and the Lagrange multiplier exist at each node in the meshfree formulation.

In addition, meshfree formulation for cable problems, Cable_3D (Chen, 2002), and commercial FEM programs for beam structures are briefly summarized regarding major numerical implementation issues in Tab. 4.2. Cable_3D differentiates itself from commercial beam FEM programs in respect of the field values interpolated in an element due to different primary variables.

Table 4.2 Comparison of Meshfree, Cable_3D and commercial programs

Item	Meshfree (Cable)	FEM (Cable3D)	FEM beam (ABAQUS, ANSYS)
Field values	position, tangent, stiffness, distributed load and mass	position, tangent, stiffness, distributed load and mass	deflection, rotation angle, distributed mass, material
Shape function	local constructed, different for all local support domains	local constructed, the same for all elements	local constructed, may use different elements
weak formulation	global form, local form	local form	local form
Numerical integration of stiffness	node based, cell based	element based	element based

So far no meshfree method has been applied to the slender rod structures such as mooring line and subsea cables adopting the slender rod formulation. Thus, a further formulation is needed so as to solve Eq. (4.8)-(4.9) and to be extended to cables.

4.2 Meshfree Formulation of the Subsea Cables

Since construction of shape functions is the most critical issue and the very first step when deploy meshfree methods, the most basic requirements on shape functions are summarized in this section (Liu, 2002, Atluri, 2004, and Li and Mulay, 2005).

First, shape functions are linearly independent for all nodes in a local support domain where field values are approximated. Second, the partition of unity condition must be satisfied for all nodes through the problem domain, that is

$$\sum_{j=1}^{n} \phi_j(\vec{x}) = 1 \tag{3.23}$$

where, n is the number of shape functions which is equal to the number of nodes used in the support domain and $\phi_i(\vec{x})$ is the shape function at the i^{th} node. Third, the field value approximation must be able to reproduce a linear field.

$$\sum_{j=1}^{n} \phi_j(\vec{x}) x_j = \vec{x} \tag{3.24}$$

Last, shape functions are preferable to possess the Kronecker delta function properties as follows

$$\phi_j(\vec{x}_i) = \delta_{ij}, \left(i = 1,2,\cdots,n;\ j = 1,2,\cdots,n\right) \tag{3.25}$$

Additionally, the shape functions of all nodes in the whole problem domain are

required to be compatible in the global weak-form approach. Numerical consistency had better to be satisfied for the interpolations of position vector and Lagrange multiplier considering the constraint condition demonstrated in Eq. (4.9).

The governing equation expressed in Eq. (4.8) is based on the undeformed configuration, which assumes that a small elongation doesn't significantly differentiate the stretched configuration from unstretched one. Some assumptions about a cable are adopted: uniformly distributed mass, uniform bending stiffness, and constant axial stiffness. The theoretical formulation can be divided into five parts:

1) Field value interpolation using RPIM with polynomial reproduction

Field values needed for interpolation include the position of a cable in the global Cartesian coordinate, the Lagrange multiplier related to tension, and the distributed load including drag force from seafloor and trawling force. The slope at point of interest on a cable is considered an independent variable which is first proposed by Wu (1992) for data interpolation using radial basis functions (RBFs). Polynomial terms are introduced to RPIM based upon the following considerations: (1) ensure the some resultant matrices are invertible when constructing shape functions; (2) guarantee the shape function can reproduce a linear field and retain numerical consistency; and (3) improve numerical accuracy. Hermite-type RPI (HRPI) functions are adopted to ease the implementation of natural boundary conditions including position and tangent. By adopting the enhanced HRPI, the three primary field values are approximated in a local support domain. The approximation of λ and q are independent of the position vector using polynomial only (summation of dummy index is applied.).

$$\begin{aligned}\vec{r}(s,t) &= u_l^h(s,t)\vec{e}_l \\ \lambda(s,t) &= p_j(s)\beta_j \\ \vec{q}(s,t) &= q_l^h(s,t)\vec{e}_l\end{aligned} \tag{3.26}$$

where,

the superscript *h* denotes a local support domain;

l=1-3 is a dummy index corresponding to components in *x*, *y*, and *z* direction;

j=1-*m* and *m* is the number of polynomial terms;

$\vec{e}_l$ is a unit base vector in the global coordinate;

p_j is a monomial and β_j is the corresponding coefficient;

$u_l^h(s,t)$ and $q_l^h(s,t)$ are the component terms in the global coordinate, which are approximated using RBFs with polynomial reproduction and pure polynomial basis respectively as follows

$$u_l^h(s,t) = \sum_{i=1}^{n} R_i(s)\alpha_{li} + \sum_{i=1}^{n} \frac{\partial R_i}{\partial s}(s)\alpha_{li}^s + \sum_{j=1}^{k} p_j(s)\beta_{lj}^u = \boldsymbol{R}^T\boldsymbol{\alpha}_l + \boldsymbol{R}_{,s}{}^T\boldsymbol{\alpha}_l^s + \boldsymbol{p}^T\boldsymbol{\beta}_l^u \tag{3.27}$$

$$q_l^h(s,t) = \sum_{j=1}^{m} p_j(s)\beta_{lj}^q = \boldsymbol{p}^T\boldsymbol{\beta}_l^q \tag{3.28}$$

where,

$R_i(s) = R(d_i), \left(d_i^2 = (s - s_i)^2\right)$ is a RBF and $p_j(s)$ is a monomial;

$\boldsymbol{R}^T = \left[R_1(s), R_2(s), \cdots, R_n(s)\right]$ and $\boldsymbol{p}^T = \left[1, s, \cdots, s^{k-1}\right]$ for $u_l^h(s,t)$;

$\boldsymbol{p}^T = \left[1, s, \cdots, s^{m-1}\right]$ for $q_l^h(s,t)$;

‘,*s*’ represents the first derivative with respect to arc-length *s*;

n is the number of nodes in the local support domain;

The RBFs adopting modified multi-quadric (MQ) will be employed in the study. The shape parameters are critical to the approximation performance of the Hermite-type RBF. To determine the coefficients α and β in Eq. (4.16), the interpolation functions are forced to pass through all nodes and to possess an equal tangent at each node in the local support domain. Different from the deflection interpolation with slope as an independent variable, see for example (Atluri et al., 1999, Gu and Liu, 2001 and Liu, 2006), the small-angle approximation is not applicable in this study since position interpolations are adopted. However, the tangent vector can be described by the first derivative of Eq. (4.16) with respect to the arc-length *s* in the global Cartesian coordinate. Moreover, the three position vector components are approximated independently.

$$\begin{cases} A\boldsymbol{\alpha}_l + A_s\boldsymbol{\alpha}_l^s + C\boldsymbol{\beta}_l^u = \boldsymbol{X}_l \\ A_s\boldsymbol{\alpha}_l + A_{ss}\boldsymbol{\alpha}_l^s + C_s\boldsymbol{\beta}_l^u = \boldsymbol{\Theta}_l \end{cases} \tag{3.29}$$

where,

$\boldsymbol{X}_l = \left(u_{l1}, u_{l2}, \cdots, u_{ln}\right)^T, \boldsymbol{\Theta}_l = \left(\cos\theta_{l1}, \cos\theta_{l2}, \cdots, \cos\theta_{ln}\right)^T, l = 1,2,3;$

$\left(u_{1j}, u_{2j}, u_{3j}\right)$ and $\left(\cos\theta_{1j}, \cos\theta_{2j}, \cos\theta_{3j}\right) = \left(u_{4j}, u_{5j}, u_{6j}\right)$ is the position and the tangent of node in the global Cartesian coordinate corresponding to $\vec{r}\left(s_j, t\right)$;

$A_{ij} = R_j\left(s_i\right) = A_{ji},\ A_{sij} = R_{j,s}\left(s_i\right) = -A_{sij},\ A_{ssij} = R_{j,ss}\left(s_i\right) = A_{ssji},\ i, j = 1-n;$

$C_{ij} = p_j\left(s_i\right),\ C_{sij} = p_{j,s}\left(s_i\right),\ i, j = 1-n,\ j = 1-k;$

subscript *ij* of A, A_s, A_{ss}, C, and C_s represents the (*i*,*j*) element;

Additionally, constraints conditions on the polynomial terms used in Eq. (4.16) are needed to obtain a unique set of coefficients in each local support domain. Complementary 3*k* equations are introduced by the following constraint conditions

$$\sum_{i=1}^{n} p_j(s_i)\alpha_{li} + \sum_{i=1}^{n} p_{j,s}(s_i)\alpha_{li}^{s} = 0, \tag{3.30}$$

where, $l = 1,2,3$ and $j = 1-k$. In the matrix form, they can be written as

$$C^T \boldsymbol{\alpha}_l + C_s^T \boldsymbol{\alpha}_l^s = 0 \tag{3.31}$$

Considering Eq. (4.18) and Eq. (4.19), the equations in matrix form are

$$G\begin{Bmatrix} \boldsymbol{\alpha}_1 \\ \boldsymbol{\alpha}_1^s \\ \boldsymbol{\beta}_1^u \end{Bmatrix} = \begin{Bmatrix} \boldsymbol{X}_1 \\ \boldsymbol{\Theta}_1 \\ 0 \end{Bmatrix}, \quad G\begin{Bmatrix} \boldsymbol{\alpha}_2 \\ \boldsymbol{\alpha}_2^s \\ \boldsymbol{\beta}_2^u \end{Bmatrix} = \begin{Bmatrix} \boldsymbol{X}_2 \\ \boldsymbol{\Theta}_2 \\ 0 \end{Bmatrix}, \quad G\begin{Bmatrix} \boldsymbol{\alpha}_3 \\ \boldsymbol{\alpha}_3^s \\ \boldsymbol{\beta}_3^u \end{Bmatrix} = \begin{Bmatrix} \boldsymbol{X}_3 \\ \boldsymbol{\Theta}_3 \\ 0 \end{Bmatrix} \tag{3.32}$$

where, $G = \begin{bmatrix} A & A_s & C \\ A_s & A_{ss} & C_s \\ C^T & C_s^T & 0 \end{bmatrix}$.

When the coefficients in Eq. (4.15) are resolved, the approximation of position is

$$u_l^h(s,t) = \begin{bmatrix} \boldsymbol{R}^T & \boldsymbol{R}_{,s}^T & \boldsymbol{p}^T \end{bmatrix} G^{-1} U_l = \Phi U_l \tag{3.33}$$

where,

$$\phi_g(s) = \sum_{i=1}^{n} R_i(s) G_{i,\mathrm{g}}^{-1} + \sum_{i=1}^{n} R_{i,s}(s) G_{i+n,\mathrm{g}}^{-1} + \sum_{j=1}^{k} p_j(s) G_{j+2n,\mathrm{g}}^{-1},\ g = 1-2n$$

$$U_l = \left[\boldsymbol{X}_l, \boldsymbol{\Theta}_l\right]^T,\ l = 1,2,3.$$

Similarly, the coefficients for tension and distributed load interpolations can be obtained by imposing interpolation functions to equal the nodal values at all nodes.

$$\lambda(s,t) = \boldsymbol{p}^T P^{-1}\hat{\lambda} = \Phi^{\lambda}\hat{\lambda} \tag{3.34}$$

$$q_l^h(s,t) = \boldsymbol{p}^T P^{-1} Q_l = \Phi^q Q_l \tag{3.35}$$

where, $\boldsymbol{p}^T = \left[1, s, \cdots, s^{m-1}\right]$, $P_{ij} = p_j(s_i)$, $\hat{\lambda} = \left[\lambda_1(t), \cdots, \lambda_m(t)\right]^T$, $Q_l = \left[q_{l1}, q_{l2}, \cdots, q_{ln}\right]^T$.

The properties of shape functions using MQ based RPI approach is first demonstrated by a two-dimensional curve which is represented by four nodes shown in Tab. 4.3. The shape parameters C=0.005 and q=1.5 are used herein. The curve is expressed by a function shown in Eq. (4.25) in the domain $\left[0, \pi/2\right]$.

$$x = t, y = \sin t, s = \int_0^t \sqrt{1+\cos^2 u}\, du \tag{3.36}$$

Table 4.3 Node distribution of the tested curve

No.	s	x	y	θ_x	θ_y
1	0	0	0	45˚	45˚
2	0.7241	0.5236	0.5000	40.9˚	49.1˚
3	1.3646	1.0472	0.8660	26.6˚	63.4˚
4	1.9101	1.5708	1.000	0˚	90˚

The RPI shape functions with linear polynomials is shown in Fig. 4.6(a), which doesn't use the tangent vector information. Fig. 4.6(a) shows the Kronecker delta property of all four shape functions. Also the unity partition requirement expressed by Eq. (4.12) has been confirmed for these shape functions in this example. Consequently, the reproduction of linear field are also satisfied. The cubic shape functions independent of nodal distribution are presented in Fig. 4.6(b). Shape functions N_1 and N_3 associated with nodal value also possess the Kronecker delta property.

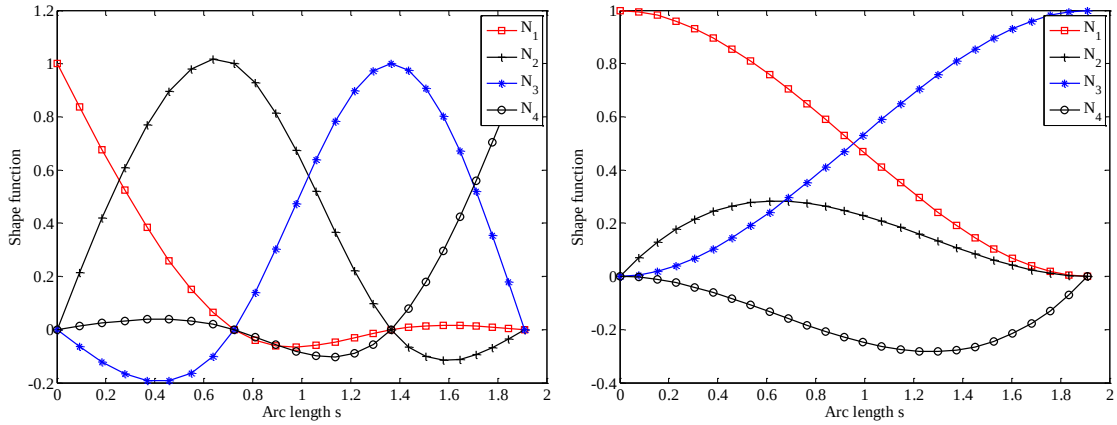

(a) RPI shape functions (b) FEM cubic shape functions (Garret, 1982)

Fig. 4.6 Shape functions for RPIM and FEM formulation

Curve fitting performance of this MQ-RBF is evaluated using shape parameters suggested by Wang and Liu (2002). The fitted positions at points of interest on the curve are plotted against exact value and nodal values in Fig. 4.7. The fitted values pass all four nodes attributed to the Kronecker delta property of shape functions. Interpolations utilizing the MQ-RBF in the RPIM formulation are compared to that using cubic shape functions in Garret's FEM formulation in Fig. 4.8. Both of these two interpolations used four nodal values: (1) RPI used four nodes where each node has one nodal value, and (2) FEM two end nodes for which each node has one position and one slope term. It can be seen that the RPI provides more accurate interpolation than cubic shape functions. However, MQ-RBF interpolation predicts worse results at the ends of curves. This edge property is to be demonstrated by $y = x + x^3/100 + \sin(x)$ in the domain of [0, 7]. This curve fitting uses 10 nodes and the same shape parameter as the first curve fitting example. The nodal distribution, interpolated value and exact value are

plotted in Fig. 4.9(a). The error of interpolated values are presented in Fig. 4.9(b) where the edge feature is revealed and the error decays when points are close to center of the interpolated domain.

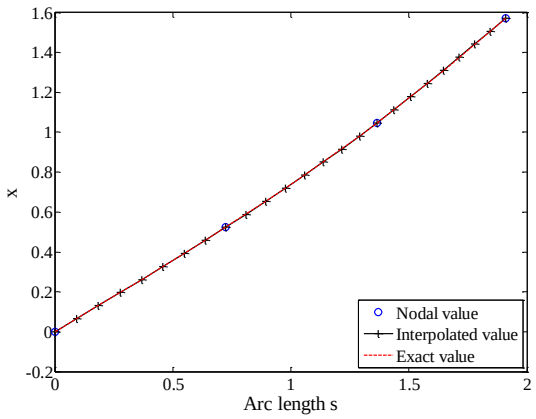

(a) Fitted x with respect to arc length

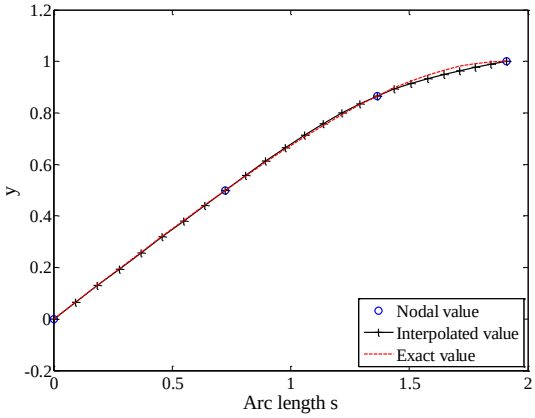

(b) Fitted y with respect to arc length

Fig. 4.7 Interpolated Cartesion coordinates with respect to arc length s

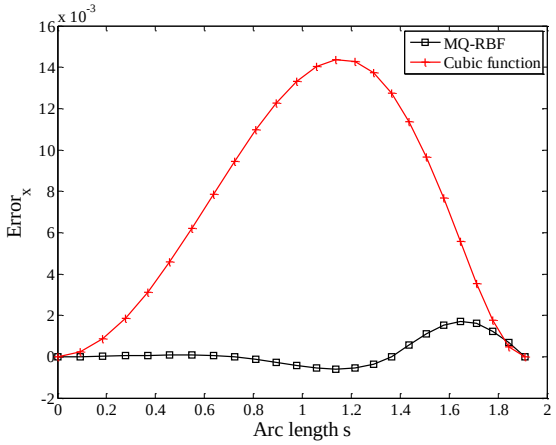

(a) Fitted error of x with respect to s

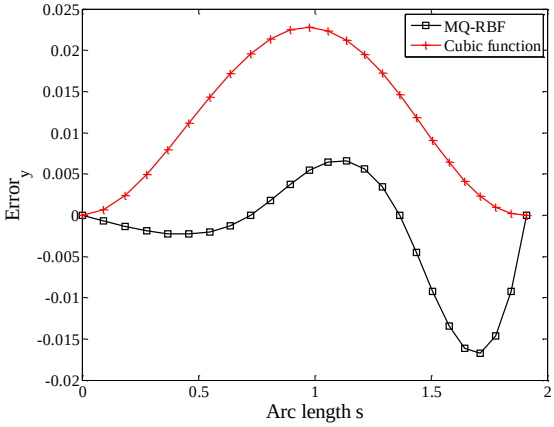

(b) Fitted error of y with respect to s

Fig. 4.8 Interpolated errors using MQ-RBF and cubic shape functions

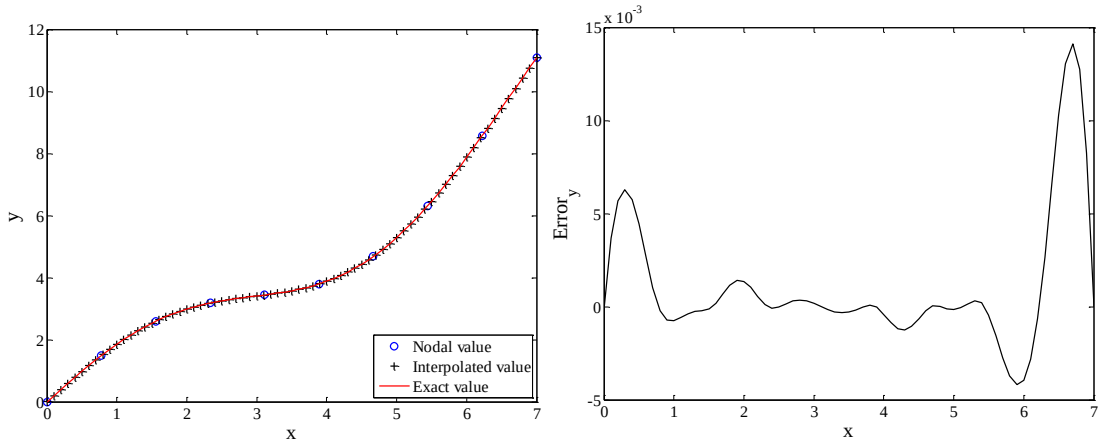

(a) Fitted *y* with respect to *x* (b) Fitted error of *y* with respect to *x*

Fig. 4.9 Edge property of interpolated function using MQ-RBF

2) Local weak formulation of governing equations

Considering Eq. (4.8), the weak formulation is performed by making the residual of governing equation to zero in an integral form over a local support domain. Since the weight function plays a critical role on the numerical performance of a meshfree method, it should at least satisfies the condition of continuity (Alturi, 1999 and Liu and Gu, 2001). Although the spline weight function may simplify the numerical integration procedure, it is not sufficient to apply in the HRPIM as derivative is included in the field value approximation. Due to the same reason, Gu and Liu (2001) adopted the weight functions using the same basis as the field interpolations. To be specific, this weighted residual technique is called Galerkin formulation.

$$\int_{\Omega_s} \left\{ \rho \ddot{\vec{r}} + EI\vec{r}^{(4)} - \left(\lambda \vec{r}'\right)' - \vec{q} \right\} \delta r_l = 0 \tag{3.37}$$

where, Ω_s is the local domain for weight functions, and δr_l (l=1,2,3) is a weight

function in the domain. Regarding arbitrary independent virtual nodal displacement and integrating by part of Eq. (4.26), yield in

$$\int_{\Omega_s} \left\{ \rho \ddot{\vec{r}} \phi_j + EI\vec{r}^{''} \phi_j^{''} + \lambda \vec{r}^{'} \phi_j^{'} - \vec{q}\phi_j \right\} ds = \left\{ EI\vec{r}^{''} \phi_j^{'} + \left(\lambda \vec{r}^{'} - EI\vec{r}^{'''} \right) \phi_j \right\} \Big|_0^L \tag{3.38}$$

where, $\phi_j^{'} = \phi_{j,s}$, $\phi_j^{''} = \phi_{j,ss}$, $j = 1-2n$, and L is the length of local domain. The right hand side of represents natural boundary conditions associated with internal moments and forces at the ends of the support domain.

3) Discretization of the weak formulation

Substituting Eq. (4.22) thru. (4.24) into the weak form Eq. (4.27) leads to a set of discrete equations for a cable allowing a small elongation (summation is employed)

$$\begin{aligned} &\rho \left\{ \int_{\Omega_s} \phi_k \phi_j ds \right\} \ddot{U}_{lk} + EI \left\{ \int_{\Omega_s} \phi_k^{''} \phi_j^{''} ds \right\} U_{lk} + \left\{ \int_{\Omega_s} \phi_i^{\lambda} \phi_k^{'} \phi_j^{'} ds \right\} \lambda_l U_{lk} \\ &= \left\{ \int_{\Omega_s} \phi_i^{q} \phi_j ds \right\} Q_{li} + f_{lj} \end{aligned} \tag{3.39}$$

where, $l = 1-3$, $k = 1-2n$, $j = 1-2n$, $i = 1-m$, and $f_{lj} = \left\{ EIr_l^{''} \phi_j^{'} + \left(\lambda r_l^{'} - EIr_l^{'''} \right) \phi_j \right\} \Big|_0^L$ which has only contribution on free ends of the cable in the global algebraic equation.

4) Compute the inertia and point stiffness term

To simplify the numerical implementation of the HRPIM, the number of polynomial terms *m* is selected to equal to the number of nodes *n* in the local domain. In respect of numerical integration in Eq. (4.28), either the nodal integration (Liu et al., 2007) or the standard Gauss quadrature may be employed to compute the inertia and stiffness coefficients. On one hand, the general force terms will be vanish when the natural boundary condition is applied. On the other hand, these force terms is not

required to be explicitly computed when the essential boundary conditions are imposed at the free ends of the cable. Then, the discretized form of equation of motion of the local domain on the cable can be obtained with *l* and *j* as the free index

$$\rho\gamma_{kj}\ddot{U}_{lk} + EI\alpha_{kj}U_{lk} + \beta_{ikj}\lambda_i U_{lk} = \mu_{ij}Q_{li} + f_{lj} \tag{3.40}$$

where,

$$U_1 = \left[u_{11}, u_{12}, \cdots, u_{1n}, u_{41}, u_{42}, \cdots, u_{4n}\right]^T;$$

$$U_2 = \left[u_{21}, u_{22}, \cdots, u_{2n}, u_{51}, u_{52}, \cdots, u_{5n}\right]^T;$$

$$U_3 = \left[u_{31}, u_{32}, \cdots, u_{3n}, u_{61}, u_{62}, \cdots, u_{6n}\right]^T;$$

$$\gamma_{kj} = \int_{\Omega_s} \phi_k \phi_j ds;\ \alpha_{kj} = \int_{\Omega_s} \phi_k^{''} \phi_j^{''} ds;\ \beta_{ikj} = \int_{\Omega_s} \phi_i^{\lambda} \phi_k^{'} \phi_j^{'} ds;\ \mu_{ij} = \int_{\Omega_s} \phi_i^{q} \phi_j ds.$$

Similarly, the constraint condition expressed in Eq. (4.9) can be also discretized in the same local domain assuming the curvature is small.

$$\beta_{ikj}U_{lk}U_{lj} = \tau_i + 2\eta_{ig}\varepsilon_g + \tilde{\gamma}_{igp}\varepsilon_g\varepsilon_p - \tilde{\gamma}_{igg}\varepsilon_g\varepsilon_g \tag{3.41}$$

where,

$$\tau_i = \int_{\Omega_s} \phi_i^{\lambda} ds,\ \eta_{ig} = \int_{\Omega_s} \phi_i^{\lambda} \phi_g^{\lambda} ds,\ \tilde{\gamma}_{igp} = \int_{\Omega_s} \phi_i^{\lambda} \phi_g^{\lambda} \phi_p^{\lambda} ds,\ i, g, p = 1 - n.$$

It should be noted that all the nodal terms use local numbering systems and all coefficients will be assembled into the global algebraic equation using a global numbering system with the numbering of node from 1 to *N* (*N* is the number of nodes used in the entire domain). Therefore, considering Eq. (4.29) and Eq. (4.30), 7*N* nodal terms can be formulated in 7*N* algebraic equations. Moreover, the discretized motion of equation are nonlinear equations shown in Eq. (4.29) due to the coupling of tension and

position vector of one stiffness coefficient term.

In summary, as long as the union of the local domains can cover the entire problem domain and the boundary condition of each local domain is applied in the global system equation, the equilibrium of the entire problem domain and boundary conditions on the free ends will be satisfied using this local HRPIM meshfree method.

5) Static analysis procedure

Since the towing speed of trawl gears is low, the vibration of cable during the interaction of gears and cables may not be significant under the scenarios considered in the current work and may be investigated when necessary. Static problem is first solved to study the response behavior of cables under movable boundary conditions. For easy implementation, Newton's method is adopted here as earlier studies Garret (1982), Ma et al., and Chen (2002). Assuming an initial guess and introducing a disturbance of position vector and λ lead to

$$\begin{cases} U_{lk} = U_{lk}^0 + \delta U_{lk} \\ \lambda_i = \lambda_i^0 + \delta\lambda_i \end{cases} \tag{3.42}$$

Substituting new values into Eq. (4.29) and Eq. (4.30), neglecting time associated term, getting rid of high order terms in respect of the disturbances and neglecting the deviation of the stretch in the vertical direction resulted from gravity, yield in

$$\left(EI\alpha_{kj} + \beta_{ikj}\lambda_i^0\right)\delta U_{lk} + \beta_{ikj}U_{lk}^0\delta\lambda_i = \mu_{ij}Q_{li} - EI\alpha_{kj}U_{lk}^0 - \beta_{ikj}\lambda_i^0 U_{lk}^0 + f_{lj} \tag{3.43}$$

$$\beta_{ikj}U_{lj}^0\delta U_{lk} - \eta_{ig}\frac{\delta\lambda_g}{EA} = \frac{1}{2}\left(\tau_i + 2\eta_{ig}\varepsilon_g^0 - \beta_{ikj}U_{lj}^0U_{lk}^0\right) \tag{3.44}$$

To facilitate the assembly of the global equation, the nodal terms in the local

domain is rearranged as $\boldsymbol{u}^T = [u_{11}, \cdots, u_{61}, \lambda_1, \cdots, u_{1n}, \cdots, u_{6n}, \lambda_n]$. Then, the incremental form of the equation of motion and constraint condition may be written

$$A\delta \boldsymbol{u} = B \tag{3.45}$$

where, A is a coefficient matrix evaluated by the left hand side of in Eq. (4.32) and Eq. (4.33) and B is computed by the right hand side of Eq. (4.32) and Eq. (4.33).

According to the aforementioned algorithm, the static problem is iteratively solved until boundary conditions at free ends of the cable are satisfied including position and tangent. As the shape functions constructed by HRPI possess the Kronecker delta property, the essential boundary conditions can be imposed directly without any additional efforts such as penalty method in other point interpolation methods PIM and RPIM. At the converged step, the internal resultant forces such as axial tension and moment can be achieved for the structural evaluation of the cable.

4.3 Numerical Implementation of the Meshfree Method

The formulated Meshfree method is to be implemented in Matlab using the working flow chart presented in Fig. 4.10. The steps circled by the dash frame is the iteration scheme for one incremental force step, where the trawling force may be distributed at the contact region of a gear and a cable. The initial layout of a cable is given and the response behavior of the cable under trawling is the purpose of study.

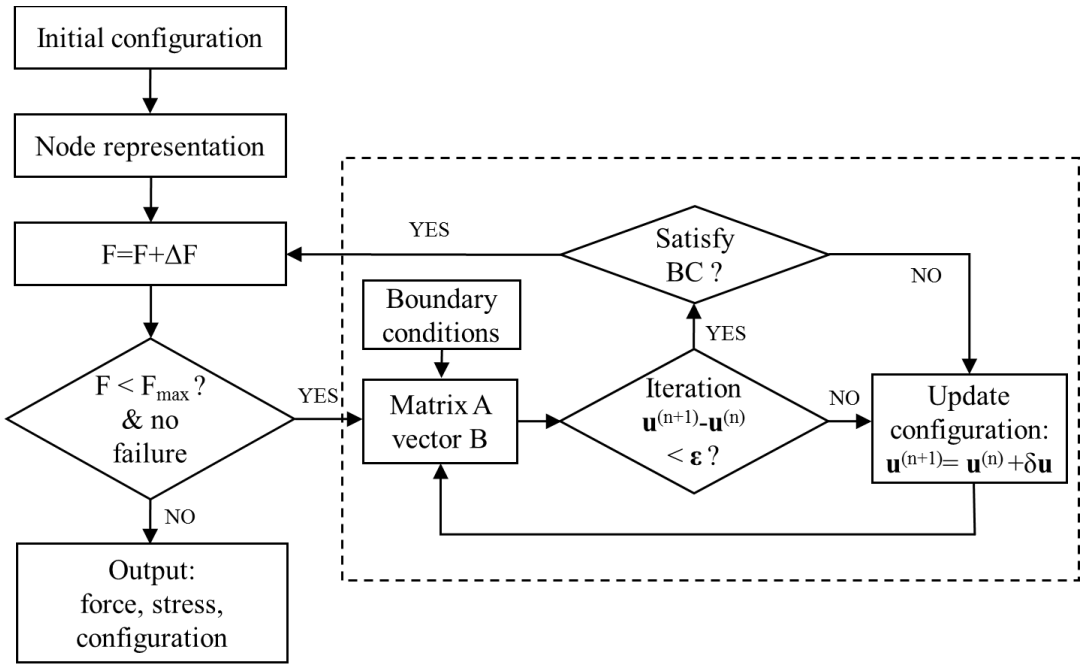

Fig. 4.10 Flow chart of the static analysis program

One critical step of the static analysis is to form the stiffness coefficient matrix A and the vector B using the further developed HRPIM based upon local weak formulation. The most general procedure to evaluate point stiffness matrix by the local weak form meshfree method is incorporated with the current configuration as shown in Fig. 4.11 to evaluate matrix A and vector B by Eq. (4.34). The standard Gauss quadrature is adopted for the numerical integration in Eq. (4.29) and Eq. (4.30).

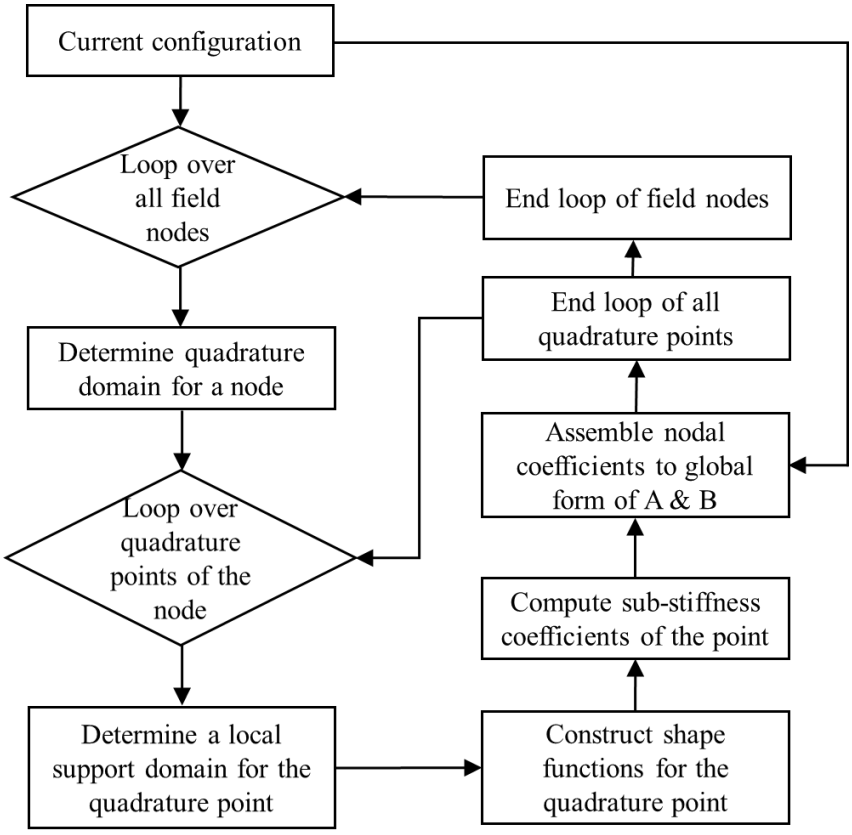

Fig. 4.11 Flow chart of computing coefficient matrix A and vector B

Different from the FEM approach, quadrature points in the same quadrature domain of a node may use different local support domains for the construction of shape functions in this meshfree method. This special treatment may improve the interpolation accuracy by overcoming the edge property as illustrated in Fig. 4.9(b). However, the trade-off is paid by much more complicated integrand for the evaluation of point stiffness coefficient due to overlap of the local interpolation domains of different quadrature points.

There are three different local domains involved in the local HRPIM method: (1)

the weight function domain Ω_s at which the weight functions is constructed, (2) the integration domain Ω_q for Gauss quadrature, and (3) the interpolation domain Ω_i for a quadrature point to compute shape functions for this point. The requirement $\Omega_q \leq \Omega_s$ must be satisfied as the weighted residual technique is applied to the weight function domain and integration is performed inside the weight function domain. When all quadrature points in one quadrature domain use the weight function domain, the numerical integration procedure is the same as FEM. The meshfree method is still different from FEM as different integration domains adopt different local support shape functions in meshfree methods. In contrast, FEM uses the same shape functions for the same type element all through the problem domain.

A few numerical issues are needed for further investigations by the two benchmark examples. In respect of the order of consistency for position vector and λ in Eq. (4.8) and Eq. (4.9), number of node, highest order of the polynomial term for λ , and shape parameter should be selected properly to meet the consistency requirement. Regarding numerical integration for coefficient matrix, number of quadrature points in the Gauss quadrature is to be determined. Numerical convergence and adaptive analysis are to be investigated in terms of density and distribution of field nodes. In addition, the parameter sensitivity of shape parameters for shape function construction using the MQ-RBF need more study in these benchmark cases.

4.4 Program Validation

A computer program is developed in Matlab based upon the further developed meshfree method formulated in detail in the precious section. It is to be validated by two benchmark examples, which are also compared with FEM results using the same slender rod theory (Garret, 1982, Ma and Webster, 1994) to reveal the effectiveness and demonstrate the accuracy of the meshfree method LHRPIM. These two cases are also adopted to perform numerical convergence and parametric study.

Intended to validate the developed meshfree formulation for a slender cable, the post buckling behavior of a column is adopted, which was first theoretically studied by Love (1944). The column steps into large deflection stage rather than immediate collapse after the initial buckling. Fig. 4.12 depicts the elastic behaviors of a column when the compressive load P exceeds the critical load. θ is the angle between the tangent direction at the top end of the column and the vertical direction. The original length of the column is L. The bottom end is clamped and the top end is free. A few numerical cases using regularly distributed nodes are compared with Timoshenko's analytical results (1936) listed in Tab. 4.4 for convergence study and parametric investigation. When L=3 m, the maximum vertical difference is less than 5% when only three nodes are used. As can be concluded, the numerical results converge to analytical solution when more nodes are used. Regarding numerical accuracy, the developed local Hermite-RPIM is excellent even if the three meters long column is only represented by 7 nodes.

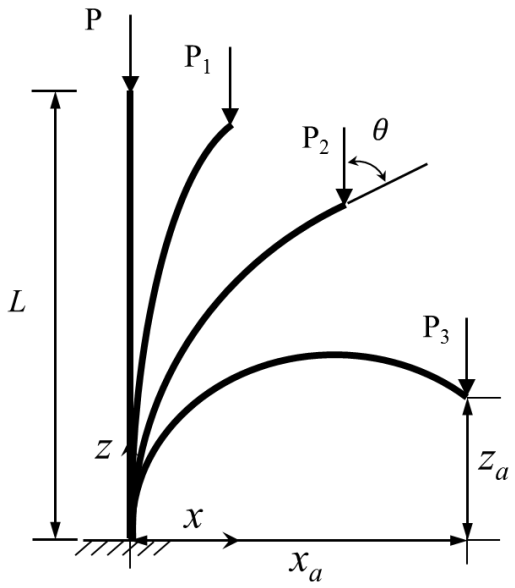

Fig. 4.12 Post buckling of a column

Table 4.4 Numerical results of the deflection data for the column

Analytical		Meshfree					P/Pc
		3	7	11	15	25	
θ (˚)	60	58.485	59.938	59.984	59.995	60.000	1.1521
	100	98.412	99.883	99.951	99.965	99.985	1.5184
	120	118.857	119.862	119.941	119.958	119.970	1.8844
	140	140.666	139.874	139.958	139.976	139.987	2.5423
x_a/L	0.5932	0.5803	0.5927	0.5931	0.5931	0.5932	1.1521
	0.7915	0.7845	0.7912	0.7914	0.7915	0.7915	1.5184
	0.8032	0.8012	0.8032	0.8032	0.8032	0.8032	1.8844
	0.7504	0.7564	0.7508	0.7506	0.7505	0.7504	2.5414
z_a/L	0.7410	0.7549	0.7416	0.7412	0.7411	0.7410	1.1521
	0.3491	0.3751	0.3505	0.3496	0.3494	0.3492	1.5184
	0.1234	0.1563	0.1252	0.1240	0.1237	0.1235	1.8844
	-0.1069	-0.0640	-0.1045	-0.1062	-0.1066	-0.1068	2.5410

Note: P_c is the critical load for initial buckling and (x_a, z_a) is the position of the free end.

The fast convergence rate in part is attributed to the accuracy of the HRPI

scheme adopted for field value interpolation. The performance of HRPI are illustrated with intend to provide a visual perspective of its capability using three nodes. The follow curve is used for demonstration in the domain $[0,\pi/2]: x=\sin t, y=\cos t, \mathrm{s}=\mathrm{t}$. Considering field value interpolation accuracy, the optimal shape parameters C=0.05 and q=2.1 are used. The interpolation of field value, first and second derivatives are presented in Fig. 4.13. As can be seen even the second derivatives can get good approximations.

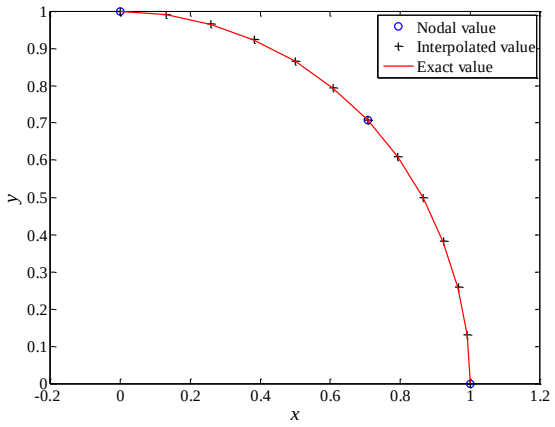

(a) Interpolated curve

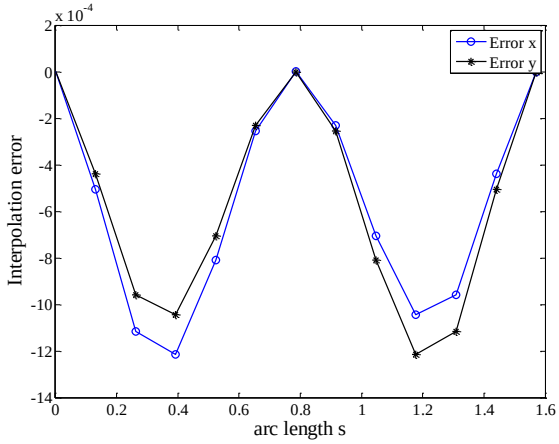

(b) Interpolation error

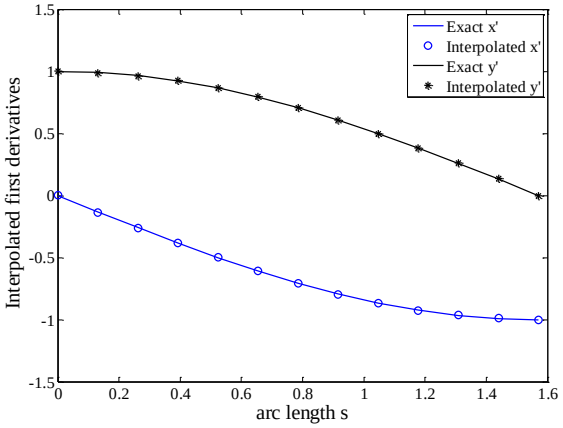

(c) Interpolated first derivatives

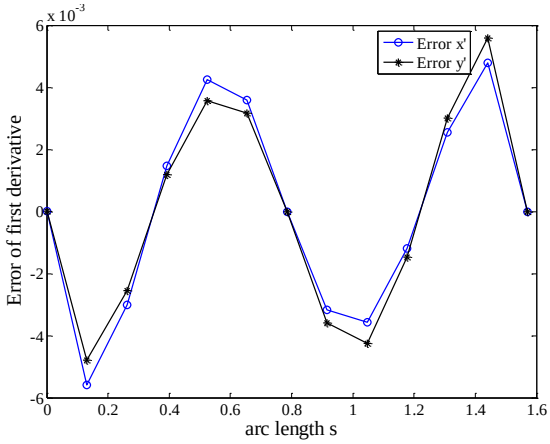

(d) Interpolated error of first derivatives

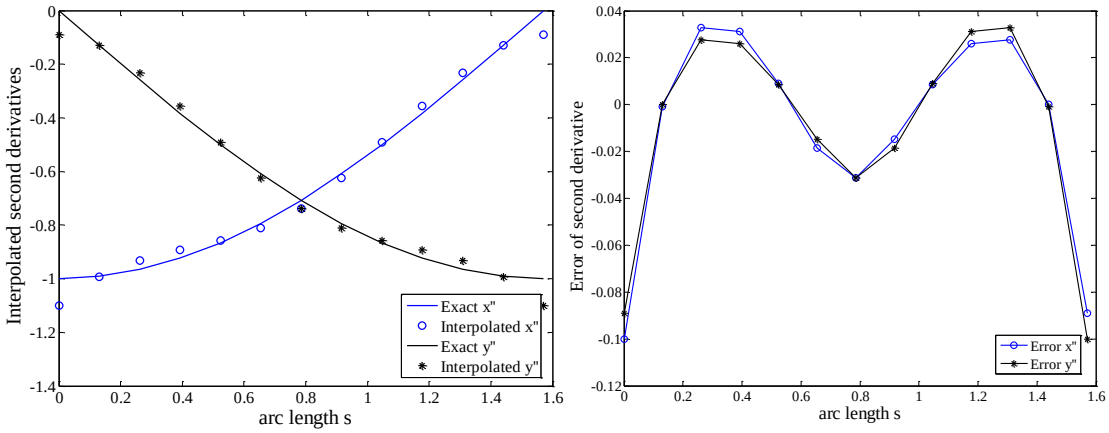

(e) Interpolated second derivatives (f) Interpolated error of second derivatives

Fig. 4.13 Illustration of interpolation performance of HRPI

The influence of the number of Gauss points for numerical integration of point stiffness on the accuracy is investigated under the case P/Pc=1.1521. The corresponding positions of the free end of the column are presented in Fig. 4.14. The results reveal that 4 quadrature points can reach the same accuracy as the case using 12 points. Thus, less points can be used for considerate long slender cables without trade-off of accuracy.

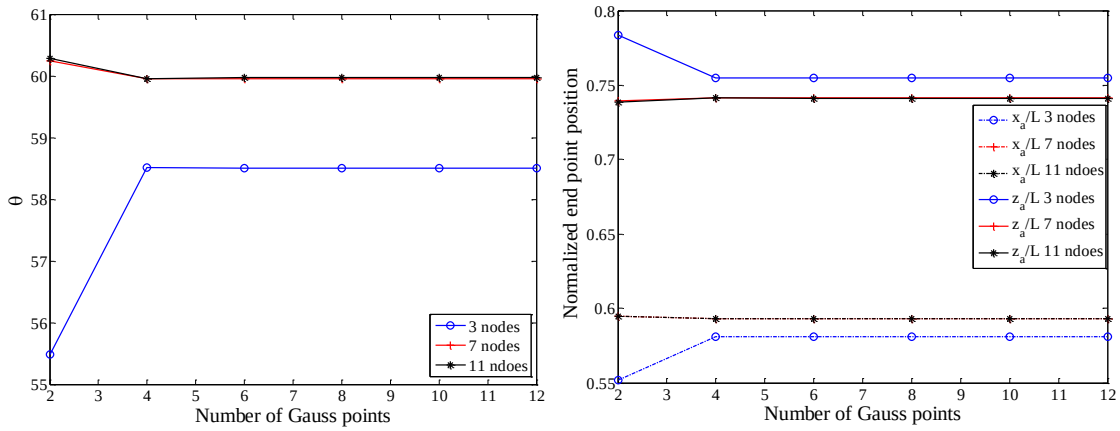

Fig. 4.14 Position of the free end of the column

According to a parametric study on the shape parameter C, it must be a small number in the range of 0.001~0.18 in order to get rid of singularity issues for this problem. 0.001~0.05 is suggested to be used considering accuracy and numerical stability. Moreover, q is a more critical shape parameter in respect of accuracy. Fig. 4.15 shows the errors of the free end using C=0.05 and 11 nodes. According to Wang and Liu (2002), the shape parameter q is investigated in the range [1.01, 3.0]. However, stable and accurate results are obtained in the range of [1.85, 2.15], which is consistent with the optimal parameter range in respect of the interpolation accuracy of field values when construct shape functions. Note that q cannot be integer otherwise singularity issue rises.

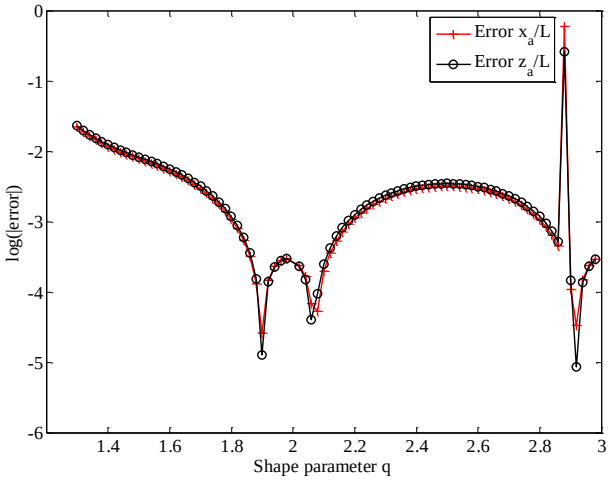

Fig. 4.15 Logarithm error of the normalized end point

For purpose of comparative study with FEM formulation (Garret, 1982), a second case is studied about a catenary shown in Fig. 4.16 with uniform distributed

weight and no bending stiffness, which is dragged by a horizontal force P at the free end.

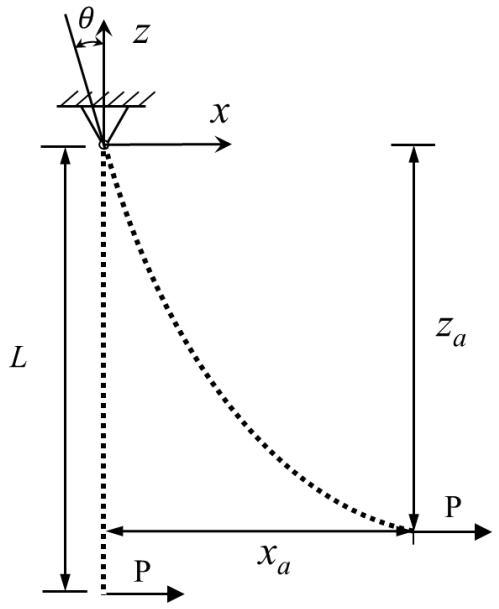

Fig. 4.16 Top pinned catenary with prescribed force at the free end

Both meshfree and FEM results are provided in Tab. 4.5, the position converges faster than the top angle. When 11 nodes are used in the further developed LRPIM, it gives excellent agreement with FEM beside the heeled angle. However, more equations are involved in the FEM simulation due to the middle dummy nodes at each element for the interpolation of the Lagragian multiplier λ. It increases the computation cost for FEM from this point. However, the interpolation is much more complicated and should be performed for each subdomain which increases the computation cost of the LRPIM. Both numerical methods are able to make accurate prediction with a few nodes for these two benchmark examples, which validates their accuracy and efficiency.

Table 4.5 Comparison of meshfree and FEM results

	Meshfree (node)			FEM (element)		WL/P
	3	5	11	1	10	
θ (°)	44.545	44.906	44.983	44.626	45.000	1
	25.874	26.477	26.551	26.723	26.566	2
	11.658	11.273	11.304	14.295	11.311	5
	7.336	5.759	5.708	9.280	5.711	10
x_a/L	0.8814	0.8814	0.8814	0.8814	0.8814	1
	0.7216	0.7218	0.7218	0.7219	0.7218	2
	0.4629	0.4623	0.4625	0.4676	0.4625	5
	0.3033	0.3001	0.2998	0.3017	0.2998	10
z_a/L	-0.4142	-0.4142	-0.4142	-0.4143	-0.4142	1
	-0.6179	-0.6180	-0.6180	-0.6179	-0.6189	2
	-0.8179	-0.8196	-0.8198	-0.8222	-0.8189	5
	-0.9046	-0.9039	-0.9050	-0.9206	-0.9050	10

Note: 10 elements in the FEM scheme contains 11 nodes and 10 dummy points.

5. APPLICATION TO THE INTERACTION OF TRAWLING AND CABLES

Since the fishing activities mainly the modern bottom trawling fishing induce damage to subsea cables, a specification overview of cables benefits the understanding of damage and possible failure modes. Light cable shown in Fig. 5.1(a) is introduced to supply power for oil and gas production units and connect wind turbine terminates to land grids. The outer diameter of light cables is typically in the range of 40~100 *mm* and the unit weight runs from 4.7 to 29 *kg/m*. The outer diameter of an optic fiber cable is typically around 70 *mm*. Single core power cable mainly comprises of conductor, polyethylene insulation, screen layer, steel armor and outer protection. Optic fiber presented in Fig. 5.1(b) which is more vulnerable to damage usually incorporates stronger armor layers.

(a) HVDC light cable (Courtesy of ABB) (b) Optic fiber cable (Courtesy of Ericsson)

Fig. 5.1 Power cable and telecom cable for offshore applications

In the energetic zone typically coastal seas where bottom trawling fishing are

active, trawl gears may frequently sweep on the seafloor and may be occasionally tangled with these submarine cables. Trawl scars were recorded as shown in Fig. 5.2(a) and (b) and some cable damages were reported see for example in Fig. 5.2(c) and (d).

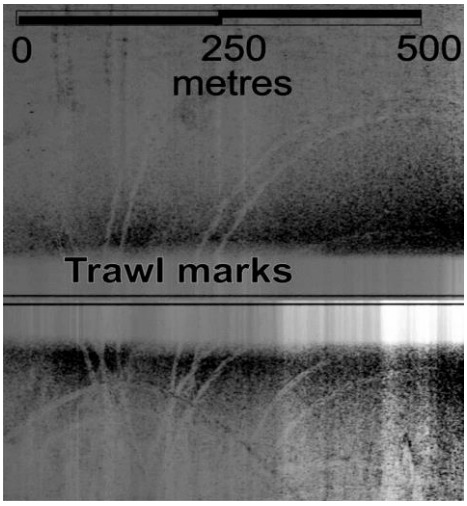

(a) Sonar image of trawl scars

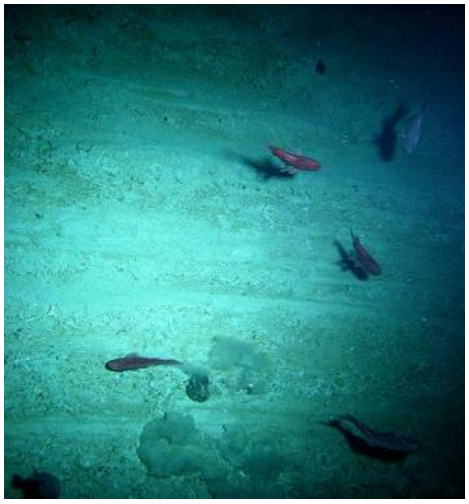

(b) Trawl scars on the seafloor

(c) Cable damage by trawl gears

(d) Cable snagged by a fishing gear

(International Cable Protection Committee, 2010)

Fig. 5.2 Impact of trawl fishing activities on sea floor and submarine cables

Due to the mechanical performance discrepancy of the core of power cable and

optic fiber cable, the possible failure mode varies from power cables to optic fiber cable, which may also depend on design specification for the same type of cable. The bend radius of fiber cable is restricted to 20 cable diameters. Possible structural damages to the cores may include the following patterns: (1) bending is in excess of the allowable bend radius; (2) tension exceeds the axial breakage load of the armor layer.

This chapter focuses on the application of the LHRPIM developed in Chapter 4 to a two dimensional cable-gear interaction model. The remaining issues include drag and friction due to the contact of cables with the seafloor and moving boundary conditions. Regarding the distributed load from the seafloor, it depends on burial condition, soil, the topology of a seafloor and marine growth on exposed cable section. So far, a simplified friction model, which relies on submerged cable weight and friction coefficient, is adopted in the present study. One representative moving boundary scenario is to be investigated.

5.1 Submarine Cables with Moving Boundary Conditions

Considering a partially buried cable with spans exposed to sea water in the rocky or the active moving sand wave area, the exposed part may get seized and then be towed by a trawl gear. It is assumed that the cable is not tensioned before being captured by a gear. The two ends of a cable segment entangled with a gear are buried in sand waves or hooked by either rocks or other subsea facilities. A simplified seafloor friction model is used for the numerical investigation for the purpose of illustrating the proposed model and algorithm. The cable experiencing friction force resulted from contact with the

seabed is expressed as

$$q_f = W_s \cdot \mu_f \tag{4.1}$$

where, W_f (N/m) is submerged weight and μ_f is an equivalent friction coefficient.

A two dimensional model shown in Fig. 5.3 is established to simulate the behavior of a towed cable under sliding boundary conditions. Since two ends of a cable span are hooked by obstacles, the target cable segment may slide at the hooked points as shown by the green line in Fig. 5.3 when tension exceeds the resistance force at the ends. Before the cable slides around the hooking points, the two ends are simply supported. The trawl load is distributed over the contact area between a trawl board and the cable. In the vicinity of the contact area, bending may control the failure of cable in a small region and the bending moment should be monitored and checked at this bending dominating zone as well as tension. Outside the bending zone, tension determines the possible breakage of the cable. The target cable segment length changes due to the sliding boundaries.

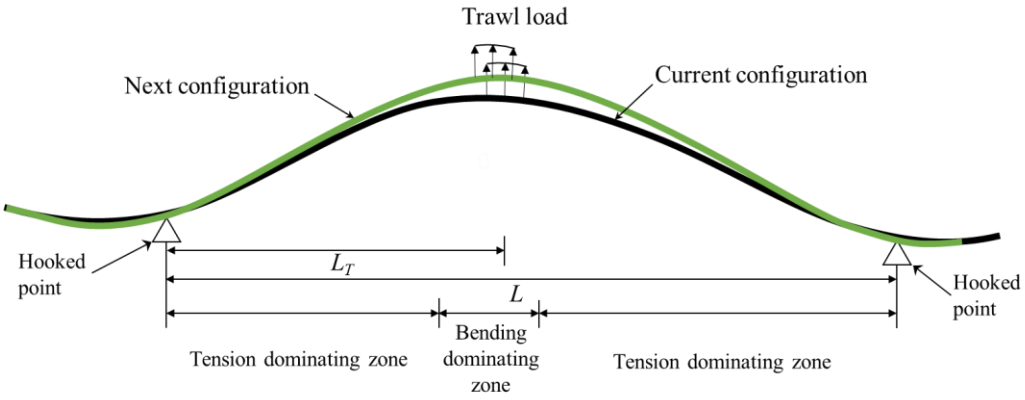

Fig. 5.3 A two dimensional trawl-cable model with moving boundaries

5.2 Analysis Scheme of a Cable with Moving Boundaries

The work flow aims to conduct static analysis of slender rods with the inclusion of incremental load has been elaborated and verified in Section 4.3. To investigate the impact of this length variation, an iterative scheme is proposed to simulate the sliding boundary condition for a preliminary study. A working flow presented in Fig. 5.4 is proposed to be integrated with flowchart shown on page 102 specially addressing moving boundary conditions.

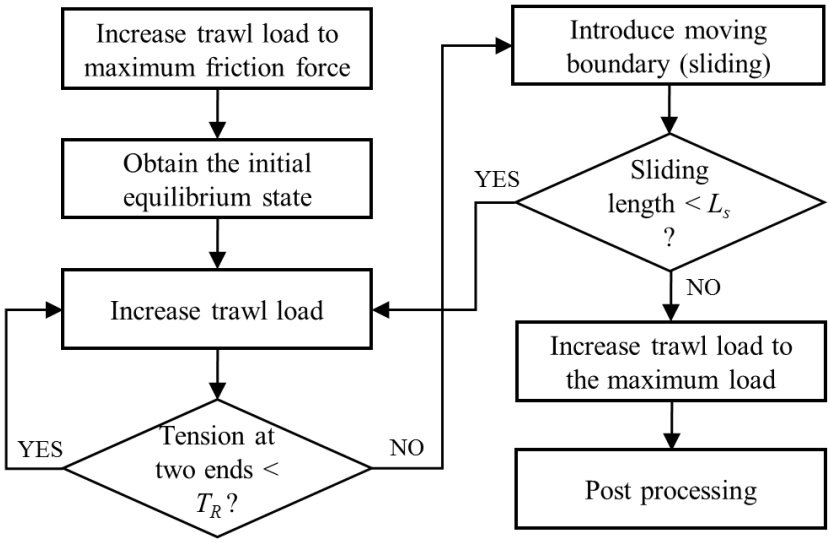

Fig. 5.4 Flow chart of solving this moving boundary condition problem

First, it is necessary to obtain the equilibrium state under which the trawl load overcomes the friction force from the seafloor. Second, the trawl load may keep increasing until the tension at the two ends of this cable segment reaches the maximum resistance force (T_R) at these two hooked points. The maximum resistance forces and

the subsequent allowable sliding lengths may be different at these two ends. When both ends release the maximum sliding lengths (L_s), the trawl load can be gradually applied till the maximum trawl load. Maximum tension and bending moment in the bending dominating zone can be monitored at every analysis step for structural integrity evaluation.

5.3 Response of a Cable Span Sliding at One End

Up to this point, the arbitrary initial layout, large deflection, deflection-dependent trawl load, and moving boundary have been handled in the developed scheme and meshfree method. A cable span with the inclusion of one sliding boundary is adopted to demonstrate the potential of the developed scheme and to simulate the interaction between a trawl board and a submarine cable. The specifications of a cable and dimensions of a cable span are listed in Tab. 5.1. Initial layout of this cable span is illustrated in Fig. 5.5 in which the span is pin-pin supported and subjected to incremental trawl load before span reaches the initial equilibrium state. Some analysis parameters are presented in Tab. 5.2.

Table 5.1 Specification of a cable and data for the cable segment

Axial stiffness (EA, $N\,m^2$)	Bending stiffness (EI, N)	Span length (L, m)	Gear location (L_T,m)	Cable length (L_c, m)
1.4560E8	1.8625E4	100	50	101.56

Note: the armor layer bears all the external loads.

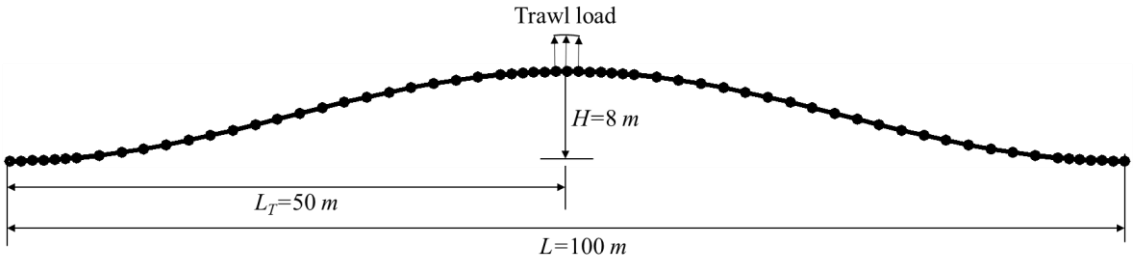

Fig. 5.5 Initial layout of a cable segment and node representation

Table 5.2 Load and parameters for simulation

Unit weight (*N/m*)	Friction coefficient (μ_f)	Max. resistance (T_R, k*N*)	Max. sliding length (L_s, *m*)	Max. trawl load (F_t, k*N*)
235	0.5	35	5	200

Since the static analysis solves a nonlinear equation and fulfilled by an iterative scheme, the trawl load may be increased step by step so as to achieve the initial equilibrium state in case of numerical divergence due to large deflection. The initial equilibrium configuration presented in Fig. 5.6 is reached under the trawl load of 11.75 kN. At the meantime, tension is plotted in Fig. 5.7 in which tension drops at the contact area due to the presence of trawl board. Also Fig. 5.6 reveals bending near the trawling point may be significant than the tension dominant zone as bending depends on curvature.

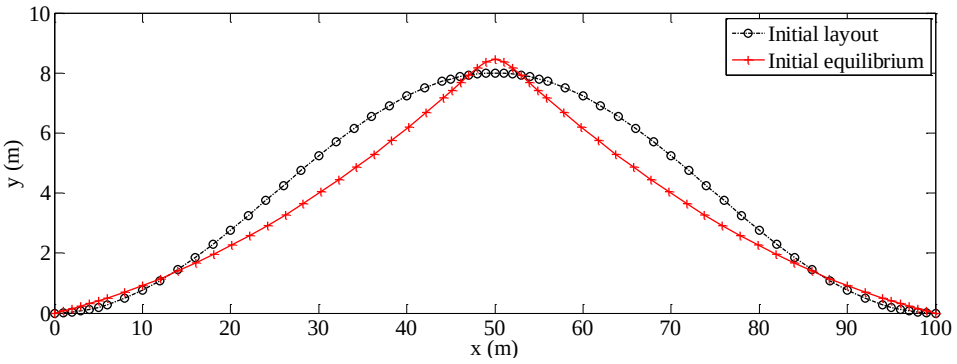

Fig. 5.6 Equilibrium configuration with maximum friction from seafloor

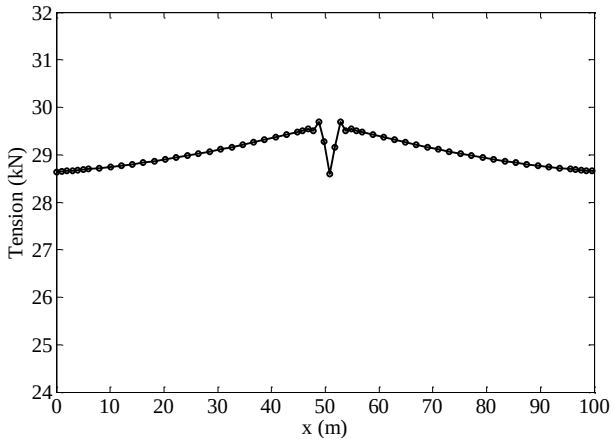

Fig. 5.7 Tension along the cable span at the initial equilibrium state

Then the trawl load is keep increasing to pull the cable until tension at the right end of the span reaches the maximum resistance. The trawl load of 13.55 kN is figured out corresponding to the resistance force 35 kN. The tension at the end increases linearly with the trawl load since the configuration changes slightly as demonstrated in Fig. 5.8. The trawl point moves forward only 0.16 *m*.

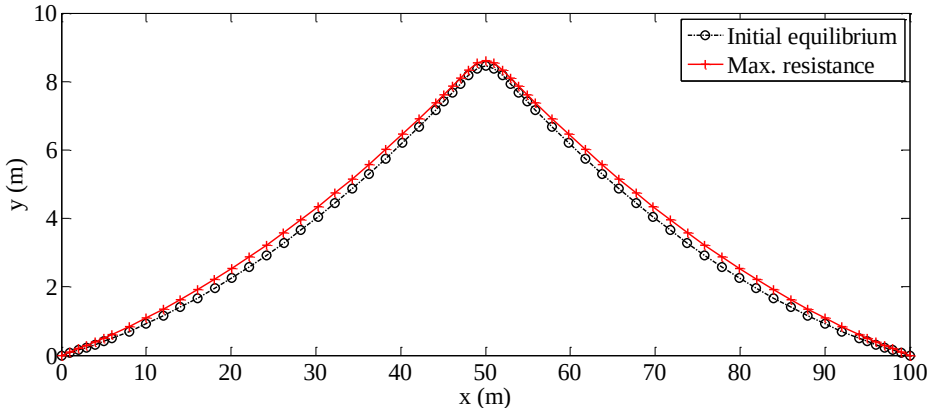

Fig. 5.8 Configuration when tension at right end reaches maximum resistance

The cable is gradually pulled out at the right hooked point as the trawl load increases. Consequently the cable length between the hooked points are increased during this pull-out process. Additional nodes are keeping appended to capture the length change in the static analysis. The resulted configuration of the cable spans are depicted in Fig. 5.9. The trace of the trawling point can be recorded assuming the direction doesn't change in the pull-out process. Then, the trawl load also increases with the sliding length as shown in Fig. 5.10, which shows nonlinear correlation with the sliding length. Fig. 5.11 presents maximum tension, which occurs at different point along the cable span.

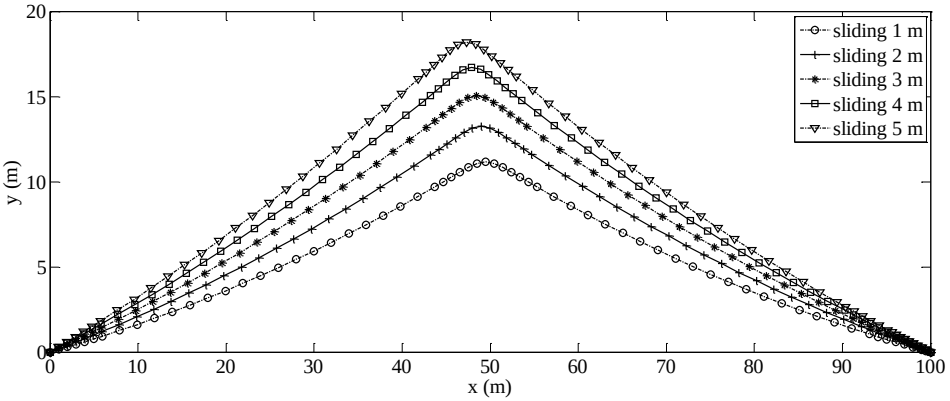

Fig. 5.9 Equilibrium configurations under different sliding lengths

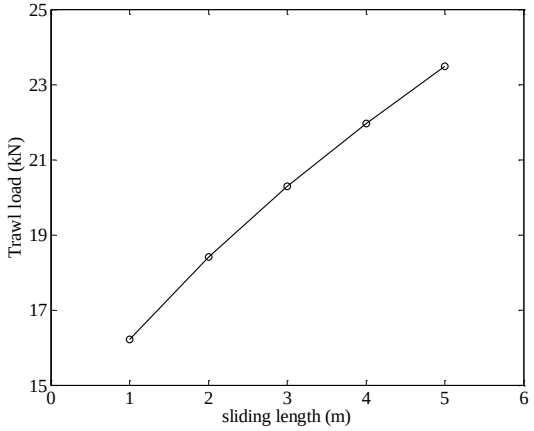

Fig. 5.10 Trawl load versus sliding length

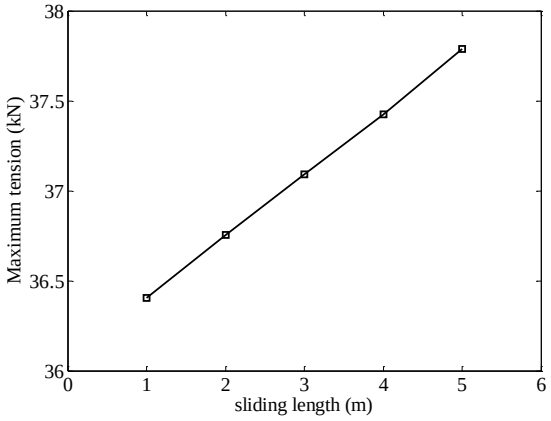

Fig. 5.11 Maximum tension versus sliding length

Eventually, the sliding end releases the maximum allowable sliding cable length, the ultimate strength analysis can be performed using the scheme demonstrated in Fig. 4.10, which can handle incremental external loads. Fig. 5.12 shows the maximum tension along the cable span with respect to trawl load and linear correlation is obtained because the configuration slightly changes during the ultimate loading process. The maximum tension and bending moment are also able to be reported in the ultimate strength loading stage, which can be adopted to predict possible breakage or failure of the cable span.

Different failure modes may be considered for both telecom cable and power cable and for different loading scenarios. In reality a few more moving boundary cases may exist and need scrutiny in respect of a thorough structure evaluation of submarine cables. Taking advantage of the proposed meshfree method and analysis procedures, cable responses may be explored under more scenarios.

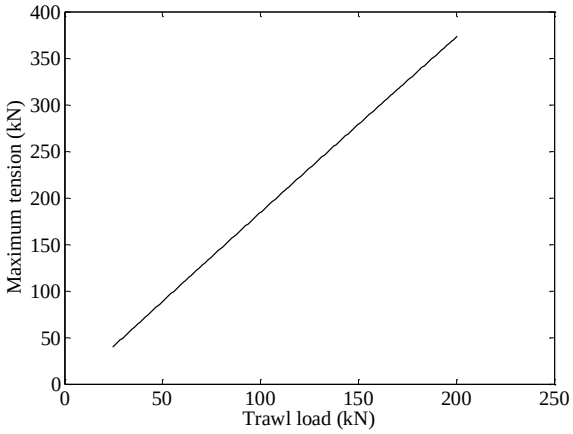

Fig. 5.12 Maximum tension along the cable span

6. SUMMARY

This first part of this research document presents and discusses a computationally efficient 2-D boundary element model that can be used for the initial investigation of the steady state thermal field surrounding a subsea pipeline conveying high temperature wellhead fluids. The model address pipelines buried in layered soils with low hydraulic permeability and is used to facilitate parametric studies of key design parameters. The second part of this research investigation as reported, focused on the formulation and application of a meshfree method. After careful scrutiny of available mathematical modeling approaches, a formulation utilizing slender rod theory and the Local Hermite-type Radial Point Interpolation Method (LRPIM) was developed. Use of the slender rod formulation provided the means to handle the large deflection of slender rods where the flexibility to address regions where bending stiffness, tension and elongation may result when subsea cables are ensnared by commercial fishing gears.

6.1 Summary on the Thermal Field Problem

The steady state heat transfer in a deepwater layered media was further formulated and a generalized numerical procedure was proposed in Section 2, which is able to accommodate complex geometries and plausible boundary conditions. Two comparative examples with finite element solutions were presented to demonstrate the computational efficiency of BEM and the accuracy of the resulting numerical predictions. Next a finite element simulation was performed in order to access the

significance of natural convection on the thermal field in a typical deepwater marine clay. This was performed using Code_Bright for cases assuming impermeable or permeable soil conditions. This comparison provided the rational for neglecting convective fluid flow in clay with extremely low hydraulic permeability, as was assumed for the BEM simulations. Complicated multi-domain configurations, typical of robotic trenching were used to illustrate the utility of the BEM for parametric studies involving curved boundary conditions. The parametric studies presented quantitatively assessed the factors that impact thermal fields surrounding a pipeline buried in a multi-layered environment.

The importance of soil stratification, geometric profiles of trenching and backfill included in the boundary element model were investigated. The evidence suggests that these aspects are important for design and the evaluation of the thermal field and should be included in numerical simulations providing information for the structural and thermal design of buried pipelines. Linear correlation between the uniform heat flux and the mean internal wall temperature using a specific case offers guidance on the preliminary thermal design of buried pipelines such as the insulation material, the coating thickness, and the optimized burial depth. The significance of backfill thermal conductivity on temperature distributions along the external pipe wall was quantitatively evaluated. Additionally, regarding the same external pipe wall temperature, larger diameter pipes require greater output thermal power in order to maintain the pipe wall temperature as smaller pipes and the output thermal power can be quantitatively evaluated based on the proposed model.

6.2 Summary on the Subsea Cable Problem

The formulation using HRPIM presented in this study is the first time it has been used to approximate the position of a curve in the three dimensional space specifically with respect to the arc-length s. This is different from the conventional interpolation of deflection of beam or shell structures, where the small deflection assumption is used to correlate slope and partial derivative of displacement. The positions of some smooth curves including both first and second derivative were shown to be accurately recovered when only a limited number of nodes were involved, for example three nodes for HRPIM and four nodes for RPIM. However, the accuracy of the second derivative deteriorates even if an optimal shape parameter q=2.1 was used in the MQ-RBF. It was found the interpolation accuracy is not sensitive to the other parameter C in the range of [0.001, 1]. Subsequently, the HRPIM was applied to construct the shape function for position vector and the PIM was used to interpolate the distributed load and Larangian multiplier λ using three nodes in a local support domain. The local Galerkin weak form was then adopted to discretize the governing equations, as it does not rely on background cells for numerical integration needed in the global weak form. The static problem was numerically implemented in Matlab for further application in a manner consistent with program flow charts presented in the text. Finally, the effectiveness and accuracy of the methodology and computer program were confirmed via two benchmark examples that have analytical solutions. The first involves the simulation of the post buckling analysis of a column and it demonstrates that the slender rod with bending stiffness and incremental point loading can be accurately use the new formulation. The

second example involves the solution of a chain without bending stiffness under self-weight and a point load and demonstrates the accuracy of the LRPIM formulation for slender structures subjected to distributed loads.

One simplified but representative submarine cable span with the inclusion of deflection-dependent load, moving boundary and nonlinearity due to large deflection is scrutinized using the developed HRPIM meshfree method and proposed procedures addressing sliding boundary condition. In fact, this is a problem involving with variable structure since the cable length keeps changing when one end slides, effectively changing the length of the cable. The simulation analysis for this cable span is logically divided into four steps. The structural evaluation of the cable can be performed at each stage and the consequent possible failure may be identified. First, the initial equilibrium configuration is achieved through an iterative loading scheme considering the maximum friction force from the seafloor. Second, the trawl load proceeds to the value under which the tension at the end allowing sliding condition reaches the maximum resistance force. Then the node representation is updated according to the instantaneous configuration of the cable span with the inclusion of length variation due to sliding boundary. The status of the cable span is reported for the moving boundary stage including configuration, tension and trawl load. Finally, load exerted by the entangled fishing trawler equipment is incrementally increased to reach the maximum trawl load depending on the capability of the fishing vessel. This example demonstrates the capability and potential of the methodology developed in the current study to explore a wide range of cable entanglement problems in the future.

REFERENCES

Atalay, M.A., Aydin, E.D., Aydin, M., 2004. Multi-region heat conduction problems by boundary element method. International Journal of Heat and Mass Transfer, 47:1549-1533.

Atluri, S.N., Zhu, T., 1998. A new meshless local Petrov-Galerkin (MLPG) approach in computational mechanics. Computational Mechanics, 22:127-127.

Atluri, S.N, Cho, J.Y., and Kim, H.G., 1999. Analysis of thin beams, using the meshless local Petrov-Galerkin method with generalized moving least squares interpolations. Computational Mechanics, 24:334-347.

Atluri, S.N., 2004. *The meshless method (MLPG) for domain & BIE discretizations*, Tech Science Press, Encino, CA.

Bai, Y., Bai, Q., 2005. *Subsea pipelines and risers*, 2nd ed., Elsevier Science, Oxford.

Barletta, A., Lazzari, S., Zanchini, E., Terenzi, A., 2008. Transient heat transfer from an offshore buried pipeline during start-up working conditions. Heat Transfer Engineering, 29(11):942-949.

Bau H.H., 1982. Heat losses from a fluid flowing in a buried pipe. International Journal of Heat Mass Transfer, 25(11):1621-1629.

Belytschko, T., Lu, Y.Y., Gu, L., 1994. Element-free Galerkin methods. International Journal for Numerical Methods in Engineering, 37:229-256.

Braden, A., Hinnah, D., Manikian, V., Monkelien, K., 1998. First Arctic subsea pipelines moving to reality. In: Proceedings of the Offshore Technology Conference, Houston, USA, pp.425-434.

Brebbia, C.A., Dominguez, J., 1977. Boundary element methods for potential problems. Applied Math Modelling, 1:372-378.

Brebbia, C.A., Dominguez, J., 1992. *Boundary elements: an introductory course*, McGraw-Hill Book Co., London.

Chen, J.K., Beraun, J.E., Jih, C.J., 1999. Completeness of corrective smoothed particle method for linear elastodynamics. Computational Mechanics, 24:273-285.

Chen, J.S., Pan, C.H., Wu., C.T., Liu, W.K., 1996. Reproducing kernel partical methods for large deformation analysis for non-linear structures. Computer Methods in Applied Mechanics and Engineering, 139:195-227.

Chen, X.H., Zhang, J., 2001. Dynamic analysis of mooring lines by using three different methods. In: Proceedings of the 11th International Offshore and Polar Engineering Conference, Stavanger, Norway, pp.635-642.

Chen, X.H., 2002. Studies on dynamics interaction between deep-water floating structures and their mooring/tendon systems. Ph.D. dissertation, Texas A&M University, College Station, USA.

Cheng, A.D., Cheng, D.T., 2005. Heritage and early history of the boundary element method. Engineering Analysis with Boundary Elements, 29:268-302.

Chen, J.S., Pan, C., Wu, C.T., 1997. Large deformation analysis of rudder based on a reproducing kernel particle method. Computational Mechanics, 19:211-227.

Cho, J.Y., Atluri, S.N., 2001. Analysis of shear flexible beams, using the Meshless local Petrov-Galerkin method, based on a locking-free formulation. Engineering Computations, 18(1/2):215-240.

Cui, X.Y., Liu, G.R., Li, G.Y., Zheng, G., 2008. A rotation free formulation for static and free vibration analysis of thin beams using gradient smoothing technique. Computer Modeling in Engineering and Science, 38(3):217-229.

DeGeer, D., Nessim, M., 2008. Arctic pipeline design consideration. In: Proceeding of 27th International Conference on Offshore Mechanics and Arctic Engineering, Estoril, Portugal, pp. 1-8.

Det Norske Veritas, 2010. Interference between trawl gear and pipelines, DNV-RP-F111. Høvik, Norway.

Donning, B.M., Liu, W.K., 1998. Meshless methods for shear-deformable beams and plates. Computational Methods in Applied Mechanics and Engineering, 152:47-71.

Drew, S.C., Hopper, A.G., 2009. Fishing and submarine cables working together, a report by International Cable Protection Committee.

Duarte, C.A., Oden, J.T., 1996. H-p-clouds an h-p meshless method. Numerical Methods for Partial Differential Equations, 12:673-705.

European Wind Energy Association, 2010. Powering Europe: wind energy and the electricity grid, a report by the European Wind Energy Association.

Franke, R., 1982. Scattered data interpolation: test of some methods. Mathematics of Computation, 38(157):181-200.

Franke, C., Schaback, R., 1998. Solving partial differential equations by collocation using radial basis functions. Applied Mathematics and Computation, 93:73-82.

Gao, X.W., 2002. The radial integration method for evaluation of domain integrals with

boundary-only discretization. Engineering Analysis with Boundary Elements, 26:905-916.

Gao, X.W., 2006. A meshless BEM for isotropic heat conduction problems with heat generation and spatially varying conductivity. International Journal for Numerical Methods in Engineering, 66:1411-1431.

Gao, X.W., Guo, L., and Zhang, C., 2007. Three-step multi domain BEM solver for nonhomogeneous material problems. Engineering Analysis of Boundary Element, 31:965-973.

Gao, X.W., Wang, J., 2009. Interface integral BEM for solving multi-medium heat conduction problems. Engineering Analysis with Boundary Elements, 33:539-546.

Garrett, D.L., 1982. Dynamic analysis of slender rods. Journal of Energy Resources Technology, 104:303-306.

Gebhart, B., Mollendorf J.C., 1978. Buoyancy-induced flows in water under conditions in which density may arise. Journal of Fluid Mechanics, 89(4):673-707.

Gela, G., Dai, J.J., 1988. Calculation of thermal fields of underground cables using the Boundary Element Method. Power Delivery, 3(4):1341-1347.

Gelach, C., 2012. Three destructive fishing practices and their effects on marine ecosystems. http://aquaviews.net/ocean-news/3-destructive-fishing-practices-effects-marine-ecosystems/

Gharbawy, S.E., 2006. Uplift capacity of buried offshore pipelines. In: Proceeding of 16th International Offshore and Polar Engineering Conference, San Francisco,

USA, pp. 86-92.

Gu, Y.T., Liu, G.R., 2001. A local point interpolation method (LPIM) for static and dynamic analysis of thin beams. Computer Methods in Applied Mechanics and Engineering, 190:5515-5528.

Greengard, L., Rokhlin, V., 1987. A fast algorithm for particle simulations. Journal of Computational Physics, 73:325-348.

Grealish F, Roddy I., 2002. State-of-the-art on deep water thermal insulation systems. In: Proceedings of the 21st international conference on offshore mechanics and arctic engineering, Oslo, Norway, pp. 23-28.

Han, Z.D., Rahendran, A.M., Atluri, S.N., 2005. Meshless local Petrov-Galerkin (MLPG) approaches for solving nonlinear problems with large deformation and rotations. Computer Modeling in Engineering & Sciences, 10(1):1-12.

Hanna, M.A., Salama, M.M.A., 1993. Thermal analysis of power cables in multi-layered soil part 1: theoretical model. Power Delivery, 8(3):761-771.

Heggdal, O., Pedersen, A., Lervik, J.K., Bjerknes, O.J., 2012. Electric heating of pipeline and large export flowline > 30" and more than 100 km. In: Proceeding of the Offshore Technology Conference, Houston, USA, pp. 1-16.

Heimbuch, J., 2010. Submarine communication cables called upon for climate change research. http://www.treehugger.com/clean-water/submarine-communication-cables-called-upon-for-climate-change-research.html

Hermann, M., Soren, P.K., 1980. Fishing gear loads and effects on submarine pipelines. In: Proceedings of the Offshore Technology Conference, Houston, USA, pp.

383-392.

International Cable Protection Committee, 2010. A lecture: about submarine telecommunications cables.

Johnsen, I.B., 2012. Clump-weight trawl gear interaction with submarine pipelines, Master's thesis, NTNU, Trondheim, Norway.

Kogan I., Paull C.K., Kuhnz L., Burton E.J., Thun S.V., et al., 2003. Environmental impact of the ATOC/Pioneer seamount submarine cable, a report by National Marine Securities.

Kikuta, M., Togoh, H., Tanka, M., 1987. Boundary element analysis of nonlinear transient heat conduction problems. Computer Method in Applied Mechanics and Engineering, 62:321-329.

Lenes, A., Lervik, J.K., Kulbotten, H., Nysveen, A., Børnes, A.H., 2005. Hydrate prevention on long pipelines by direct electrical heating. In: Proceeding of 15th International Offshore and Polar Engineering Conference, Seoul, Korea, pp. 25-30.

Li, H., Mulay, S.S., 2013. *Meshless methods and their numerical properties*, CRC Press, Boca Raton.

Liew, K.H., Ng, T.Y., Wu, Y.C., 2002. Mehsfree method for large deformation analysis-a reproducing kernel particle approach. Engineering Mechanics, 24:543-551.

Liu, W.K., Jun, S., Li, S.F., Adee, J., Belytschko, T., 1995. Reproducing kernel particle methods for structural dynamics. International Journal for Numerical Methods in Engineering, 38:1655-1679.

Liu, G.R., Gu, Y.T., 1999. A point interpolation method. In: Proceeding of 4th Asia-Pacific Conference on Computational Mechanics, Singapore, pp. 1009-1014.

Liu, G.R., Gu, Y.T., 2003. A matrix triangularization algorithm for the polynomial point interpolation method. Computer Methods in Applied Mechanics and Engineering, 192:2269-2295.

Liu, G.R., Gu, Y.T., 2001. A local radial point interpolation method (LRPIM) for free vibration analyses of 2-D solids. Journal of Sound and Vibration, 246(1):29-46.

Liu, G.R., 2008. A generalized gradient smoothing technique and the smoothed bilinear form for Galerkin formulation of a wide class of computational methods. International Journal of Computational Methods, 5(2):199-236.

Liu, G.R., Gu, Y.T., 2005. *An introduction to meshfree methods and their programming*, Springer, New York.

Liu, G.R., 2010. *Meshfree methods: moving beyond the finite element method*, 2nd ed., CRC Press, Boca Raton.

Longva, V., Sævik, S., Levold, E., IIstad, H., 2011. Dynamic simulation of free-spanning pipeline trawl board impact. In: Proceeding of 30th International Conference on Ocean, Offshore and Arctic Engineering, Rotterdam, Netherlands, pp. 561-568.

Love, A.E.H., 1944. *A treatise on the mathematical theory of elasticity*, 4th ed., Dover Publications, New York.

Lu, T., Wang, K.S., 2008. Numerical analysis of the heat transfer associated with freezing/solidifying phase changes for a pipeline filled with crude oil in soil

saturated with water during pipeline shutdown in winter. Journal of Petroleum Science and Engineering, 62:52-58.

Ma, W., Webster, W.C., 1994. An analytical approach to cable dynamics: theory and user manual. SEA GRANT PROJECT R/OE-26.

Martin W.W., Sadhal S.S., 1978. Bounds on transient temperature distribution due to a buried cylindrical heat source. International Journal of Heat and Mass Transfer, 21:783-789.

Mendonca, P.T.R., Barcellos, C.S., Duarte, A., 2000. Investigation on the hp-cloud method by solving Timoshenko beam problems. Computational Mechanics, 286-295.

Mitchell, J.K., Adel-Hadi, O.H., 1979. Temperature distribution around buried cables. Power Apparatus and System, 98(4):1158-1166.

Newson, T.A., Brunning, P., Stewart, G., 2002. Thermal conductivity of consolidating offshore clay backfill. In: Proceeding of the 21st International Conference on Offshore Mechanics and Arctic Engineering, Oslo, Norway, pp. 17-24.

Nordgren, R.P., 1974. On the computation of the motion of elastic rods. Journal of Applied Mechanics, 777-780.

Nowak, A.J., Brebbia, C.A., 1989. The multiple-reciprocity method: A new approach for transforming BEM domain integrals to the boundary. Engineering Analysis with Boundary Elements, 6(3):164-167.

Olivella, S., Gens, A., Carrera, J., Alonso, E.E., 1996. Numerical formulation for a simulator (CODE_BRIGHT) for the coupled analysis of saline media.

Engineering Computation, 13(7):87-112.

Osborne, R. Franzer, I., 2001. Flowline burial: the key to unlocking subeconomic marginal discoveries. In: Proceedings of the Offshore Technology Conference, Houston, USA, pp. 1-8.

Ochiai, Y., Sladek, V., Sladek, J., 2006. Transient heat conduction analysis by triple-reciprocity boundary element method. Engineering Analysis with Boundary Elements, 30:194-204.

París, F., Cañas, J., 1997. *Boundary element method: fundamentals and applications*, Oxford University Press, Oxford.

Raju, I.S., Philips, D.R., Krishnamurthy, T., 2004. A radial basis function approach in the meshless local Petrov-Galerkin method for Euler-Bernoulli beam problems. Computational Mechanics, 34:464-474.

Schaback, R., 1995. Error estimates and condition numbers for radial basis function interpolation. Advances in Computational Mathematics, 3:251-264.

Rokhlin, V., 1985. Rapid solution of integral equations of classical potential theory. Journal of Computational Physics, 73: 25-348.

Simões, N., Tadeu, A., 2005. Fundamental solutions for transient heat transfer by conduction and convection in an unbounded, half-space, slab and layered media in the frequency domain. Engineering Analysis with Boundary Elements, 29:1130-1142.

Sutradhar, A., Paulino, G.H., Gray, L.J., 2002. Transient heat conduction in homogeneous and non-homogeneous materials by the Laplace transform

Galerkin boundary element method. Engineering Analysis with Boundary Elements, 26:119-132.

Su J., 2003. Flow assurance of deepwater oil and gas production: a review. In: Proceedings of the 22nd International Conference on Offshore Mechanics and Arctic Engineering, Cancun, Mexico, pp. 624-643.

Teigen, P., Ilstad, H., Levold, E., Hansen, H. 2009. Hydrodynamical aspects of pipeline over trawling. In: Proceedings of the 19th International Offshore and Polar Engineering Conference, Oska, Japan, pp. 435-442.

Thiyagarajan R., Yovanovich M.M., 1974.Thermal resistance of a buried cylinder with constant heat flux boundary condition. Journal of Heat Transfer, 96(2):249-250.

Timoshenko, S., 1936. *Theory of elastic stability*, 1st ed., McGraw-Hill Inc., New York.

Vervik, S., 2011. Pipeline accidental load analysis. M.S. thesis, NTNU, Trondheim, Norway.

Wang, J.G., Liu, G.R., 2002. A point interpolation meshless method based on radial basis functions. International Journal for Numerical Method in Engineering, 54:1623-1648.

Wang, J.G., Liu, G.R., 2002. On the optimal shape parameters of radial basis functions used for 2-D meshless methods. Computer Methods in Applied Mechanics and Engineering, 191:2611-2630.

Worzyk, T., 2009. *Submarine power cables: design, installation, repair and environmental aspects*, Springer-Verlag, New York.

Wrobel, L.C., Brebbia, C.A., 1979. The boundary element method for steady state and

transient heat conduction. In: Proceedings of the 1st International Conference: Numerical methods in thermal problems, Swansea, Wales, pp. 58-73.

Wu, Z.M., 1992. Hermite-Birkholf interpolation of scattered data by radial basis functions. Approximation Theory and its Applications, 8:1-10.

Department of Geotechnical Engineering and Geo-Sciences of the Technical University of Catalonia (UPC), CODE_BRIGHT: A thermal-hydro-mechanical analysis program in geological media (Version 3), Barcelona, Spain, 2013. Available from https://www.etcg.upc.edu/recerca/webs/code_bright.

Xu, C., Yu, B., Zhang, Z.W., Zhang, J.J., Wei, J.J., Sun, S.Y., 2010. Numerical simulation of a buried hot crude oil pipeline during shutdown. Petroleum Science, 7:73-82.

Yang M.T., Park K.H., Banerjee P.K., 2002. 2D and 3D transient heat conduction analysis by BEM via particular integrals. Computational Method in Applied Mechanics and Engineering, 191:1701-1722.

Young, A.G., Osborne, R.S., Franzer, I., 2001. Utilizing thermal properties of seabed soils as cost-effective insulation for subsea flowlines. In: Proceedings of the Offshore Technology Conference, Houston, USA, pp. 1-6.

Zhang, X., Song, K.Z., Lu, M.W., Liu, X., 2000. Meshless methods based on collocation with radial basis functions. Computational Mechanics, 26:333-343.

Zhang, X., Liu, X.H., Song, K.Z., Lu, M.W., 2001. Least-squares collocation meshless method. International Journal for Numerical Method in Engineering, 51:1089-1100.

Zhu, S.P., Satravaha, P., 1996. An efficient computational method for modelling transient heat conduction with nonlinear source terms. Applied Mathematical Modelling, 20:513-522.

APPENDIX

A1. Validation of LBEM for Three Different Boundary Condition Cases

LBEM is first validated in a homogeneous medium in a single domain with the three basic boundary conditions: Neumann, Dirichlet, and mixed boundary condition. The unit of length is meter and the unit of temperature is Kelvin for all three cases. The boundary conditions and temperature distributions are shown in Fig. A1.1 to Fig. A1.3.

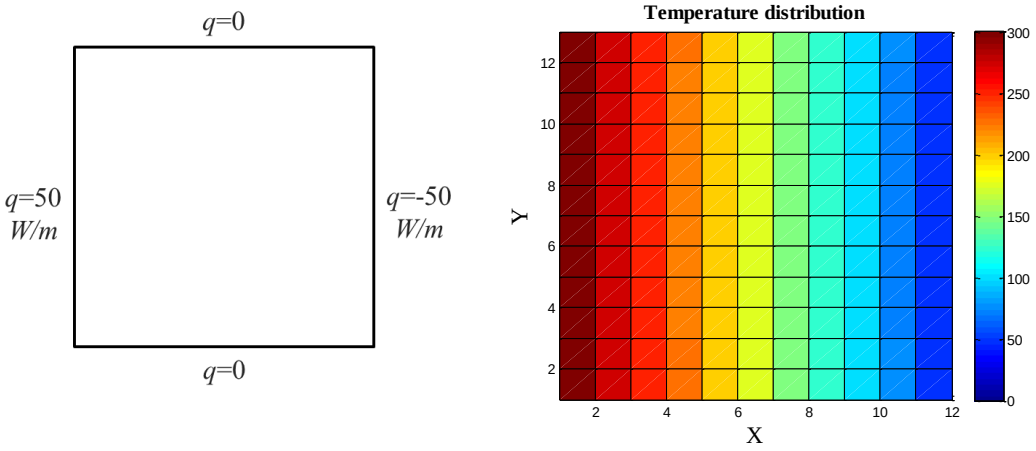

Fig. A1.1 Neumann boundary condition case

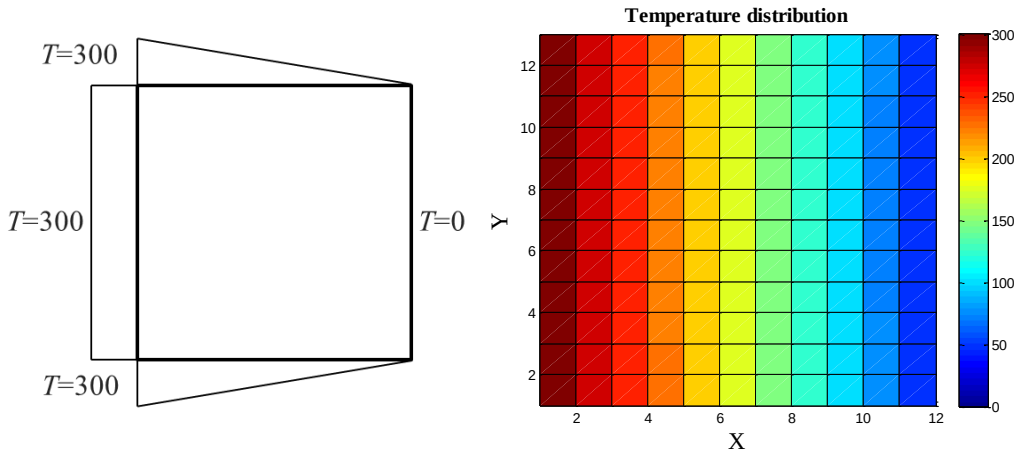

Fig. A1.2 Dirichlet boundary condition case

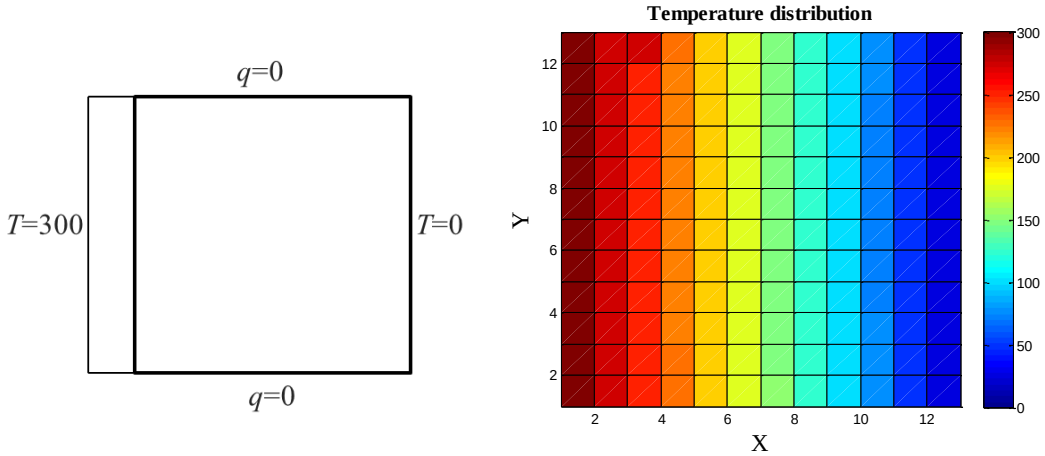

Fig. A1.3 Mixed boundary condition case

A2. Format Input File of LBEM

A format *.txt file is designed to prepare the input information for LBEM, which defines node, element, boundary condition, sub-regions, interface, and material property. An input file example is listed below.

**Square domain with internal heat source

```
*Number of node, element, sub-regions, and interfaces (NES)
330 166 2 1
**Coordinates of boundary nodes (NODE)
*Node     X        Y
1         -4       0
2         -3.9     0
...
329       4        -0.2
330       4        -0.1
**Numbering of element and node of each element (ELEM)
*Element    node1   node2   node3
1           1       2       3
2           3       4       5
...
165         327     328     329
166         329     330     85
*Boundary condition (KODE)
10          0       10      0       10      0
...
1           0       1       0       1       0
**Number of element for each sub-region (NEMS)
*Group
1 102
2 102
**Element of each sub-region (ELMS)
*Region01
1           1
...
1           102
*Region02
1           108
...
0           1
1           107
**Number of interfaces (NI)
*Nint
1 38
**Interface of regions, element of the interface (ELIN)
*Interface01
1
2
...
41
42
**Material for each region (Thermal conductivity) (MAT)
*Material property
1 1
2 10
```